Available online at www.sciencedirect.com
ScienceDirect
Comput. Methods Appl. Mech. Engrg. 410 (2023) 115983
Computer methods in applied mechanics and engineering
www.elsevier.com/locate/cma

A comprehensive and biophysically detailed computational model of the whole human heart electromechanics

Marco Fedele[a,*], Roberto Piersanti[a], Francesco Regazzoni[a], Matteo Salvador[a], Pasquale Claudio Africa[a], Michele Bucelli[a], Alberto Zingaro[a], Luca Dede'[a], Alfio Quarteroni[a,b]

[a] *MOX - Department of Mathematics, Politecnico di Milano, Piazza Leonardo da Vinci, 32, Milano, 20133, Italy*
[b] *Mathematics Institute (Professor Emeritus), École Polytechnique Fédérale de Lausanne, Av. Piccard, Lausanne, CH-1015, Switzerland*

Received 24 July 2022; received in revised form 27 February 2023; accepted 27 February 2023
Available online 21 March 2023

Abstract

While ventricular electromechanics is extensively studied in both physiological and pathological conditions, four-chamber heart models have only been addressed recently; most of these works however neglect atrial contraction. Indeed, as atria are characterized by a complex anatomy and a physiology that is strongly influenced by the ventricular function, developing computational models able to capture the physiological atrial function and atrioventricular interaction is very challenging. In this paper, we propose a biophysically detailed electromechanical model of the whole human heart that considers both atrial and ventricular contraction. Our model includes: (i) an anatomically accurate whole-heart geometry; (ii) a comprehensive myocardial fiber architecture; (iii) a biophysically detailed microscale model for the active force generation; (iv) a 0D closed-loop model of the circulatory system, fully-coupled with the mechanical model of the heart; (v) the fundamental interactions among the different *core models*, such as the mechano-electric feedback or the fibers-stretch and fibers-stretch-rate feedbacks; (vi) specific constitutive laws and model parameters for each cardiac region. Concerning the numerical discretization, we propose an efficient segregated-intergrid-staggered scheme that includes a computationally efficient strategy to handle the non-conductive regions. We also propose extending recent stabilization techniques – regarding the circulation and the fibers-stretch-rate feedback – to the whole heart, demonstrating their cruciality for obtaining a stable formulation in a four-chamber scenario. We are able to reproduce the healthy cardiac function for all the heart chambers, in terms of pressure–volume loops, time evolution of pressures, volumes and fluxes, and three-dimensional cardiac deformation, with volumetric indexes within reference ranges for cardiovascular magnetic resonance. We also show the importance of considering atrial contraction, fibers-stretch-rate feedback and the proposed stabilization techniques, by comparing the results obtained with and without these features in the model. In particular, we show that the fibers-stretch-rate feedback, often neglected due to the numerical challenges that it entails, plays a fundamental role in the regulation of the blood flux ejected by ventricles. The proposed model represents the state-of-the-art electromechanical model of the iHEART ERC project – an Integrated Heart Model for the Simulation of the Cardiac Function – and is a fundamental step toward the building of physics-based digital twins of the human heart.

Keywords: Multiphysics and multiscale modeling; Whole-heart modeling; Cardiac electromechanics; Computational cardiology; High performance computing; Cardiac digital twin

* Corresponding author.
E-mail address: marco.fedele@polimi.it (M. Fedele).

https://doi.org/10.1016/j.cma.2023.115983

1. Introduction

Computational models of the cardiac function are progressively increasing their role in cardiology, revealing diagnostic information, contributing to the development of new therapies and promising patient-specific treatments based on individual pathophysiology [1–3]. Successful examples can be found in the context of cardiac electrophysiology [4–9], electromechanics [10–14] and fluid-dynamics [15–17], often in a multiphysics coupled framework involving fluid–structure or electro-mechano-fluid interaction [18–25].

The growing demand for computational models in clinical applications requires the development of increasingly detailed mathematical models and efficient numerical methods [26–36]. In the context of cardiac electromechanics, a biophysically detailed model of the human heart encompasses all the multiscale and multiphysics processes underlying the cardiac function, ranging from the cellular (microscale) to the organ (macroscale) level, such as the propagation of the electrical signal, the active and passive mechanics, and the interaction with the circulatory system [27]. Moreover, the biophysics of the heart tissue is substantially different among atria, ventricles and non-conductive regions (e.g. valves, arteries). Further modeling difficulties are given by the complex anatomy made up of many components with non-trivial shapes, each of which plays an important role in the cardiac function [37,38].

All these complex aspects make accurate simulation of the cardiac cycle – characterized by highly coordinated electrical, mechanical and valvular events – a very challenging subject still not fully addressed. In particular, the literature lacks electromechanical models of the entire human heart that take into account both atrial and ventricular contraction in detailed whole-heart geometries. While ventricular electromechanics in image-based geometries is extensively studied in both physiological and pathological conditions [4,12,27,31,32,39–44], whole-heart models emerged only in recent years [9,21,26,30,36,45–53]. Some studies focus only on electrophysiology [9,36,51,53] or, if they consider electromechanics, include the atrial muscle only as passive tissue [21,26,45,46,49,50]. More specifically, Sugiura et al. [45] review the essential methodologies for a multiscale and multiphysics heart model using the University of Tokyo whole-heart simulator. However, the electromechanical results are limited to the ventricles, as well as those of related papers using this simulator [54,55]. Fritz et al. [46] propose a whole-heart image-based model of the ventricular contraction that considers the interaction with passive atria, pericardium and surrounding organs, demonstrating their impact on the modeling of a physiological heart deformation. Augustin et al. [26] focus their study on the importance of considering anatomically accurate image-based geometries of the entire heart. They also develop novel numerical techniques that allow solving these complex problems in high-resolution computational meshes. Santiago et al. [21] present a fluid-electro-mechanical model of the heart focusing on the ventricles and the arterial flow. They perform simulations in the anatomically accurate Zygote Solid 3D Heart Model [56], considering simplified passive atria filled with a soft material in their cavity. Despite this simplification, they show the impact of including atria to achieve physiological ventricular motion. Pfaller et al. [49] analyze the importance of proper epicardial boundary conditions in the mechanical model to correctly surrogate the effect of the pericardium and surrounding organs. Strocchi et al. [50] propose similar boundary conditions but considering spatially varying coefficients, to take into account the different stiffness of the surrounding organs. Both of these studies are based on whole-heart geometries reconstructed from medical images, that are also used to validate the results. Finally, Strocchi et al. [30] release a publicly available cohort of four-chamber heart meshes reconstructed from CT-images to facilitate the study of the whole-heart electromechanics. They also perform simulations of the ventricular electrical activation and contraction on this cohort. Furthermore, some works as [21,23] have developed fully coupled electro-mechano-fluid models of the heart, in which electromechanics is bidirectionally coupled to three-dimensional models of hemodynamics. The extension to four chamber models in this setting is however still in its infancy [19,24].

All the aforementioned electromechanical models neglect atrial contraction, that, to the best of our knowledge, is instead considered only in a few works, namely [47,48,52]. Baillargeon et al. [47] present the Living Heart project, a simulator of the human cardiac function that includes a phenomenological representation of both ventricular and atrial active contraction. This simulator has been extensively used in recent years, but mainly to study ventricular pathologies [13,14,57,58], while more details on atrial contraction (such as pressure–volume loops) have never been shown. The work of Land and Niederer [48] is the first one focusing on the influence of atrial contraction on the cardiac function, investigating also an atrial fibrillation scenario. Active contraction is taken into account using the lumped-parameter model previously proposed for the ventricles [59], by adapting some parameters to the atrial case. This work shows, as a result, atrial pressure–volume loops that qualitatively tend to the distinguishing

physiological eight-shape. Gerach et al. [52] use the same active contraction model while also including a three-dimensional representation of the pericardium, the adipose tissue and the beginning of the major vessels. They show atrial pressure–volume loops that qualitatively match the characteristic eight-shape, representing the most realistic result concerning atrial function available in the literature. However, blood fluxes across the semilunar valves thereby shown substantially exceed the physiological values. As we show in our paper, these anomalies can be explained by the lack of the fibers-stretch-rate feedback (between passive mechanics and active force generation model). Indeed, this feedback is commonly neglected since it can generate, at a numerical level, strong non-physical oscillations [52,60]. In this work, we successfully cure these numerical instabilities with negligible computational cost by introducing stabilization terms that extend the approach previously proposed in abstract terms by Regazzoni [61] to the whole heart. This allows us, for the first time in the literature (to the best of our knowledge), to assess the role of the fibers-stretch-rate feedback in four-chamber electromechanics.

Compared to the ventricles, the atria exhibit a more complex anatomy and physiology, characterized by a thinner and weaker muscle strongly influenced by ventricular contraction and relaxation. Consequently, computational models of the atrial function are very challenging and must consider properly calibrated biophysically detailed models of the four chambers in order to obtain physiologically meaningful results. In this paper, we propose a novel mathematical model of whole-heart electromechanics endowed with biophysically detailed *core models* for electrophysiology, passive mechanics, and ventricular and atrial active contraction. Specifically, our mathematical model – that extends the left-ventricular model we have recently proposed in [31] – features several innovative contributions:

- an anatomically accurate whole-heart model consisting of detailed geometries for the four chambers, simplified valves acting as electrically insulating regions, and the initial tracts of the arteries;
- an accurate myocardial fiber architecture using a novel whole-heart Rule-Based-Method (RBM) that extends previously proposed models [51,62] taking into account some additional characteristic atrial fiber bundles;
- chamber-specific and accurate ionic models for atria and ventricles [63,64];
- a biophysically detailed microscale model for the active force generation [65] used for the first time in a whole heart and for the atrial electromechanics;
- a 0D closed-loop model of the circulatory system [31], fully-coupled with the mechanical model in all the heart chambers;
- specific spring–damper Robin boundary conditions to model the pericardium and the surrounding organs [49];
- strong coupling among the different core models, taking into account the most important feedbacks, such as the Mechano-Electric Feedback (MEF) or the fibers-stretch and fibers-stretch-rate feedbacks.

The core models are specifically calibrated for each cardiac compartment. Concerning the numerical discretization, we extend to the whole heart the efficient segregated-intergrid-staggered scheme proposed in [31,32] for the ventricular case. In particular, we introduce suitable stabilization terms by extending recently developed stabilization techniques – related to the circulation [61] and the fibers-stretch-rate feedback [60] – to the whole heart, demonstrating that they are crucial for obtaining a stable formulation in a four-chamber scenario.

The numerical models proposed in this work are characterized by high dimensionality and huge computational complexity, thus calling for efficient and accurate computational tools. To this aim, the solver that we developed for the numerical simulation of the whole-heart electromechanics – which includes also a computationally efficient treatment of the non-conductive regions in the electrophysiology model – has been built upon `life`$^{\mathtt{x}}$,[1] an in-house Finite Element (FE) library focused on large-scale cardiac applications in a High Performance Computing (HPC) framework [66,67].

This paper is structured as follows: in Section 2 we shortly review the anatomy and physiology of the heart; in Section 3 we describe the full electromechanical model; Section 4 is devoted to the numerical discretization; in Section 5 we discuss the numerical results; finally, in Section 6 we draw our conclusions.

2. Cardiac anatomy and physiology

In this section we briefly review the anatomy of the human heart aiming at introducing all the cardiac components that – with different level of details – we consider in our electromechanical model. We also describe the phases of

[1] https://lifex.gitlab.io/

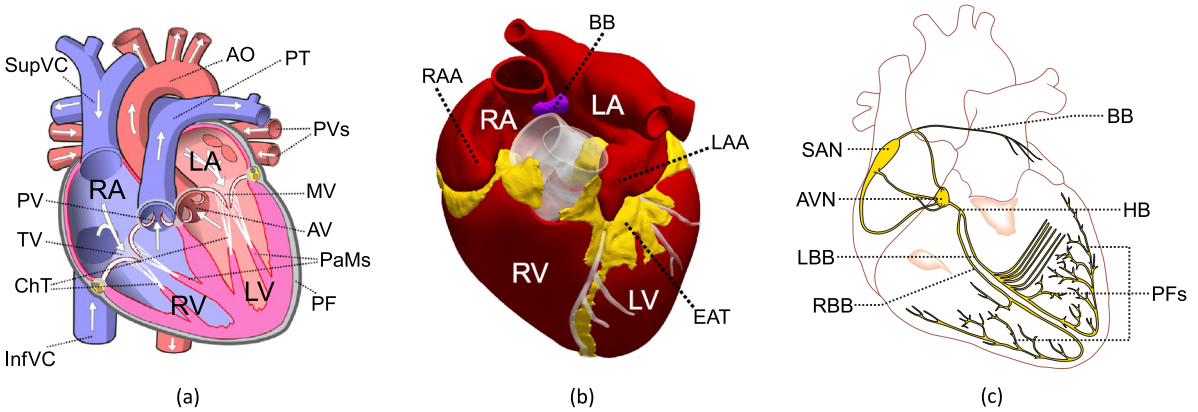

Fig. 1. The anatomy of the heart: (a) a sketch of the internal view of the four chambers and their components (picture elaborated from https://commons.wikimedia.org/w/index.php?curid=830253); (b) an external view of the cardiac anatomy; (c) a sketch of the electrical conduction system (picture elaborated from https://commons.wikimedia.org/w/index.php?curid=10197958). All the abbreviations are defined in Table 1.

Table 1
List of abbreviations.

Cardiac anatomy	
AO	Aorta
AV	Aortic Valve
AVN	AtrioVentricular Node
BB	Bachmann's Bundle
ChT	Chordae Tendineae
CrT	Crista Terminalis
EAT	Epicardial Adipose Tissue
HB	His Bundle
InfVC	Inferior Vena Cava
LA	Left Atrium
LAA	Left Atrial Appendage
LBB	Left Bundle Branch
LV	Left Ventricle
MV	Mitral Valve
PF	Pericardial Fluid
PFs	Purkinje Fibers
PT	Pulmonary Trunk
PV	Pulmonary Valve
PVs	Pulmonary Veins
PaMs	Papillary Muscles
PeMs	Pectinate Muscles
RA	Right Atrium
RAA	Right Atrial Appendage
RBB	Right Bundle Branch
RV	Right Ventricle
SAN	SinoAtrial Node
SupVC	Superior Vena Cava
TV	Tricuspid Valve

Cardiac cycle	
AC	Atrial Contraction
EDV	End Diastolic Volume
ESV	End Systolic Volume
IVC	IsoVolumetric Contraction
IVR	IsoVolumetric Relaxation
SV	Stroke Volume
VE	Ventricular Ejection
VPF	Ventricular Passive Filling
Modeling	
BDF	Backward Differentiation Formula
BDF1	BDF of order 1
BDF2	BDF of order 2
CRN	Courtemanche et al. [63]
DOFs	Degrees Of Freedom
FE	Finite Element
HPC	High Performance Computing
ICI	Ionic Current Interpolation
IMEX	Implicit–Explicit
LDRBM	Laplace–Dirichlet RBM
MEF	Mechano-Electric Feedback
RBM	Rule-Based-Method
RDQ20	Regazzoni et al. [73]
TTP06	ten Tusscher and Panfilov [64]

the cardiac cycle, focusing on the differences of the atrial and ventricular function. For a more in-depth overview of the cardiac anatomy and physiology, we refer to [22,38,68–72].

As shown in Fig. 1, (a)–(b), the human heart is characterized by a very complex anatomy and is made up of several components, each of which plays a crucial role in the cardiac function. The heart is made up of four muscle chambers: RA and Left Atrium (LA) on the upper part, Right Ventricle (RV) and Left Ventricle (LV) on the lower part. Commonly, RA and RV are collectively referred to as *right heart* and their left counterparts (LA and LV) as

left heart. The right heart pumps the oxygen-depleted blood – coming from the systemic venous return and flowing through the Superior Vena Cava (SupVC) and the Inferior Vena Cava (InfVC) – toward the Pulmonary Trunk (PT) into the lungs, where oxygenation takes place; the left heart pumps oxygenated blood – coming from the lungs through the Pulmonary Veins (PVs) – toward the Aorta (AO) into the systemic circulation, closing the loop of the circulatory system.

The blood flow is regulated by four cardiac valves made of strong fibrous tissue: the TV and MV lie in the atrioventricular plane and divide the RA and LA from the RV and LV, respectively, also acting as electrical insulators between atria and ventricles; the Pulmonary Valve (PV) and Aortic Valve (AV) connect the RV and LV to the PT and AO, respectively. Valves passively open and close depending on the pressure exerted on their leaflets; TV and MV are also supported by Chordae Tendineae (ChT) and Papillary Muscles (PaMs) to avoid valve prolapse while closed.

The tissue of the cardiac chambers is made up of three layers: the *endocardium* is the thin innermost layer in direct contact with the blood; the *myocardium* is the thick muscle layer made of *cardiomyocytes*, the cells responsible for generating contractile force in the heart; the *epicardium* forms the thin outermost layer. This latter layer, mainly characterized by a smooth surface, features a complex rough anatomy in some regions (see Fig. 1, (b)). In particular, the atrioventricular regions, the initial part of the arteries (PT and AO) and the presence of the Left Atrial Appendage (LAA) and the Right Atrial Appendage (RAA) contribute to create some empty regions among the different cardiac components. These regions are filled of the Epicardial Adipose Tissue (EAT), a visceral fat deposit that creates a sort of soft pillow among the nearby cardiac components and contributes to make the external surface of the heart a smooth surface.

The whole heart – including EAT – is surrounded by the *pericardium*, a sac that holds the heart in place. This sac is filled with the Pericardial Fluid (PF) which allows the free sliding of the heart external surface, thus also allowing the volume of the four chambers to increase or decrease during the different phases of the cardiac cycle.

The cardiac cycle is a highly coordinated, temporally related series of electrical, mechanical, and valvular events [74]. The contraction of the four cardiac chambers is regulated by the electrical conduction system of the heart whose main components are sketched in Fig. 1, (c). The pacemaking electrical signal arises in the SinoAtrial Node (SAN), located in the RA near the junction of the SupVC. From SAN the signal propagates into the RA myocardium and reaches the LA through specific interatrial bundle connections, of which the most important is the Bachmann's Bundle (BB). On the other side, the conduction network continues toward the AtrioVentricular Node (AVN) where the signal is delayed until the end of the atrial contraction. Then, the signal travels through the His Bundle (HB) and, in the interventricular septum, splits between the Left Bundle Branch (LBB) and the Right Bundle Branch (RBB) to end in the respective Purkinje Fibers (PFs) network located in the subendocardial layer. Through the connection of the PFs with the cardiomyocytes the signal transmurally propagates from the endocardium to the epicardium stimulating the ventricular contraction.

The main mechanical events of the cardiac cycle are sketched in Fig. 2, top, where the heart chambers are darker in color when contracting – i.e. during *systole* – and lighter when relaxing — i.e. during *diastole*. Atrial and ventricular systole and diastole occur in different phases of the cycle. During the IsoVolumetric Relaxation (IVR) phase, the ventricular muscle is relaxing after the end of the ejection phase of the previous heartbeat. Since all the valves are closed, the ventricular volume remains constant while its pressure quickly drops down until it reaches the atrial pressure, causing the opening of the atrioventricular valves (TV and MV). At this moment the Ventricular Passive Filling (VPF) phase begins, blood flows from the atria to the ventricles and the volumes of both ventricles increase, driven by the muscle relaxation that thins the myocardium and moves the ventricular base upwards. At the same time, the atrial volumes decrease due to the passive deformation of the atrial myocardium squeezed by the movement of the atrioventricular plane. We remark that none of the four chambers is contracting during these first two phases. When the passive filling slows down, the Atrial Contraction (AC) begins, stimulated by the pacemaking of the SAN. The active deformation of the atrial muscle pushes additional blood toward the ventricles giving an additional ventricular preload; for this peculiarity, this phase is also called *atrial kick*. The AVN delays the electrical signal, allowing the ventricular contraction to begin only when the atrial contraction has ended. When the ventricular muscle begins to contract, the ventricular pressure suddenly rises, exceeding the atrial pressure and determining the closure of the TV and MV. This event starts the IsoVolumetric Contraction (IVC) phase, in which all the cardiac valves are closed again. This short phase ends when the pressures of the ventricles (RV and LV) reach the pressures of the respective arteries (PT and AO), triggering the opening of the semilunar valves (PV and AV) and the beginning

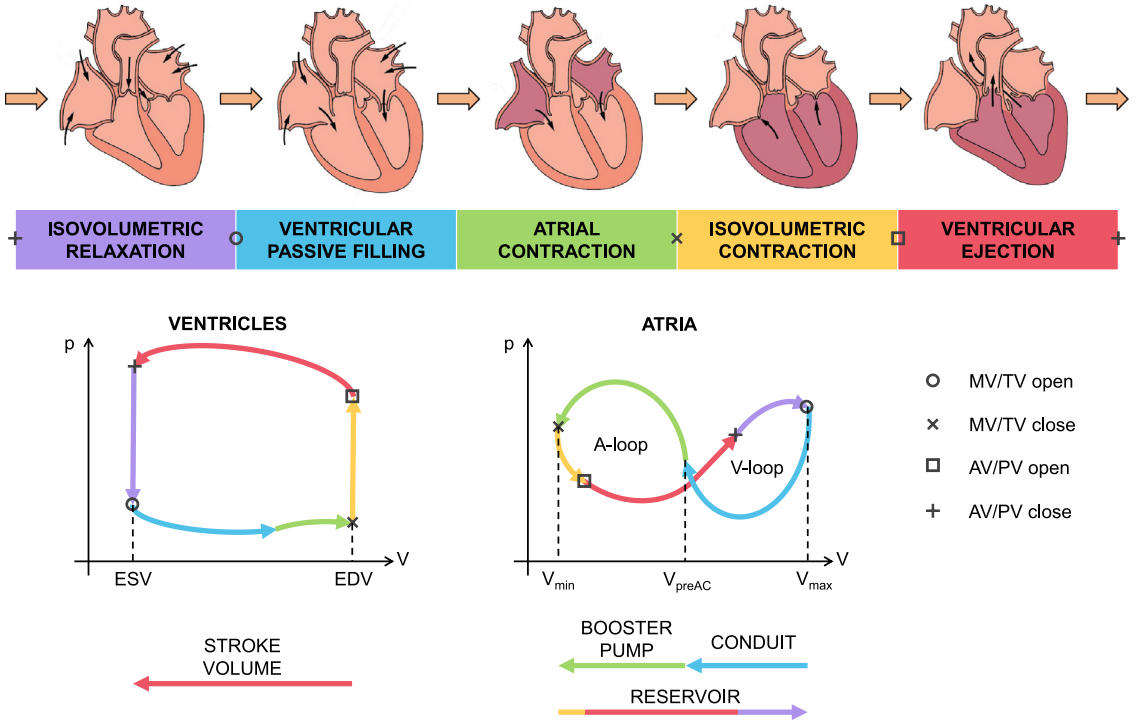

Fig. 2. The five phases of the cardiac cycle: on the top, a sketch of the direction of the blood flow, the status of the valves and the contraction of the chambers (darker color) during the different phases (pictures elaborated from https://commons.wikimedia.org/w/index.php?curid=30148227); on the bottom, schematic ventricular and atrial pressure–volume loops with the opening and closing of the valves and colored with the five phases.

of the Ventricular Ejection (VE) phase. During this last phase, the ventricular volumes drop down – driven by the myocardial thickening and the downward movement of the base – and the blood flows toward the pulmonary and systemic circulation. At the same time the atria fill, passively dilating due to the downward movement of the atrioventricular plane.

A plot of the pressure against the volume has long been used to measure the work done by a system and is also widely applied to assess the efficiency of the cardiac pump. In Fig. 2, bottom, the different phases of the cardiac cycle are shown in this kind of diagram – usually called *pressure–volume loop* – for both ventricles and atria. The squared shape of the ventricular diagram is a direct consequence of the state of the valves and of the two isovolumetric phases. To this counterclockwise loop is associated the (positive) ejection work exerted by the tissue on the blood [22], that increases if the maximum difference in pressures (or in volumes) arises. The difference among the ventricular End Diastolic Volume (EDV) and End Systolic Volume (ESV) is called Stroke Volume (SV) and represents the volume of blood pumped out from each ventricle during a heartbeat. Instead, the interpretation of the eight-shaped atrial loop needs more explanations and can be divided into two parts. The *V-loop* is dominated by the effect of the ventricles on the atria. Indeed, for a substantial part of the cardiac cycle, the atria fill or empty only passively, dragged by the contraction or relaxation of the ventricles. Thus, the clockwise V-loop represents the (negative) work exerted by the ventricles on the atria, since the atria are not contracting during this period (i.e. their muscle is not consuming energy). Conversely, the counterclockwise *A-loop* is dominated by the atrial contraction and relaxation and is associated with the (positive) work exerted by the atrial muscle on the blood. This complex pressure–volume loop is related to the threefold atrial function of *reservoir*, *conduit*, and *booster pump* [75–81] (see Fig. 2, bottom-right): while the atrioventricular valves (TV and MV) are closed, the atria store blood for later delivery to the ventricles (reservoir) when the valves open, atria release blood to the ventricles, passively driven by the ventricular relaxation (conduit) [82]; finally, at the end of ventricular diastole, the atrial muscle contraction actively supplies additional blood to the ventricles (booster pump), increasing the efficiency of the heart pump as is also evident from the effect on the ventricular pressure–volume loop.

This partial introduction to the heart anatomy and to the cardiac cycle aims at highlighting the complexity of concurring events that contribute to a physiological heart function and regulation. In order to capture these events in a computational framework, an electromechanical model must accurately grasp the interaction among the heart chambers, the complex biophysics and all the multiscale and multiphysics aspects underlying the cardiac function.

3. Mathematical models

We propose a mathematical model that extends to the whole heart the cardiac electromechanical model fully coupled with a lumped-parameter model of blood circulation proposed by Regazzoni et al. [31]. Indeed, in that work, the only heart chamber considered as a 3D domain was the LV. This work was then extended by Piersanti et al. [32] to a 3D domain for both ventricles. However, in both cases, the 3D computational domain consists only of the ventricular muscle, which can be considered as a unique tissue with homogeneous electrical and mechanical properties. Here, we extend these ventricular models taking into account the heterogeneity of the cardiac tissue in the different cardiac components (*e.g.* atria, ventricles, valves and vessels) for what concerns both electrical signal conduction and active/passive mechanics. In particular, we carefully distinguish between conductive and non-conductive regions. Moreover, we also introduce some improvements in the core models and their interactions, such as the use of the Regazzoni et al. [73] (RDQ20) model for the active force generation and the inclusion of the fibers-stretch-rate feedback between passive mechanics and active force generation.

In the following sections we detail our mathematical model, focusing on the novelties introduced with respect to [31,32]. In Section 3.1 we define the whole-heart computational domain and we describe the choices made in terms of domain partitioning and boundaries; in Section 3.2 we discuss the modeling of the cardiac fibers; in Section 3.3 we present the full mathematical model by highlighting each core model; in Section 3.4 we describe the strategy employed to recover the unloaded (i.e. stress-free) configuration and to subsequently compute the initial displacement.

3.1. Computational domain

In Fig. 3, (a), we show the computational domain $\Omega_0 \subset \mathbb{R}^3$ of the entire human heart, subdivided in the following subdomains:

- the myocardium of the four cardiac chambers – named Ω_0^{myo} – in turn divided into: (i) the RA and LA – named Ω_0^{RA} and Ω_0^{LA}, respectively – characterized by a detailed anatomy that includes the two appendages (RAA, LAA) and physically connected to each other through the interatrial septum and the BB; (ii) a unique subdomain for the two ventricles – named Ω_0^{V} – with a smoothed endocardium layer deprived of PaMs;
- the two arteries (PT, AO) – named Ω_0^{PT} and Ω_0^{AO}, respectively – modeled up to their main bifurcations so that they can be fixed sufficiently far from their connection with the heart, where their movement can be considered negligible;
- the cardiac valves (TV, MV, PV, AV) – named Ω_0^{valve} – as flat simplified geometries filling the valvular orifices and connecting the atria to the ventricles (TV, MV) and the ventricles to the arteries (PV, AV). Although very simplified anatomically, this representation allows to model some crucial aspects of valvular functioning such as the role of their *annuli* as stiff and insulating fibrous tissue that connects different cardiac compartments and the high pressure difference across their closed leaflets occurring during some phases of the cardiac cycle;
- some artificial caps – named Ω_0^{caps} – placed in all the entry veins (InfVC, SupVC, PVs) and included in the domain in order to close the atrial blood pools, facilitating the calculation of their volumes (see Section 3.3.4).

In order to apply proper boundary conditions to the mechanical model, the boundaries of the domain are divided as follows:

- some artificial boundaries (see Fig. 3, (b)) – named Γ_0^{rings} – placed where the veins (InfVC, SupVC, PVs) and the arteries (PT, AO) are cut;
- the external cardiac surface Γ^{epi} (see Fig. 3, (c)) in turn divided into: (i) the regions of the epicardium in contact with the PF, named $\Gamma_0^{\text{epi,PF}}$; (ii) the regions of the epicardium in contact with the EAT, named $\Gamma_0^{\text{epi,EAT}}$; (iii) the epithelium of the two arteries, named $\Gamma_0^{\text{epi,AR}}$;
- the internal cardiac surface (see Fig. 3, (d)) made up of the endocardium of the four cardiac chambers (RA, LA, RV, LV) – named $\Gamma_0^{\text{endo,RA}}$, $\Gamma_0^{\text{endo,LA}}$, $\Gamma_0^{\text{endo,RV}}$ and $\Gamma_0^{\text{endo,LV}}$, respectively – and the endothelium of the two arteries (PT, AO) — named $\Gamma_0^{\text{endo,PT}}$ and $\Gamma_0^{\text{endo,AO}}$, respectively.

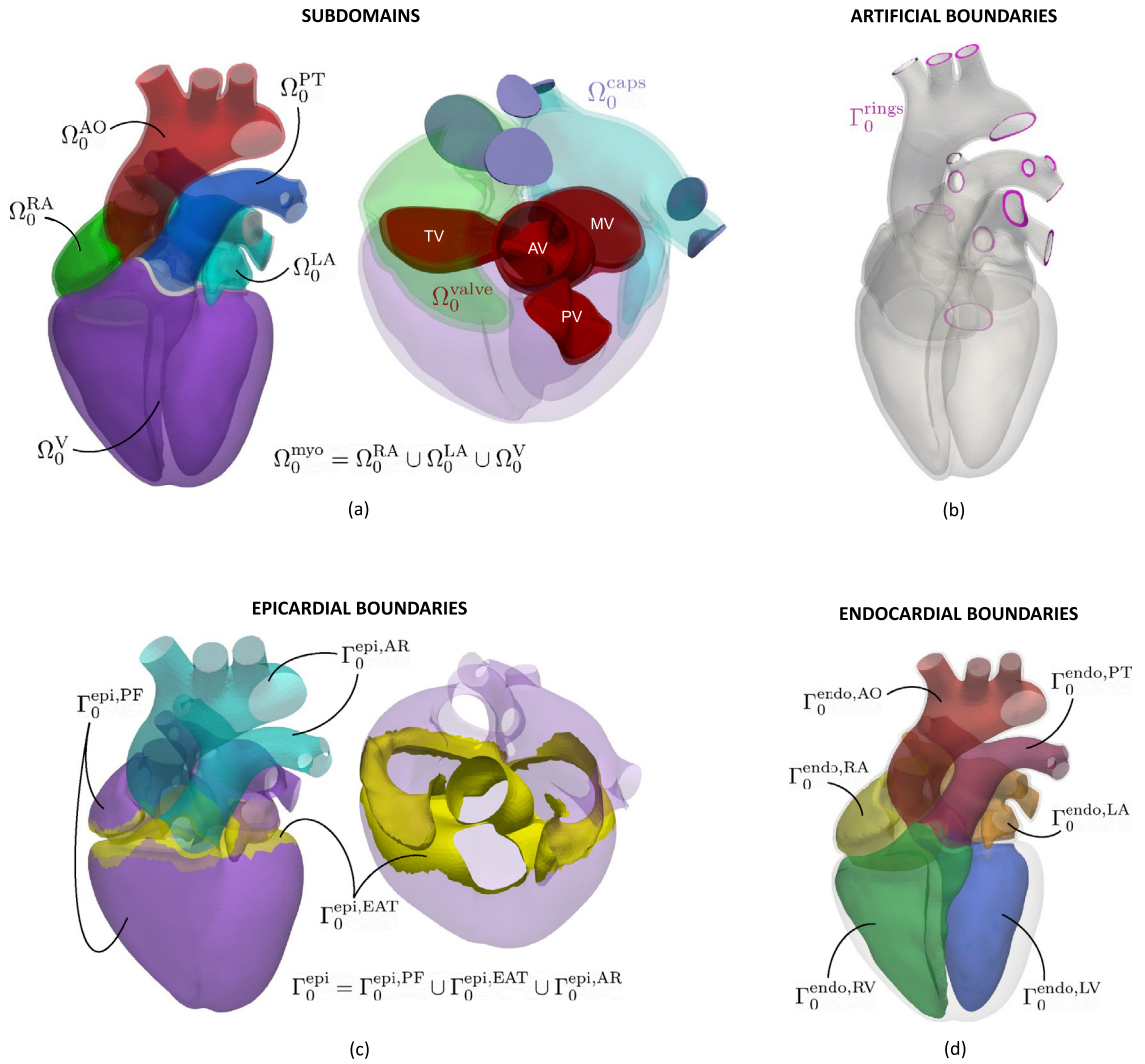

Fig. 3. The computational domain Ω_0: (a) the division in subdomains; (b) the artificial boundaries; (c) the epicardial boundaries; (d) the endocardial boundaries.

3.2. Modeling the cardiac fibers

To prescribe the muscular fiber architecture in the myocardium Ω_0^{myo}, we rely on a particular class of Rule-Based-Methods (RBMs), known as Laplace–Dirichlet RBMs (LDRBMs) [27,84,85]. These methods were recently extended to the whole heart accounting also for atrial geometries by Piersanti et al. [51]. In our work, we further extend the whole-heart LDRBM proposed in [51] taking into account some additional crucial myofiber bundles to better represent the atrial architecture [83].

To properly reproduce the characteristic features of the cardiac fiber bundles in all the four chambers, the whole-heart LDRBM first defines a transmural distance ϕ (from epicardium to endocardium) and several internal distances ψ_i These are obtained by solving Laplace boundary-value problems of the type

$$\begin{cases} -\Delta\xi = 0 & \text{in } \Omega_0^{myo}, \\ \xi = \xi_a & \text{on } \Gamma_0^{a}, \\ \xi = \xi_b & \text{on } \Gamma_0^{b}, \\ \nabla\xi \cdot \mathbf{N} = 0 & \text{on } \Gamma_0^{n}, \end{cases} \tag{1}$$

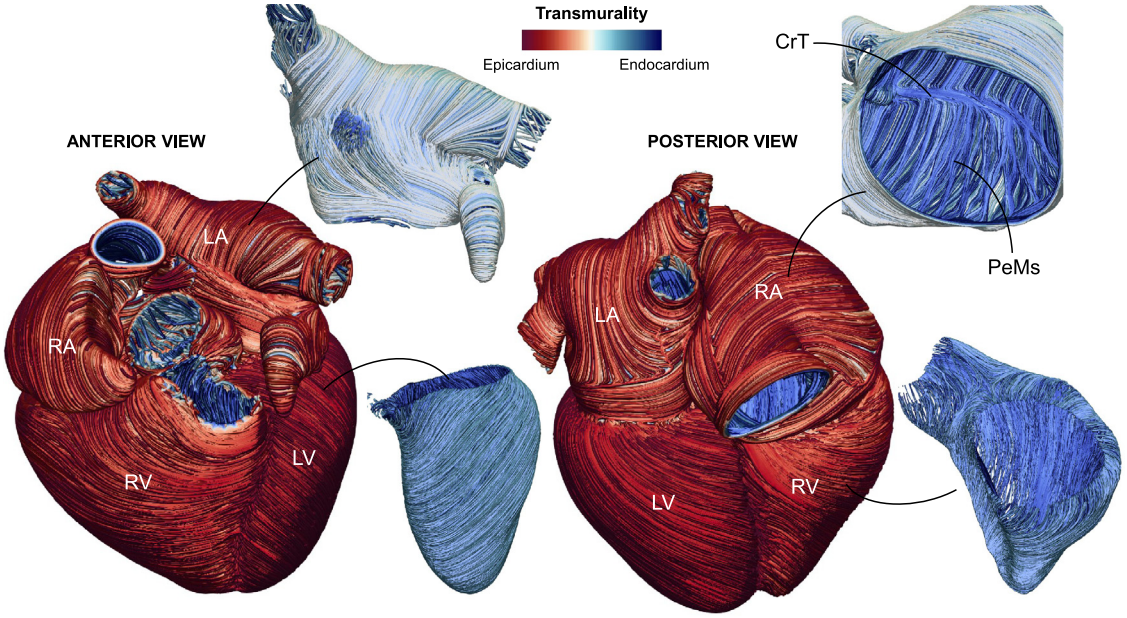

Fig. 4. The myofibers architecture of the four cardiac chambers obtained using the whole-heart Laplace–Dirichlet RBM proposed by Piersanti et al. [51,62], Piersanti [83]. The transmural variation is pointed out through anterior and posterior views of the entire epicardium and chamber-specific views of the endocardium. On the endocardium of RA also the Crista Terminalis (CrT) and the Pectinate Muscles (PeMs) are clearly visible.

where ξ_{a}, $\xi_{\mathrm{b}} \in \mathbb{R}$ are suitable Dirichlet data set on generic partitions of the heart boundary Γ_0^{a}, Γ_0^{b}, Γ_0^{n}, with $\overline{\Gamma}_0^{\mathrm{a}} \cup \overline{\Gamma}_0^{\mathrm{b}} \cup \overline{\Gamma}_0^{\mathrm{n}} = \partial\Omega_0^{\mathrm{myo}}$. In particular, the internal distances are used both to discriminate the left from the right heart and the atria from the ventricles, and also to represent different atrial and ventricular distances, characteristic of the four-chambers. Then, for each point of the cardiac computational domain, the whole-heart LDRBM suitably combines the gradients of the heart distances with the aim of defining an orthonormal local coordinate axial system $[\widehat{\boldsymbol{e}}_\ell, \widehat{\boldsymbol{e}}_{\mathrm{n}}, \widehat{\boldsymbol{e}}_{\mathrm{t}}]$ owing to $\widehat{\boldsymbol{e}}_{\mathrm{t}} = \frac{\nabla\phi}{\|\nabla\phi\|}$, $\widehat{\boldsymbol{e}}_{\mathrm{n}} = \frac{\nabla\psi_i - (\nabla\psi_i\cdot\widehat{\boldsymbol{e}}_{\mathrm{t}})\widehat{\boldsymbol{e}}_{\mathrm{t}}}{\|\nabla\psi_i - (\nabla\psi_i\cdot\widehat{\boldsymbol{e}}_{\mathrm{t}})\widehat{\boldsymbol{e}}_{\mathrm{t}}\|}$ and $\widehat{\boldsymbol{e}}_\ell = \widehat{\boldsymbol{e}}_{\mathrm{n}} \times \widehat{\boldsymbol{e}}_{\mathrm{t}}$, defined as the unit transmural, normal, and longitudinal directions, respectively. Finally, the reference frame $[\widehat{\boldsymbol{e}}_\ell, \widehat{\boldsymbol{e}}_{\mathrm{n}}, \widehat{\boldsymbol{e}}_{\mathrm{t}}]$ is properly rotated to define the myofiber orientations $[\widehat{\boldsymbol{e}}_\ell, \widehat{\boldsymbol{e}}_{\mathrm{n}}, \widehat{\boldsymbol{e}}_{\mathrm{t}}] \xrightarrow{\alpha_j,\beta_j} [\mathbf{f}_0, \mathbf{n}_0, \mathbf{s}_0]$, where $\mathbf{f}_0$ is the fiber direction, $\mathbf{n}_0$ is the sheet-normal direction, $\mathbf{s}_0$ is the sheet direction, and α_j and β_j are suitable helical and sheetlet angles following linear relationships $\theta_j(d_j) = \theta_{\mathrm{epi},j}(1 - d_j) + \theta_{\mathrm{endo},j} d_j$, (with $\theta_j = \alpha_j, \beta_j$) in which $d_j \in [0, 1]$ is the transmural normalized distance and $\theta_{\mathrm{endo},j}$, $\theta_{\mathrm{epi},j}$ are suitable prescribed rotation angles on the endocardium and epicardium of the jth heart fibers bundle.

Fig. 4 shows that the whole-heart LDRBM is able to accurately reproduce the myocardial fiber architecture, capturing the helical structure of LV, the characteristic fibers of RV, the outflow tracts regions and the fiber bundles of LA and RA, including the inter-atrial connections, the Bachmann's Bundle (BB), the Crista Terminalis (CrT) and the Pectinate Muscles (PeMs) [86,87]. In particular, these additional atrial bundles have been introduced for the first time in this work. For further details about whole-heart LDRBM we refer to [83, Chapter 4] and [62].

3.3. The full electromechanical model

A multiphysics and multiscale whole-heart electromechanical model consists of several *core models*, each of them describing biophysical processes that occur at different spatial and temporal scales during the cardiac cycle: electrophysiology, in turn consisting of ionic activity ($\mathscr{I}$) at the microscale [63,64,88–93] and electrical activity ($\mathscr{E}$) in terms of propagation of the transmembrane potential at the macroscale [94–98]; active force generation of cardiomyocites ($\mathscr{A}$) [65,73,99–101]; active and passive mechanics of the cardiac tissue ($\mathscr{M}$) [102–106]; blood circulatory system ($\mathscr{C}$) [31,107,108]. These core models are coupled to each other through some fundamental

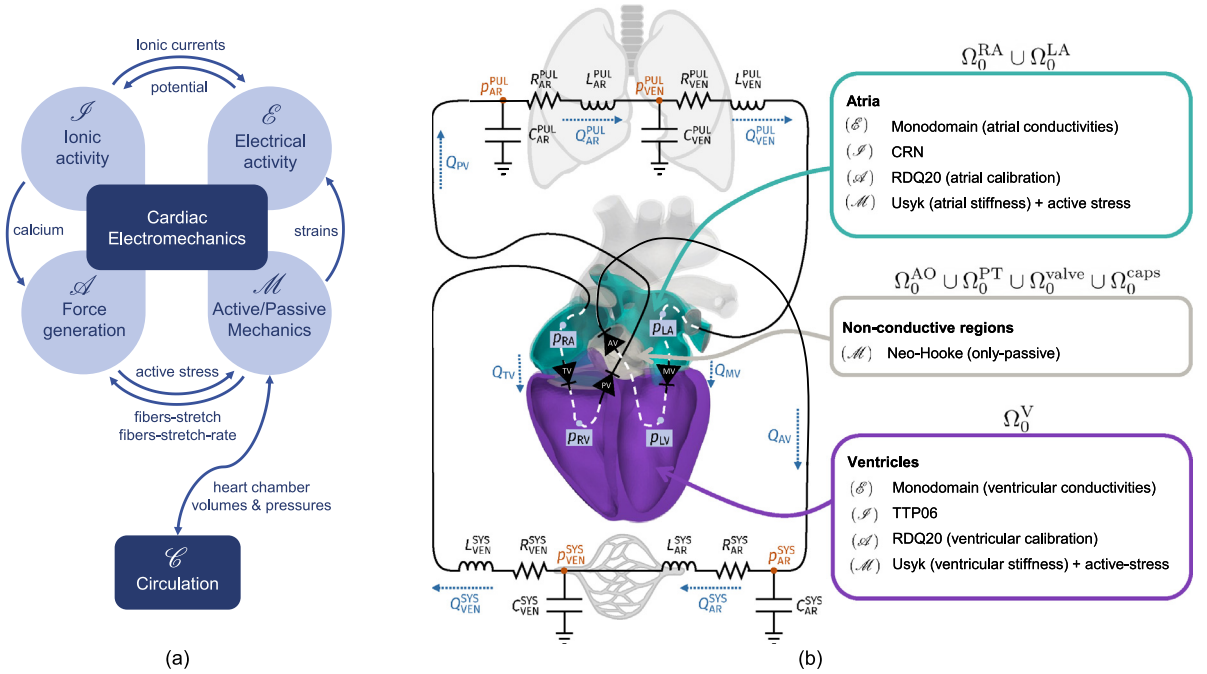

Fig. 5. A sketch of the electromechanical model. (a) The underlying *core models* and the fundamental quantities for their coupling. (b) The 0D model of the circulatory system made of resistance–inductance–capacitance (RLC) circuits for the systemic and pulmonary circulation and diodes for cardiac valves, coupled with the electromechanical model of the four 3D cardiac chambers. On the right, we highlight the models employed in the three main regions of the computational domain, i.e. atria, ventricles and non-conductive regions (*CRN*, Courtemanche et al. [63]; *TTP06*, ten Tusscher and Panfilov [64]; *RDQ20*, Regazzoni et al. [73]; *Usyk*, Usyk et al. [39].

variables or feedbacks that represent biophysical processes. In Fig. 5, (a), we sketch the variables, interactions and feedbacks that we consider in our whole-heart electromechanical model: the electrical and the ionic activities are coupled by the transmembrane potential and the ionic currents, respectively; the ionic activity determines the calcium dynamics which is of fundamental importance for the active force generation model; the cardiac mechanics is strongly influenced by the active stress provided by the force generation model which in turn is affected by the fibers-stretch and fibers-stretch-rate provided by the mechanics; the loop is closed by the influence of the mechanical strains on the electrical activity; finally, a volume conservation condition on the four cardiac chambers handles the two-way coupling between the 0D model of the circulatory system (see Fig. 5, (b)) and the 3D cardiac mechanics. More in detail, the proposed model features the following unknowns:

$$
\begin{aligned}
&u : \Omega_0^{\text{myo}} \times [0,T] \to \mathbb{R}, && \boldsymbol{w}_1 : \{\Omega_0^{\text{RA}} \cup \Omega_0^{\text{LA}}\} \times [0,T] \to \mathbb{R}^{n_{\boldsymbol{w}_1}}, && \boldsymbol{w}_2 : \Omega_0^{\text{V}} \times [0,T] \to \mathbb{R}^{n_{\boldsymbol{w}_2}},\\
&\mathbf{z} : \Omega_0^{\text{myo}} \times [0,T] \to \mathbb{R}^{n_{\mathbf{z}}}, && \mathbf{d} : \Omega_0 \times [0,T] \to \mathbb{R}^3, && \boldsymbol{c} : [0,T] \to \mathbb{R}^{n_{\boldsymbol{c}}},\\
&p_i : [0,T] \to \mathbb{R}, && i \in \{\text{RA}, \text{LA}, \text{RV}, \text{LV}\}, &&
\end{aligned}
\tag{2}
$$

where u denotes the transmembrane potential, $\boldsymbol{w}_1$ and $\boldsymbol{w}_2$ the ionic variables on atria and ventricles, respectively, $\mathbf{z}$ the state variables of the force generation model, $\mathbf{d}$ the mechanical displacement of the tissue, $\boldsymbol{c}$ the state vector of the circulation model (including pressures, volumes and fluxes in the different compartments of the vascular network), and p_{RA}, p_{LA}, p_{RV}, and p_{LV} the blood pressures inside the four cardiac chambers. The full model reads as follows:

$$
(\mathscr{E}) \quad \begin{cases}
J\chi_{\text{m}} \left[C_{\text{m}} \dfrac{\partial u}{\partial t} + \mathcal{I}_{\text{ion}}(u, \boldsymbol{w}_1, \boldsymbol{w}_2) \right] - \nabla \cdot (J\mathbf{F}^{-1} \boldsymbol{D}_{\text{M}} \mathbf{F}^{-T} \nabla u) = J\chi_{\text{m}} \mathcal{I}_{\text{app}}(t) & \text{in } \Omega_0^{\text{myo}} \times (0,T], \quad \text{(a)} \\
\left(J\mathbf{F}^{-1} \boldsymbol{D}_{\text{M}} \mathbf{F}^{-T} \nabla u \right) \cdot \mathbf{N} = 0 & \text{on } \partial\Omega_0^{\text{myo}} \times (0,T], \quad \text{(b)}
\end{cases}
\tag{3}
$$

with $u = u_0$ in Ω_0^{myo}, at time $t = 0$;

$$(\mathscr{I}) \quad \begin{cases} \dfrac{\partial \boldsymbol{w}_1}{\partial t} - \boldsymbol{H}_1(u, \boldsymbol{w}_1) = \boldsymbol{0} & \text{in } \{\Omega_0^{\text{RA}} \cup \Omega_0^{\text{LA}}\} \times (0, T], \quad \text{(a)} \\ \dfrac{\partial \boldsymbol{w}_2}{\partial t} - \boldsymbol{H}_2(u, \boldsymbol{w}_2) = \boldsymbol{0} & \text{in } \Omega_0^{\text{V}} \times (0, T], \quad \text{(b)} \end{cases} \tag{4}$$

with $\boldsymbol{w}_1 = \boldsymbol{w}_{1,0}$ in $\{\Omega_0^{\text{RA}} \cup \Omega_0^{\text{LA}}\}$ and $\boldsymbol{w}_2 = \boldsymbol{w}_{2,0}$ in Ω_0^{V}, at time $t = 0$;

$$(\mathscr{A}) \quad \left\{ \frac{\partial \mathbf{z}}{\partial t} = \boldsymbol{K}\left(\mathbf{z},\ w_{\text{Ca}},\ \text{SL},\ \frac{\partial \text{SL}}{\partial t}\right) \qquad \text{in } \Omega_0^{\text{myo}} \times (0, T], \right. \tag{5}$$

with $\mathbf{z} = \mathbf{z}_0$ in Ω_0^{myo} at time $t = 0$;

$$(\mathscr{M}) \quad \begin{cases} \rho_{\text{s}} \dfrac{\partial^2 \mathbf{d}}{\partial t^2} - \nabla \cdot \mathbf{P}(\mathbf{d}, T_{\text{a}}(\mathbf{z}, \text{SL})) = \boldsymbol{0} & \text{in } \Omega_0 \times (0, T], \quad \text{(a)} \\ \mathbf{P}(\mathbf{d}, T_{\text{a}}(\mathbf{z}, \text{SL}))\,\mathbf{N} + (\mathbf{N} \otimes \mathbf{N})\left(K_{\perp}^{\text{epi}} \mathbf{d} + C_{\perp}^{\text{epi}} \dfrac{\partial \mathbf{d}}{\partial t}\right) = \boldsymbol{0} & \text{on } \Gamma_0^{\text{epi}} \times (0, T], \quad \text{(b)} \\ \mathbf{P}(\mathbf{d}, T_{\text{a}}(\mathbf{z}, \text{SL}))\,\mathbf{N} = -p_{\text{RA}}(t)\, J\mathbf{F}^{-T}\mathbf{N} & \text{on } \Gamma_0^{\text{endo,RA}} \times (0, T], \quad \text{(c)} \\ \mathbf{P}(\mathbf{d}, T_{\text{a}}(\mathbf{z}, \text{SL}))\,\mathbf{N} = -p_{\text{LA}}(t)\, J\mathbf{F}^{-T}\mathbf{N} & \text{on } \Gamma_0^{\text{endo,LA}} \times (0, T], \quad \text{(d)} \\ \mathbf{P}(\mathbf{d}, T_{\text{a}}(\mathbf{z}, \text{SL}))\,\mathbf{N} = -p_{\text{RV}}(t)\, J\mathbf{F}^{-T}\mathbf{N} & \text{on } \Gamma_0^{\text{endo,RV}} \times (0, T], \quad \text{(e)} \\ \mathbf{P}(\mathbf{d}, T_{\text{a}}(\mathbf{z}, \text{SL}))\,\mathbf{N} = -p_{\text{LV}}(t)\, J\mathbf{F}^{-T}\mathbf{N} & \text{on } \Gamma_0^{\text{endo,LV}} \times (0, T], \quad \text{(f)} \\ \mathbf{P}(\mathbf{d}, T_{\text{a}}(\mathbf{z}, \text{SL}))\,\mathbf{N} = -p_{\text{PT}}(t)\, J\mathbf{F}^{-T}\mathbf{N} & \text{on } \Gamma_0^{\text{endo,PT}} \times (0, T], \quad \text{(g)} \\ \mathbf{P}(\mathbf{d}, T_{\text{a}}(\mathbf{z}, \text{SL}))\,\mathbf{N} = -p_{\text{AO}}(t)\, J\mathbf{F}^{-T}\mathbf{N} & \text{on } \Gamma_0^{\text{endo,AO}} \times (0, T], \quad \text{(h)} \\ \mathbf{d} = \boldsymbol{0} & \text{on } \Gamma_0^{\text{rings}} \times (0, T], \quad \text{(i)} \end{cases} \tag{6}$$

with $\mathbf{d} = \mathbf{d}_0$ and $\dfrac{\partial \mathbf{d}}{\partial t} = \dot{\mathbf{d}}_0$ in Ω_0 at time $t = 0$;

$$(\mathscr{C}) \quad \left\{ \frac{d\boldsymbol{c}(t)}{dt} = \boldsymbol{D}(t,\ \boldsymbol{c}(t),\ p_{\text{RA}}(t),\ p_{\text{LA}}(t),\ p_{\text{RV}}(t),\ p_{\text{LV}}(t)) \qquad \text{for } t \in (0, T], \right. \tag{7}$$

with $\boldsymbol{c}(0) = \boldsymbol{c}_0$ at time $t = 0$;

$$(\mathscr{V}) \quad \begin{cases} V_{\text{RA}}^{\text{3D}}(\mathbf{d}(t)) = V_{\text{RA}}^{\text{0D}}(\boldsymbol{c}(t)) & \text{for } t \in (0, T], \quad \text{(a)} \\ V_{\text{LA}}^{\text{3D}}(\mathbf{d}(t)) = V_{\text{LA}}^{\text{0D}}(\boldsymbol{c}(t)) & \text{for } t \in (0, T], \quad \text{(b)} \\ V_{\text{RV}}^{\text{3D}}(\mathbf{d}(t)) = V_{\text{RV}}^{\text{0D}}(\boldsymbol{c}(t)) & \text{for } t \in (0, T], \quad \text{(c)} \\ V_{\text{LV}}^{\text{3D}}(\mathbf{d}(t)) = V_{\text{LV}}^{\text{0D}}(\boldsymbol{c}(t)) & \text{for } t \in (0, T]. \quad \text{(d)} \end{cases} \tag{8}$$

We remark that $(\mathscr{E})$ and $(\mathscr{A})$ are both defined in the whole domain Ω_0^{myo}, but with specific parameters for atria and ventricles. Thus, since the myocardial domain is composed of the two disconnected parts $\{\Omega_0^{\text{RA}} \cup \Omega_0^{\text{LA}}\}$ and Ω_0^{V}, they behave independently in the atria and ventricles. Instead, $(\mathscr{I})$ is composed of two distinct ionic models, each one characterized by different variables and equations for the atria and ventricles. The variability of the parameters and models employed in the different regions of the heart is sketched in Fig. 5, (b).

In Section 3.3.1 to Section 3.3.4 we describe each core model (Eqs. (3) to (8)), detailing how they are coupled to each other and how they vary along the heart domain.

3.3.1. Electrophysiology $(\mathscr{E})$–$(\mathscr{I})$

Eqs. (3) and (4) represent the electrophysiological model and are solved only in the cardiac chambers Ω_0^{myo}, since the rest of the domain is made up of non-conductive regions. The model consists of the monodomain Eq. (3) – describing the propagation of the transmembrane potential u [95,98] – coupled with suitable ionic models, one for the atria in $\{\Omega_0^{\text{RA}} \cup \Omega_0^{\text{LA}}\}$ (Eq. (4)a) and one for the ventricles in Ω_0^{V} (Eq. (4)b). The vectors $\boldsymbol{w}_1 = \{w_{1,i}\}_{i=1}^{n_{\boldsymbol{w}_1}}$ and $\boldsymbol{w}_2 = \{w_{2,j}\}_{j=1}^{n_{\boldsymbol{w}_2}}$ constitute the gating variables and the concentrations of ionic species. Among them, the intracellular calcium ions concentration $[\text{Ca}^{2+}]_{\text{i}}$ plays a crucial role for active force generation. We denote this quantity with

$w_{1,\mathrm{Ca}}$ and $w_{2,\mathrm{Ca}}$ for the atria and ventricles, respectively, and we define in the whole myocardium the corresponding function w_{Ca} (used in Eq. (5)) as:

$$w_{\mathrm{Ca}} = \begin{cases} w_{1,\mathrm{Ca}}, & \text{in } \{\Omega_0^{\mathrm{RA}} \cup \Omega_0^{\mathrm{LA}}\} \times [0, T], \\ w_{2,\mathrm{Ca}}, & \text{in } \Omega_0^{\mathrm{V}} \times [0, T]. \end{cases} \tag{9}$$

We use the Courtemanche et al. [63] (CRN) model for the atria and the ten Tusscher and Panfilov [64] (TTP06) model for the ventricles, respectively. These two models are used to define the nonlinear reaction term $\mathcal{I}_{\mathrm{ion}}(u, \boldsymbol{w}_1, \boldsymbol{w}_2)$ of Eq. (3)a that models the ionic currents taking into account the multiscale effects from the cellular to the tissue level:

$$\mathcal{I}_{\mathrm{ion}}(u, \boldsymbol{w}_1, \boldsymbol{w}_2) = \begin{cases} \mathcal{I}_{\mathrm{ion}}(u, \boldsymbol{w}_1), & \text{in } \{\Omega_0^{\mathrm{RA}} \cup \Omega_0^{\mathrm{LA}}\} \times [0, T], \\ \mathcal{I}_{\mathrm{ion}}(u, \boldsymbol{w}_2), & \text{in } \Omega_0^{\mathrm{V}} \times [0, T]. \end{cases} \tag{10}$$

The monodomain model is finally closed by the no-flux Neumann boundary condition of Eq. (3)b that represents an electrically insulated domain. Moreover, since the domain Ω_0^{myo} is composed of the two disjoint parts ($\Omega_0^{\mathrm{RA}} \cup \Omega_0^{\mathrm{LA}}$ and Ω_0^{V}) separated by the insulating fibrous tissue of the atrioventricular valves (the TV and MV parts of $\Omega_0^{\mathrm{valve}}$), also the atrial and ventricular muscles are electrically insulated from each other.

The anisotropic transmission of the transmembrane potential u is regulated by the diffusion term $\nabla\cdot(J\mathbf{F}^{-1}\boldsymbol{D}_{\mathrm{M}}\mathbf{F}^{-T}\nabla u)$ of the monodomain model (Eq. (3)a) [31], where $\boldsymbol{D}_{\mathrm{M}}$ represents the diffusion tensor in the deformed configuration and $\mathbf{F} = \mathbf{I} + \nabla\mathbf{d}$ and $J = \det(\mathbf{F})$ are the deformation gradient tensor and the deformation Jacobian, respectively. Being $\mathbf{F}$ dependent on the unknown displacement $\mathbf{d}$ of the mechanical model ($\mathscr{M}$) (Eq. (6)), this diffusion term takes into account the variation of the electrical properties due to the tissue deformation, modeling the so-called Mechano-Electric Feedback (MEF) [109]. The diffusion tensor $\boldsymbol{D}_{\mathrm{M}}$ regulates the anisotropic conduction of the electrical signal using the local orthonormal coordinates system $(\mathbf{f}_0, \mathbf{s}_0, \mathbf{n}_0)$ (see Section 3.2) by prescribing three different conductivities $\sigma_{\mathbf{f}}^*$, $\sigma_{\mathbf{s}}^*$, and $\sigma_{\mathbf{n}}^*$ along the fiber, sheet normal and crossfiber directions, respectively [31,32]:

$$\boldsymbol{D}_{\mathrm{M}} = \sigma_{\mathbf{f}}^* \frac{\mathbf{f}\mathbf{f}_0 \otimes \mathbf{f}\mathbf{f}_0}{\|\mathbf{f}\mathbf{f}_0\|^2} + \sigma_{\mathbf{s}}^* \frac{\mathbf{f}\mathbf{s}_0 \otimes \mathbf{f}\mathbf{s}_0}{\|\mathbf{f}\mathbf{s}_0\|^2} + \sigma_{\mathbf{n}}^* \frac{\mathbf{f}\mathbf{n}_0 \otimes \mathbf{f}\mathbf{n}_0}{\|\mathbf{f}\mathbf{n}_0\|^2}. \tag{11}$$

In addition to varying along the local direction, the conductivities vary in space depending on the cardiac compartment:

$$\sigma_{\mathbf{k}}^* = \begin{cases} \sigma_{\mathbf{k}}^{\mathrm{A}} & \text{in } \{\Omega_0^{\mathrm{RA}} \cup \Omega_0^{\mathrm{LA}}\}, \\ \sigma_{\mathbf{k}}^{\mathrm{V}}(\phi) = \begin{cases} \sigma_{\mathbf{k}}^{\mathrm{V,myo}} & \text{if } \phi > \epsilon, \\ \sigma_{\mathbf{k}}^{\mathrm{V,endo}} & \text{if } \phi \le \epsilon, \end{cases} & \text{in } \Omega_0^{\mathrm{V}}, \end{cases} \qquad \text{for } \mathbf{k} = \mathbf{f}, \mathbf{s}, \mathbf{n}. \tag{12}$$

Following Piersanti et al. [32], the conductivities in the ventricles Ω_0^{V} also depend on a scalar function ϕ that smoothly connects the endocardium to the epicardium, allowing the definition of an endocardial layer where the electric signal propagates faster. This surrogates the PFs network [53,110] and represents a valid alternative (at least in sinus rhythm) to the generation of the PFs as a 1D network [111–114]. Instead, in the atria $\{\Omega_0^{\mathrm{RA}} \cup \Omega_0^{\mathrm{LA}}\}$, different conduction velocities of the various bundles characterize the atrial fibers morphology (see Section 3.2), varying from fast to slow conduction regions [115]. This feature is of paramount importance in the modeling of atrial electrical disorders and related pathologies [116,117]. However, as this work is focused on a healthy scenario, we do not vary the conductivities $\sigma_{\mathbf{f}}^{\mathrm{A}}$, $\sigma_{\mathbf{s}}^{\mathrm{A}}$, and $\sigma_{\mathbf{n}}^{\mathrm{A}}$ in space, considering only the variation along the local fibers orientation, as done in [51].

Finally, the forcing term $\mathcal{I}_{\mathrm{app}}(t)$ of Eq. (3)a represents an applied current that triggers the action potential of the myocardium at specific locations and times. This term is used to model a series of electrical impulses that mimic the behavior of the electrical conduction system (see Section 2 and Fig. 1, (c)), starting from the SAN and ending into a series of points on the ventricular endocardium which, combined with the fast endocardial layer, surrogate the effect of the PFs.

3.3.2. Active force generation ($\mathscr{A}$)

We model the subcellular processes by which cardiomyocytes generate an active force in response to changes in calcium concentration w_{Ca} using the model proposed by Regazzoni et al. [73] (RDQ20). RDQ20 is based on

a biophysically accurate description of the subcellular mechanisms of force generation and regulation. Despite its computational lightness (its state $\mathbf{z}$ has only 20 variables), this model explicitly describes the end-to-end interactions of tropomyosin, which are responsible for the cooperative tissue response to calcium ion concentration, manifested in a markedly enhanced sensitivity to calcium around the half-maximal effective concentration (so-called EC_{50}). Moreover, the RDQ20 model takes into account the effect of sarcomere length on the total force generated and, thanks to its explicit representation of the attachment–detachment mechanism of crossbridges, it is able to reproduce the force–velocity relationship, according to which the generated force decreases while the muscle fibers are shortening. These subcellular mechanisms are responsible for two organ-level feedbacks, namely the fibers-stretch and the fibers-stretch-rate feedback, which regulate the force generated in each region of the myocardium depending on how much and how quickly it deforms [118]. The former is related to the dependence of the model (5) on SL, while the latter is related to the dependence of the model on $\partial \mathrm{SL}/\partial t$. The variable SL represents the local sarcomere length, obtained as $\mathrm{SL} = \mathrm{SL}_0 \|\mathbf{F}\mathbf{f}_0\|$, where SL_0 is the sarcomere length at rest. The regulatory and feedback mechanisms mentioned above play a key role in the cardiac function. Nevertheless, some of them are sometimes neglected in multiscale models, due to the difficulty of capturing them in mathematical models of low computational cost and because of the difficulties involved in their numerical approximation.

The RDQ20 model describes subcellular mechanisms inherent to both atrial and ventricular cells. The model can be adapted to reproduce experimental measurements of different cell types by calibrating the parameters, which reflect the different calcium-sensitivity and kinetics of protein interactions. See [119] for an adaptation to ventricular cells and [120] for a calibration to atrial cells. Therefore, we use the same model throughout the computational domain, but with different parameter calibration to reflect the specificities of the cells belonging to the different chambers.

The tissue level active tension T_a of the RDQ20 can be defined as a nonlinear function of the state $\mathbf{z}$ and of the sarcomere length SL [73]. This quantity determines the coupling with the mechanical model (6) and contributes to the active stress part of the Piola–Kirchhoff stress tensor (see Section 3.3.3). More specifically, T_a can be written as:

$$T_\mathrm{a}(\mathbf{z}, \mathrm{SL}) = a^i_{\mathrm{XB}} G(\mathbf{z}, \mathrm{SL}), \qquad \text{for } i \in \{\mathrm{RA}, \mathrm{LA}, \mathrm{RV}, \mathrm{LV}\}, \tag{13}$$

where the microscale crossbridge stiffness a^i_{XB} links the microscopic force with the macroscopic active tension and $G(\mathbf{z}, \mathrm{SL})$ is a nonlinear function (see [73]). Thus, the organ-level contractility of each chamber is calibrated using the a^i_{XB} parameter. Moreover, in order to set a specific contractility also in the RV and LV (that belong to the same subdomain Ω_0^{V}), we use the same strategy proposed by Piersanti et al. [32] (for the previous version of the active force generation model [121]) defining the ventricular microscale crossbridge stiffness $a^{\mathrm{V}}_{\mathrm{XB}} : \Omega_0^{\mathrm{V}} \to \mathbb{R}$ as a function of space:

$$a^{\mathrm{V}}_{\mathrm{XB}}(\mathbf{x}) = a^{\mathrm{LV}}_{\mathrm{XB}} \left(\hat{\xi}(\mathbf{x}) + C_{\mathrm{lrv}}(1 - \hat{\xi}(\mathbf{x})) \right), \tag{14}$$

where $\hat{\xi} : \Omega_0^{\mathrm{V}} \to [0, 1]$ is the normalized interventricular distance [32,51] – that smoothly goes from 0 to 1 in the interventricular septum – and $C_{\mathrm{lrv}} \in \mathbb{R}$ is a coefficient that represents the left–right ventricle contractility ratio. In practical terms, this is equivalent to setting two constant values in the two ventricles (smoothly connected in the septum): $a^{\mathrm{LV}}_{\mathrm{XB}}$ in the LV and $a^{\mathrm{RV}}_{\mathrm{XB}} = C_{\mathrm{lrv}}\, a^{\mathrm{LV}}_{\mathrm{XB}}$ in the RV.

3.3.3. Active and passive mechanics ($\mathscr{M}$)

The mechanics of the cardiac tissue is modeled by the problem ($\mathscr{M}$) of Eq. (6), describing the dynamics of the tissue displacement $\mathbf{d}$ by the momentum conservation (Eq. (6)a) under the hyperelasticity assumption [102] and employing an active stress approach [122]. The active and passive mechanical properties are embedded in the Piola–Kirchhoff stress tensor $\mathbf{P}(\mathbf{d}, T_\mathrm{a}(\mathbf{z}, \mathrm{SL}))$:

$$\mathbf{P}(\mathbf{d}, T_\mathrm{a}(\mathbf{z}, \mathrm{SL})) = \begin{cases} \dfrac{\partial \mathcal{W}(\mathbf{F})}{\partial \mathbf{F}} + T_\mathrm{a}(\mathbf{z}, \mathrm{SL}) \left[n_{\mathbf{f}} \dfrac{\mathbf{F}\mathbf{f}_0 \otimes \mathbf{f}_0}{\sqrt{\mathcal{I}_{4f}}} + n_{\mathbf{n}} \dfrac{\mathbf{F}\mathbf{n}_0 \otimes \mathbf{n}_0}{\sqrt{\mathcal{I}_{4n}}} \right] & \text{in } \Omega_0^{\mathrm{myo}}, \quad \text{(a)} \\ \dfrac{\partial \mathcal{W}(\mathbf{F})}{\partial \mathbf{F}} & \text{in } \left\{ \Omega_0 \setminus \Omega_0^{\mathrm{myo}} \right\}. \quad \text{(b)} \end{cases} \tag{15}$$

The passive part of the tensor is modeled by the term $\partial \mathcal{W}(\mathbf{F})/\partial \mathbf{F}$ where $\mathcal{W}$ is the hyperelastic strain energy density function. In the myocardium Ω_0^{myo} we employ the exponential constitutive law of Usyk et al. [39], with a

volumetric term enforcing quasi-incompressibility [31,123–125]. In the non-conductive regions $\{\Omega_0 \setminus \Omega_0^{\text{myo}}\}$, instead, we use a Neo-Hookean model [102]. The resulting strain energy density function reads:

$$\mathcal{W}(\mathbf{F}) = \begin{cases} \dfrac{C^i}{2}\left(e^Q - 1\right) + \dfrac{B}{2}\left(J-1\right)\log(J), & \text{in } \Omega_0^{\text{myo}} \quad \text{(a)}, \\ \dfrac{\mu^j}{2}\left(J^{-\frac{2}{3}}\mathbf{F} : \mathbf{F} - 3\right) + \dfrac{\kappa^j}{4}\left[(J-1)^2 + \log^2(J)\right], & \text{in } \left\{\Omega_0 \setminus \Omega_0^{\text{myo}}\right\}, \quad \text{(b)} \end{cases} \tag{16}$$

where, in the Usyk et al. [39] model (16)a, $B \in \mathbb{R}^+$ represents the bulk modulus contributing to the term that realizes a weakly incompressible constraint [31], C^i, for $i \in \{\text{RA}, \text{LA}, \text{V}\}$, is the stiffness scaling parameter that assumes a specific value in each subdomain of the myocardium Ω_0^{RA}, Ω_0^{LA}, and Ω_0^{V}. Instead, in the Neo-Hookean model (16)b, μ^j and κ^j, for $j \in \{\text{valve}, \text{caps}, \text{AO}, \text{PT}\}$, are the shear modulus and the bulk modulus, respectively, and assume specific values in each non-conductive region Ω_0^{valve}, Ω_0^{caps}, Ω_0^{AO}, and Ω_0^{PT}. Finally, the term Q of the Usyk et al. [39] model (16)a reads:

$$\begin{aligned} Q &= b_{\text{ff}}E_{\text{ff}}^2 + b_{\text{ss}}E_{\text{ss}}^2 + b_{\text{nn}}E_{\text{nn}}^2 + b_{\text{fs}}\left(E_{\text{fs}}^2 + E_{\text{sf}}^2\right) + b_{\text{fn}}\left(E_{\text{fn}}^2 + E_{\text{nf}}^2\right) + b_{\text{sn}}\left(E_{\text{sn}}^2 + E_{\text{ns}}^2\right), \\ E_{\text{ab}} &= \mathbf{E}\boldsymbol{a}_0 \cdot \boldsymbol{b}_0, \qquad \text{for } a, b \in \{f, s, n\}, \end{aligned}$$

where $\mathbf{E} = \frac{1}{2}(\mathbf{C} - \mathbf{I})$ is the Green–Lagrange strain energy tensor, being $\mathbf{C} = \mathbf{F}^T\mathbf{F}$ the right Cauchy–Green deformation tensor.

The active part of the Piola–Kirchhoff stress tensor acts only in the conductive subdomains Ω_0^{myo}. This tensor depends on the active tension $T_{\text{a}}(\mathbf{z}, \text{SL})$, provided by the active force generation model (5), and on the fiber orientation in the deformed configuration. We consider the orthotropic active stress tensor (15)a, where the coefficients $\mathcal{I}_{4f}$ and $\mathcal{I}_{4n}$ (equal to $\mathbf{Fk} \cdot \mathbf{Fk}$, for $\mathbf{k} = \mathbf{f}_0, \mathbf{n}_0$) represent the tissue stretches along the fiber and sheet-normal directions, respectively, while $n_{\mathbf{f}}$ and $n_{\mathbf{n}}$ model the proportion of active tension along these directions [32]. In this way the active stress tensor can mainly act in the fiber direction $\mathbf{f}$ while also being partially applied in the cross-fiber direction $\mathbf{n}$. This surrogates the contraction caused by the dispersed myofibers [126,127]. The effect of including cross-fiber active contraction in an electromechanical model has been extensively discussed by Piersanti et al. [32]. The parameters used for $n_{\mathbf{f}}$ and $n_{\mathbf{n}}$ are reported in Table A.4. The mechanical model is closed by the boundary conditions of Eq. (6)b to Eq. (6)i. On the epicardium Γ_0^{epi} we apply the Robin-like condition (6)b originally proposed in the whole heart by Pfaller et al. [49]. This condition surrogates the pressure exerted by the pericardium and surrounding organs on the external cardiac surface by penalizing only the normal displacement [49,50]. No constraints are added on the other directions as the pericardial fluid allows free sliding within the pericardial sac [49,50]. Instead, an additional constraint on the tangential direction can be necessary to avoid rigid rotation when the computational domain consists of the sole ventricles [31]. The calibration of the pericardial stiffness $K_{\perp}^{\text{epi}}$ of Eq. (6)b plays a fundamental role in the realistic movement of the heart [49,50]. Pfaller et al. [49] have tested different constant values on the whole external cardiac surface, but they model the EAT as a 3D subdomain. More recently, Strocchi et al. [50] have proposed a spatially varying coefficient to surrogate the different stiffness of the organs in contact with the pericardial sac, without including the EAT as a 3D subdomain. Inspired by both of these works, we vary the $K_{\perp}^{\text{epi}}$ only between two regions: we prescribe a stiffer value on $\Gamma_0^{\text{epi,PF}}$ – where the external organs are in contact with the pericardium – and a much lower value $K_{\perp}^{\text{epi,EAT}}$ on $\Gamma_0^{\text{epi,EAT}}$ — where the presence of the EAT leaves the ventricular base and the lower part of the LAA and RAA more free to move.

On the endocardium and endothelium surfaces, we apply the normal stress boundary conditions of Eq. (6)c to Eq. (6)h that model the pressure exerted by the blood. The blood pressure of the various chambers and arteries depends on the circulation model (7), as detailed in Section 3.3.4. Finally, we apply the homogeneous Dirichlet boundary condition (6)i on all the artificial boundaries Γ_0^{rings}, since the arteries and veins can be considered almost fixed where we cut the computational domain (see Fig. 3).

3.3.4. Blood circulation ($\mathscr{C}$) and 3D-0D coupling ($\mathscr{V}$)

We model the blood circulatory system using the 0D lumped-parameter closed-loop model proposed by Regazzoni et al. [31] and inspired by Blanco and Feijóo [107], Hirschvogel et al. [108]. In this model, as sketched in Fig. 5, (b), resistance–inductance–capacitance (RLC) circuits represent the systemic (SYS) and pulmonary (PUL) circulations in both their arterial (AR) and venous (VEN) compartments, while non-ideal diodes model the four

cardiac valves. The state vector $\boldsymbol{c}$ comprises the volumes of the cardiac chambers and the systemic/pulmonary arterial/venous pressures and flow rates:

$$\boldsymbol{c}(t) = \left(V_{\mathrm{RA}}(t),\, V_{\mathrm{LA}}(t),\, V_{\mathrm{RV}}(t),\, V_{\mathrm{LV}}(t),\, p_{\mathrm{AR}}^{\mathrm{SYS}}(t),\, p_{\mathrm{VEN}}^{\mathrm{SYS}}(t),\, p_{\mathrm{AR}}^{\mathrm{PUL}}(t),\, p_{\mathrm{VEN}}^{\mathrm{PUL}}(t),\, Q_{\mathrm{AR}}^{\mathrm{SYS}}(t),\, Q_{\mathrm{VEN}}^{\mathrm{SYS}}(t),\, Q_{\mathrm{AR}}^{\mathrm{PUL}}(t),\, Q_{\mathrm{VEN}}^{\mathrm{PUL}}(t) \right).$$

The corresponding ODE system ($\mathscr{C}$), summarized by Eq. (7), reads:

$$\begin{cases} C_{\mathrm{VEN}}^{\mathrm{SYS}} \dfrac{dp_{\mathrm{VEN}}^{\mathrm{SYS}}(t)}{dt} = Q_{\mathrm{AR}}^{\mathrm{SYS}}(t) - Q_{\mathrm{VEN}}^{\mathrm{SYS}}(t), & C_{\mathrm{VEN}}^{\mathrm{PUL}} \dfrac{dp_{\mathrm{VEN}}^{\mathrm{PUL}}(t)}{dt} = Q_{\mathrm{AR}}^{\mathrm{PUL}}(t) - Q_{\mathrm{VEN}}^{\mathrm{PUL}}(t), \\ \dfrac{L_{\mathrm{VEN}}^{\mathrm{SYS}}}{R_{\mathrm{VEN}}^{\mathrm{SYS}}} \dfrac{dQ_{\mathrm{VEN}}^{\mathrm{SYS}}(t)}{dt} = -Q_{\mathrm{VEN}}^{\mathrm{SYS}}(t) - \dfrac{p_{\mathrm{RA}}(t) - p_{\mathrm{VEN}}^{\mathrm{SYS}}(t)}{R_{\mathrm{VEN}}^{\mathrm{SYS}}}, & \dfrac{L_{\mathrm{VEN}}^{\mathrm{PUL}}}{R_{\mathrm{VEN}}^{\mathrm{PUL}}} \dfrac{dQ_{\mathrm{VEN}}^{\mathrm{PUL}}(t)}{dt} = -Q_{\mathrm{VEN}}^{\mathrm{PUL}}(t) - \dfrac{p_{\mathrm{LA}}(t) - p_{\mathrm{VEN}}^{\mathrm{PUL}}(t)}{R_{\mathrm{VEN}}^{\mathrm{PUL}}}, \\ \dfrac{dV_{\mathrm{RA}}(t)}{dt} = Q_{\mathrm{VEN}}^{\mathrm{SYS}}(t) - Q_{\mathrm{TV}}(p_{\mathrm{RA}}(t),\, p_{\mathrm{RV}}(t)), & \dfrac{dV_{\mathrm{LA}}(t)}{dt} = Q_{\mathrm{VEN}}^{\mathrm{PUL}}(t) - Q_{\mathrm{MV}}(p_{\mathrm{LA}}(t),\, p_{\mathrm{LV}}(t)), \\ \dfrac{dV_{\mathrm{RV}}(t)}{dt} = Q_{\mathrm{TV}}(p_{\mathrm{RA}}(t),\, p_{\mathrm{RV}}(t)) - Q_{\mathrm{PV}}(p_{\mathrm{RV}}(t),\, p_{\mathrm{AR}}^{\mathrm{PUL}}(t)), & \dfrac{dV_{\mathrm{LV}}(t)}{dt} = Q_{\mathrm{MV}}(p_{\mathrm{LA}}(t),\, p_{\mathrm{LV}}(t)) - Q_{\mathrm{AV}}(p_{\mathrm{LV}}(t),\, p_{\mathrm{AR}}^{\mathrm{SYS}}(t)), \\ C_{\mathrm{AR}}^{\mathrm{PUL}} \dfrac{dp_{\mathrm{AR}}^{\mathrm{PUL}}(t)}{dt} = Q_{\mathrm{PV}}(p_{\mathrm{RV}}(t),\, p_{\mathrm{AR}}^{\mathrm{PUL}}(t)) - Q_{\mathrm{AR}}^{\mathrm{PUL}}(t), & C_{\mathrm{AR}}^{\mathrm{SYS}} \dfrac{dp_{\mathrm{AR}}^{\mathrm{SYS}}(t)}{dt} = Q_{\mathrm{AV}}(p_{\mathrm{LV}}(t),\, p_{\mathrm{AR}}^{\mathrm{SYS}}(t)) - Q_{\mathrm{AR}}^{\mathrm{SYS}}(t), \\ \dfrac{L_{\mathrm{AR}}^{\mathrm{PUL}}}{R_{\mathrm{AR}}^{\mathrm{PUL}}} \dfrac{dQ_{\mathrm{AR}}^{\mathrm{PUL}}(t)}{dt} = -Q_{\mathrm{AR}}^{\mathrm{PUL}}(t) - \dfrac{p_{\mathrm{VEN}}^{\mathrm{PUL}}(t) - p_{\mathrm{AR}}^{\mathrm{PUL}}(t)}{R_{\mathrm{AR}}^{\mathrm{PUL}}}, & \dfrac{L_{\mathrm{AR}}^{\mathrm{SYS}}}{R_{\mathrm{AR}}^{\mathrm{SYS}}} \dfrac{dQ_{\mathrm{AR}}^{\mathrm{SYS}}(t)}{dt} = -Q_{\mathrm{AR}}^{\mathrm{SYS}}(t) - \dfrac{p_{\mathrm{VEN}}^{\mathrm{SYS}}(t) - p_{\mathrm{AR}}^{\mathrm{SYS}}(t)}{R_{\mathrm{AR}}^{\mathrm{SYS}}}, \end{cases} \tag{17}$$

with $t \in [0, T]$ and where the flow rates of the valves read:

$$Q_{\mathrm{i}}(p_1, p_2) = \begin{cases} \dfrac{p_1 - p_2}{R_{\min}}, & \text{if } p_1 < p_2 \\ \dfrac{p_1 - p_2}{R_{\max}}, & \text{if } p_1 \geq p_2 \end{cases} \qquad \text{for } i \in \{\mathrm{TV}, \mathrm{MV}, \mathrm{PV}, \mathrm{AV}\}, \tag{18}$$

where p_1 and p_2 denote the proximal and distal pressures of the valve, whereas $R_{\min}$ and $R_{\max}$ are its minimum and maximum resistance [31].

While in the fully 0D model the four cardiac chambers consists of time-varying elastance elements [31], in the 3D-0D whole-heart model the pressure–volume relationships of each chamber is provided by the 3D electromechanical model and must satisfy the volume-consistency conditions ($\mathscr{V}$) of Eq. (8), where $V_i^{\mathrm{0D}}(\boldsymbol{c}(t)) = V_i(t)$, for $i \in \{\mathrm{RA}, \mathrm{LA}, \mathrm{RV}, \mathrm{LV}\}$, represent the volumes of the four cardiac chambers in the 0D circulation model, while the 3D volumes are computed using the divergence (Gauss) theorem on the closed endocardial surfaces of the four cardiac chambers:

$$V_i^{\mathrm{3D}}(\mathbf{d}(\mathbf{x}, t)) = \frac{1}{3} \int_{\Gamma^{\mathrm{endo},i}} J(\mathbf{x}, t)\, (\mathbf{x} + \mathbf{d}(\mathbf{x}, t)) \cdot \mathbf{F}^{-T}(\mathbf{x}, t)\, \mathbf{N}(\mathbf{x})\, d\mathbf{x}, \qquad i \in \{\mathrm{RA}, \mathrm{LA}, \mathrm{RV}, \mathrm{LV}\}. \tag{19}$$

We remark that these volumes can be exactly computed since the endocardial surfaces $\Gamma^{\mathrm{endo},i}$ are closed surfaces thanks to the presence of the valves $\Omega_0^{\mathrm{valve}}$ and of the artificial caps Ω_0^{caps} (see Fig. 3). The resulting model ($\mathscr{C}$)–($\mathscr{V}$) of Eqs. (7) and (8) consists of $n_{\boldsymbol{c}} + 4$ equations and unknowns, where the four additional unknowns are the chamber pressures ($p_{\mathrm{RA}}(t)$, $p_{\mathrm{LA}}(t)$, $p_{\mathrm{RV}}(t)$, $p_{\mathrm{LV}}(t)$) that act as Lagrange multipliers enforcing the volume-consistency constraints. These four pressures take into account the coupling with the ($\mathscr{M}$) model through the normal stress boundary conditions of Eqs. (6)c to (6)f applied on the endocardium of the four chambers. Instead, on the endothelium of the PT and AO we apply the pulmonary and systemic arterial pressures by setting $p_{\mathrm{PT}}(t) = p_{\mathrm{AR}}^{\mathrm{PUL}}(t)$ and $p_{\mathrm{AO}}(t) = p_{\mathrm{AR}}^{\mathrm{SYS}}(t)$ in Eqs. (6)g and (6)h, respectively.

3.4. Reference configuration and initial displacement

The most interesting applications of computational cardiac electromechanics occur when the human heart domain is directly reconstructed from medical images, with the aim of performing patient-specific simulations. However, these reconstructed geometries correspond to a configuration $\widetilde{\Omega}$ loaded by the internal blood pressure while, on the contrary, the stress–strain relationship at the basis of the mechanical model ($\mathscr{M}$) is formulated in an unloaded (stress-free) configuration Ω_0 (see Eq. (15)). In order to recover this reference configuration Ω_0 from the imaging

configuration $\widetilde{\Omega}$ we extend the procedure proposed by Regazzoni et al. [31] for the LV to the whole heart: starting from $\widetilde{\Omega}$, we recover the configuration Ω_0 by virtually deflating the whole-heart domain previously subject to the internal pressures $\widetilde{p}_i$, for $i \in \{\text{RA, LA, RV, LV, PT, AO}\}$; then, by applying on the endocardium and endothelium the pressures $p_{i,0}$, we inflate the domain again in order to compute the displacement $\mathbf{d}_0$ for the initial condition of the mechanical problem ($\mathscr{M}$) of Eq. (6). The whole procedure is sketched in Fig. 6.

Both these two steps are performed by assuming a quasi-static approximation of the mechanical problem (6) [31]. This hypothesis is reasonable only in a few moments of the cardiac cycle, such as at the end of the VPF phase just before the beginning of the AC phase (see Section 2 and Fig. 2). Indeed, at this time of the diastole, the ventricular filling slows down and the movement of the four chambers becomes negligible. This moment is usually captured in standard cardiac medical images, because on the one hand it is easy to identify using the ECG signal, on the other hand the image quality is better when the heart moves slowly. Furthermore, the small blood pressures that load the heart chambers during this phase make the associated numerical problem less challenging to solve.

More in detail, the procedure is based on the following quasi-static approximation, obtained by neglecting the time derivative term of Eq. (6)a in the mechanical problem ($\mathscr{M}$):

$$
\left(\mathscr{M}^{\text{static}}\right)
\begin{cases}
\nabla \cdot \mathbf{P}(\mathbf{d}, \overline{T}_{\text{a}}) = \mathbf{0} & \text{in } \Omega_0 \times (0,T], \quad \text{(a)} \\
\mathbf{P}(\mathbf{d}, \overline{T}_{\text{a}})\,\mathbf{N} + (\mathbf{N}\otimes\mathbf{N})\left(K_{\perp}^{\text{epi}}\mathbf{d} + C_{\perp}^{\text{epi}}\dfrac{\partial \mathbf{d}}{\partial t}\right) = \mathbf{0} & \text{on } \Gamma_0^{\text{epi}} \times (0,T], \quad \text{(b)} \\
\mathbf{P}(\mathbf{d}, \overline{T}_{\text{a}})\,\mathbf{N} = -\overline{p}_{\text{RA}}\, J\mathbf{F}^{-T}\mathbf{N} & \text{on } \Gamma_0^{\text{endo,RA}} \times (0,T], \quad \text{(c)} \\
\mathbf{P}(\mathbf{d}, \overline{T}_{\text{a}})\,\mathbf{N} = -\overline{p}_{\text{LA}}\, J\mathbf{F}^{-T}\mathbf{N} & \text{on } \Gamma_0^{\text{endo,LA}} \times (0,T], \quad \text{(d)} \\
\mathbf{P}(\mathbf{d}, \overline{T}_{\text{a}})\,\mathbf{N} = -\overline{p}_{\text{RV}}\, J\mathbf{F}^{-T}\mathbf{N} & \text{on } \Gamma_0^{\text{endo,RV}} \times (0,T], \quad \text{(e)} \\
\mathbf{P}(\mathbf{d}, \overline{T}_{\text{a}})\,\mathbf{N} = -\overline{p}_{\text{LV}}\, J\mathbf{F}^{-T}\mathbf{N} & \text{on } \Gamma_0^{\text{endo,LV}} \times (0,T], \quad \text{(f)} \\
\mathbf{P}(\mathbf{d}, \overline{T}_{\text{a}})\,\mathbf{N} = -\overline{p}_{\text{PT}}\, J\mathbf{F}^{-T}\mathbf{N} & \text{on } \Gamma_0^{\text{endo,PT}} \times (0,T], \quad \text{(g)} \\
\mathbf{P}(\mathbf{d}, \overline{T}_{\text{a}})\,\mathbf{N} = -\overline{p}_{\text{AO}}\, J\mathbf{F}^{-T}\mathbf{N} & \text{on } \Gamma_0^{\text{endo,AO}} \times (0,T], \quad \text{(h)} \\
\mathbf{d} = \mathbf{0} & \text{on } \Gamma_0^{\text{rings}} \times (0,T], \quad \text{(i)}
\end{cases}
\tag{20}
$$

where $\overline{T}_{\text{a}} = \overline{T}_{\text{a},i} > 0$, for $i \in \{\text{RA, LA, RV, LV}\}$, represents the residual active tension fixed to a constant value in each cardiac chamber and $\overline{p}_i$, for $i \in \{\text{RA, LA, RV, LV, PT, AO}\}$, are the constant pressures loading the endocardium and the endothelium. Being $\mathbf{x}_0$ the coordinates associated to Ω_0, the solution $\overline{\mathbf{d}} = \mathbf{d}(\mathbf{x}_0, \overline{p}_i, \overline{T}_{\text{a}})$ of Eq. (20) can be used to move the coordinate $\mathbf{x}_0$ into a coordinate $\overline{\mathbf{x}} = \mathbf{x}_0 + \overline{\mathbf{d}}$ corresponding to a loaded configuration $\overline{\Omega}$. Thus, in order to recover the unloaded configuration Ω_0 starting from the imaging configuration $\widetilde{\Omega}$, we need to solve the following inverse problem: find the domain Ω_0 such that, if we displace $\mathbf{x}_0$ by the solution $\widetilde{\mathbf{d}} = \mathbf{d}(\mathbf{x}_0, \widetilde{p}_i, \widetilde{T}_{\text{a}})$ of Eq. (20), we get the coordinate $\widetilde{\mathbf{x}}$ of the domain $\widetilde{\Omega}$, i.e. $\widetilde{\mathbf{x}} = \mathbf{x}_0 + \widetilde{\mathbf{d}}$. To solve this problem we employ the algorithm proposed in [31,128], that is based on a fixed point method augmented with an adaptive step continuation method to ensure stability and boost convergence speed.

Finally, once the reference configuration Ω_0 has been recovered, we can set proper values of $\overline{p}_i = p_{i,0}$ and $\overline{T}_{\text{a}} = T_{\text{a},0}$ corresponding to the phase of the cardiac cycle at the initial time $t = 0$ of the unsteady electromechanical model and solve again Eq. (20). In this way, we obtain the initial condition $\mathbf{d}_0 = \mathbf{d}(\mathbf{x}_0, p_{i,0}, T_{\text{a},0})$ for the unsteady mechanical problem ($\mathscr{M}$) of Eq. (6). Note that, in principle, the phase of the cardiac cycle corresponding to the initial time $t = 0$ and the time when the imaging configuration $\widetilde{\Omega}$ is acquired can be different, justifying possible different values of $\overline{T}_{\text{a}}$ and $\overline{p}_i$ during the reference configuration recovery and the initial displacement computation. In this specific work, since the imaging configuration and the initial time are coherent, we adopt the same pressures $\overline{p}_i$ and active tension residual $\overline{T}_{\text{a}}$ values for both the reference configuration recovery ($\widetilde{p}_i$, $\widetilde{T}_{\text{a}}$) and the initial displacement computation ($p_{i,0}$, $T_{\text{a},0}$), see Table A.5.

4. Numerical approximation

For the numerical approximation of the whole-heart electromechanical model (Eqs. (3) to (8)) we extend to the four-chamber case the segregated-intergrid-staggered numerical approach introduced for the ventricular cases in [31,32]. In this numerical scheme the core models are sequentially solved in a segregated manner, using different resolutions in space and time to properly take into account the heterogeneous space and time scales that characterize

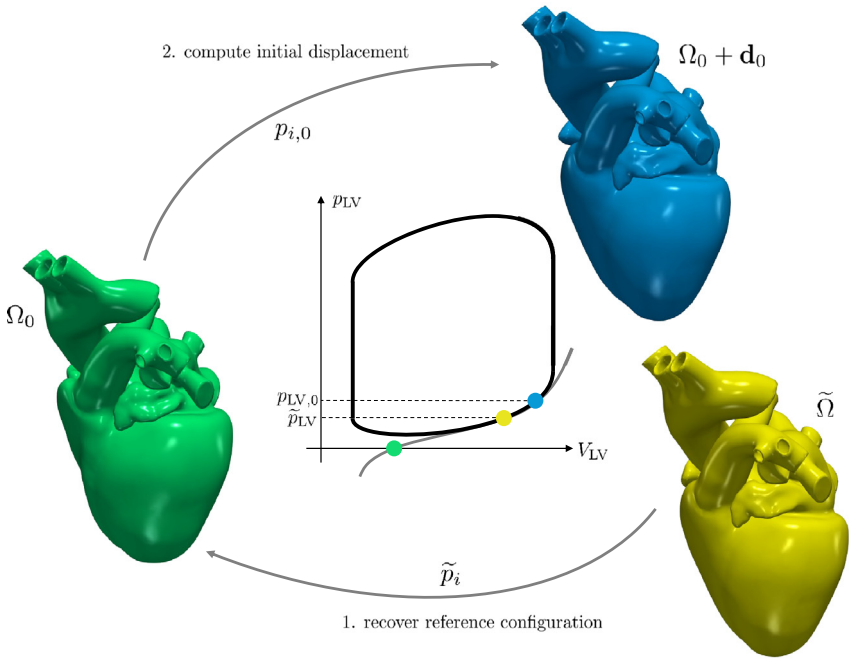

Fig. 6. A sketch of the procedure to recover the reference configuration and to compute the initial displacement. In yellow, the loaded configuration $\widetilde{\Omega}$ (reconstructed from in-vivo medical images). In green, the deflated reference configuration Ω_0; in blue, the configuration inflated by the initial displacement $\mathbf{d}_0$. We also report the three configurations in the LV pressure–volume loop. (For interpretation of the references to color in this figure legend, the reader is referred to the web version of this article.)

the different core models [27,44,129]. However, extending this scheme to the whole-heart mathematical model presented in Section 3 is not a simple task. As a matter of fact, several additional challenges must be addressed, including the fibers-stretch-rate feedback, the presence of interconnected chambers, and the solution of some core models only within the conductive subset of the computational domain. In the subsequent sections, we focus on the novel approaches we propose to surmount these obstacles, with a particular emphasis on the handling of non-conductive regions and the introduction of specific stabilization terms. A sketch of the whole numerical scheme is shown in Fig. 7, highlighting how the different core models are separately solved, which variables interconnect them, and which interactions need numerical stabilization.

4.1. Numerical approximation of the core models

For the time discretization, we employ Backward Differentiation Formula (BDF) schemes [130]. The ($\mathscr{E}$) and ($\mathscr{I}$) models are solved using a BDF of order 2 (BDF2), using an Implicit–Explicit (IMEX) scheme, denoted by ($\mathscr{E}_{\mathrm{IMEX}}$) and ($\mathscr{I}_{\mathrm{IMEX}}$), respectively, where the diffusion term is treated implicitly, the reaction term is treated explicitly and the ionic variables are advanced through the IMEX scheme of [31,32]. Moreover, the discretization of the ionic current term $\mathcal{I}_{\mathrm{ion}}$ is performed following the Ionic Current Interpolation (ICI) approach [131]. Both ($\mathscr{M}$) and ($\mathscr{A}$) models are advanced in time with a BDF of order 1 (BDF1) scheme, with an IMEX scheme for the activation ($\mathscr{A}_{\mathrm{IMEX}}$) [73] and a fully implicit scheme for the mechanical problem ($\mathscr{M}_{\mathrm{I}}$) [31,32]. Finally, we use an explicit BDF1 scheme for the circulation ($\mathscr{C}_{\mathrm{E}}$) [83].

Concerning the space discretization, we use the FE Method with continuous FEs and tetrahedral meshes [130]. We consider a unique mesh $\mathcal{T}_h$ (h represents the mesh size) for the entire computational domain Ω_0 (see Fig. 9, (a)). We employ a scalable and efficient intergrid transfer operator on the unique mesh $\mathcal{T}_h$ that enables the use of arbitrary FEs among the different core models. In particular, we consider FE of order 2 ($\mathbb{P}_2$) for ($\mathscr{E}_{\mathrm{IMEX}}$) to properly capture the dynamics of traveling waves, and FE of order 1 ($\mathbb{P}_1$) for both ($\mathscr{A}_{\mathrm{IMEX}}$) and ($\mathscr{M}_{\mathrm{I}}$) [26,31,32,132].

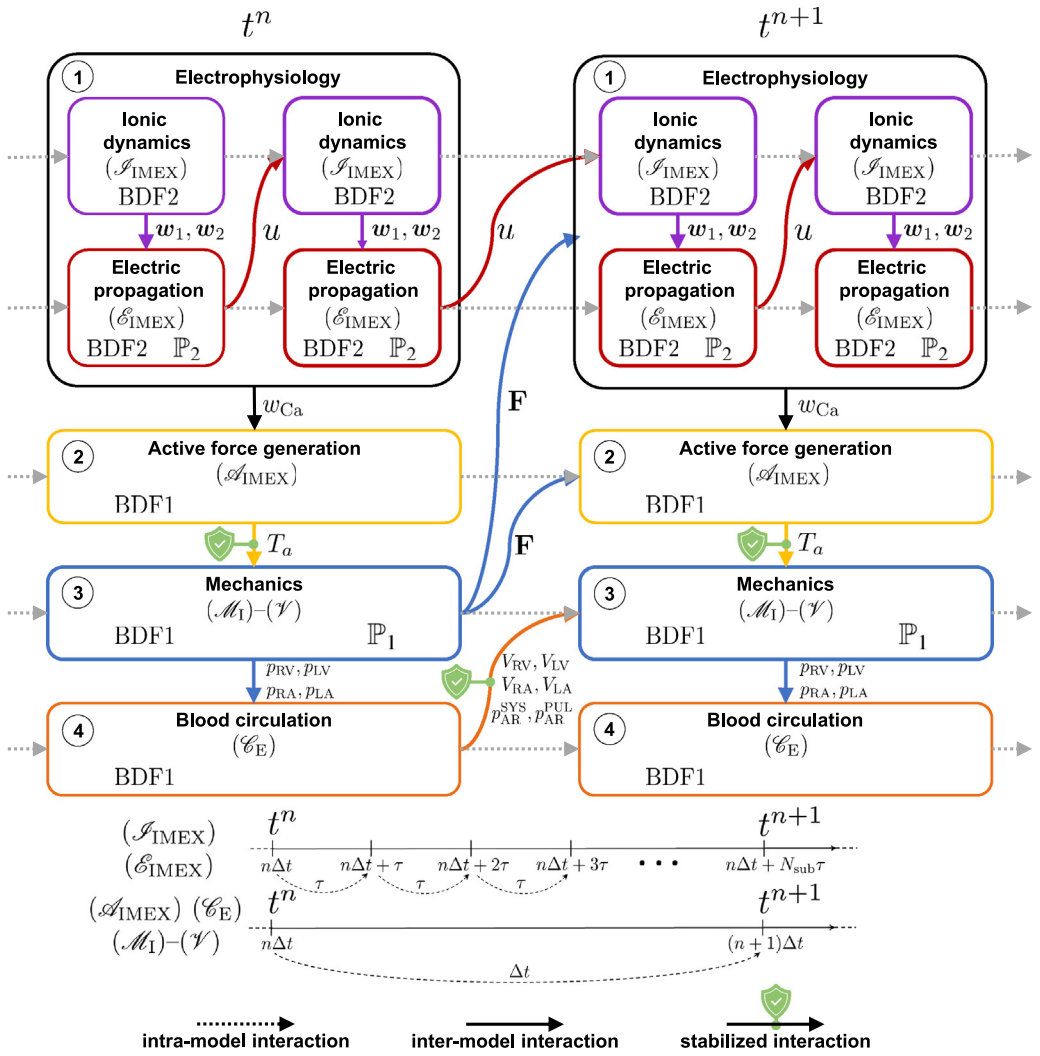

Fig. 7. A sketch of the segregated-intergrid-staggered numerical scheme. Each block represents a core model and we show their order of resolution, which variables interconnect them and which interactions need stabilization. We also highlight the time and space discretization employed. Note that the electrophysiological block, being solved using a smaller timestep, features several repeated solutions of the ($\mathscr{E}_{\text{IMEX}}$) and ($\mathscr{I}_{\text{IMEX}}$) blocks for each time t^n of the ($\mathscr{A}_{\text{IMEX}}$)–($\mathscr{M}_{\text{I}}$)–($\mathscr{V}$)–($\mathscr{C}_{\text{E}}$) blocks (in the figure, for illustrative purposes, only two sub-steps are displayed).

4.2. Parallel implementation of the conductive and non-conductive regions

The models ($\mathscr{E}_{\text{IMEX}}$)–($\mathscr{I}_{\text{IMEX}}$)–($\mathscr{A}_{\text{IMEX}}$) are only defined in the subdomain Ω_0^{myo}. Since Ω_0^{myo} is composed of the disjoint subsets Ω_0^{A} and Ω_0^{V}, in principle it would be possible to solve said models on those subsets independently. However, all these models must communicate with ($\mathscr{M}$) (through the electro-mechanical and mechano-electrical feedbacks, as well as through SL and $\partial \text{SL}/\partial t$), which is instead defined over the whole domain Ω_0. Solving ($\mathscr{E}_{\text{IMEX}}$)–($\mathscr{I}_{\text{IMEX}}$)–($\mathscr{A}_{\text{IMEX}}$) on the disjoint subsets independently would pose significant technical challenges related to the communication of data between the subsets and the whole domain. These difficulties become even more significant in a parallel computing context, where each of the domains would be distributed over multiple processes.

To avoid these issues, we employ a different strategy in which the models ($\mathscr{E}_{\text{IMEX}}$)–($\mathscr{I}_{\text{IMEX}}$)–($\mathscr{A}_{\text{IMEX}}$) are implemented in the whole domain Ω_0. Each element of the mesh $\mathcal{T}_h$, as sketched in Fig. 8, is marked as being conductive if it belongs to Ω_0^{myo}, and non-conductive otherwise. Similarly, DOFs are marked as conductive if they

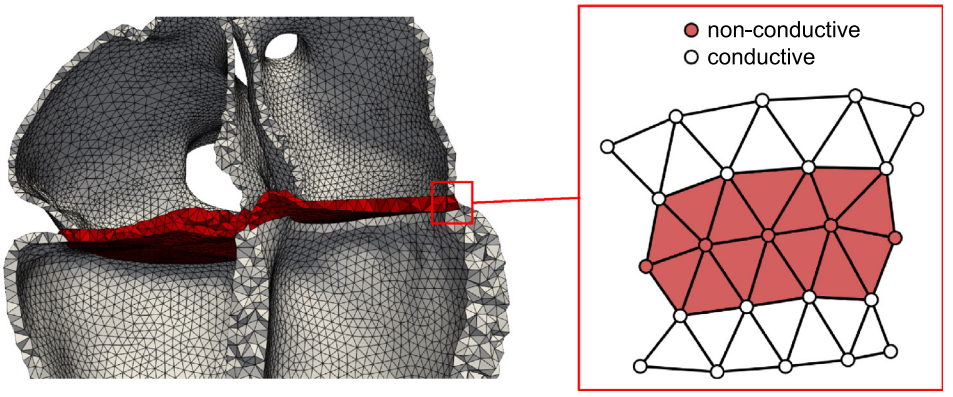

Fig. 8. Representation of the conductive (white) and non-conductive (red) cells and Degrees Of Freedom (DOFs): on the left an internal view of a whole-heart mesh; on the right a 2D schematic representation of the conductive and non-conductive cells and DOFs. (For interpretation of the references to color in this figure legend, the reader is referred to the web version of this article.)

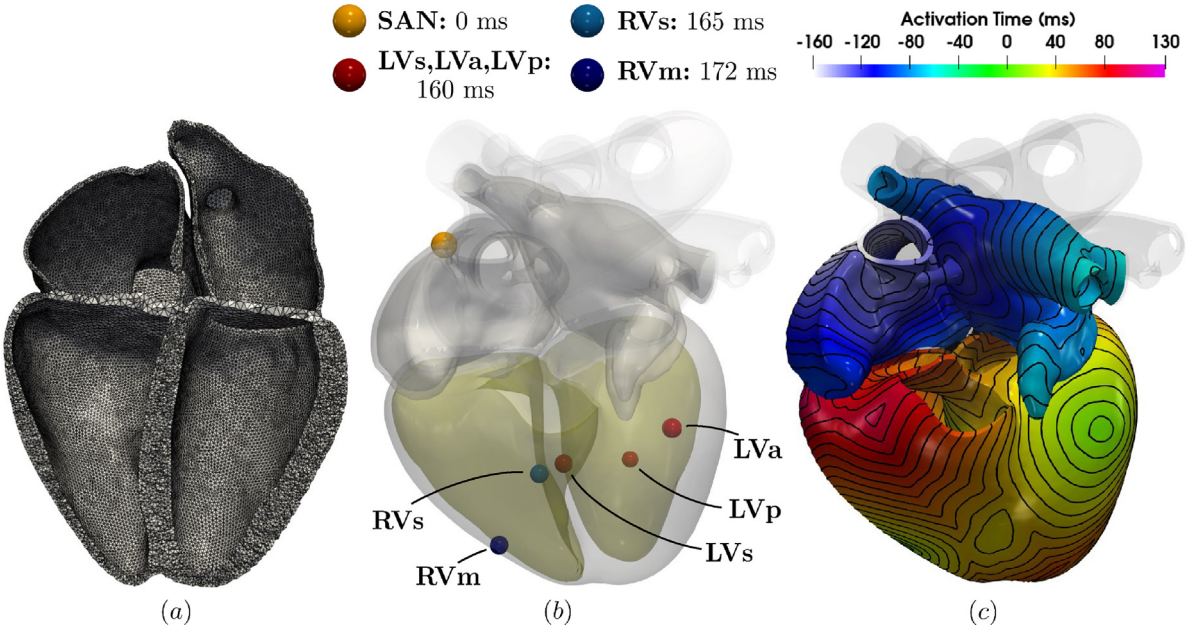

Fig. 9. (a) A cut view of the computational mesh. (b) The stimulation protocol highlighting the location and time of the applied spherical impulses. (c) The baseline simulation results in term of activation time. The activation time has been shifted to the reference initial time taken at the onset of the left ventricular activation (160 ms). Hence, the atrial activation is reported with negative values. The distance between the isochrones is 5 ms.

are supported on at least one conductive element, and non-conductive otherwise. We solve ($\mathscr{I}_{\text{IMEX}}$) and ($\mathscr{A}_{\text{IMEX}}$) on the conductive DOFs only. When assembling the monodomain Eq. (3)a, we only loop over the conductive elements (and do nothing for the non-conductive elements): this imposes in a natural (and computationally efficient) way the homogeneous Neumann condition (3)b on the internal interfaces between the conductive and non-conductive regions, thus allowing the non-conductive regions to serve as electrical insulators (see also the numerical test performed in Appendix B). Non-conductive DOFs are constrained to an arbitrary value, to ensure the well-posedness of the resulting algebraic system.

This strategy has several advantages for what concerns the convenience of implementation and distributed parallel computing. Indeed, it allows to use the same mesh for all models, which greatly facilitates exchanging variables among them. Moreover, the DOFs are naturally distributed among the parallel processes in a way that is

consistent across the different core models, and perfectly balances the load. This minimizes the amount of parallel communication, thus resulting in an efficient implementation. All these aspects would require a more complex implementation if the models ($\mathscr{E}_{\text{IMEX}}$)–($\mathscr{I}_{\text{IMEX}}$)–($\mathscr{A}_{\text{IMEX}}$) were solved independently on the disjoint domains Ω_0^{A} and Ω_0^{V}.

4.3. Numerical coupling of the core models

We adopt a segregated approach to couple the different core models, solving them in a sequential manner. Moreover, we make use of two different time steps, a larger one (denoted by Δt) for ($\mathscr{A}_{\text{IMEX}}$)–($\mathscr{M}_{\text{I}}$)–($\mathscr{V}$)–($\mathscr{C}_{\text{E}}$) and a finer one (that is $\tau = \Delta t / N_{\text{sub}}$) for ($\mathscr{E}_{\text{IMEX}}$)–($\mathscr{I}_{\text{IMEX}}$), with $N_{\text{sub}} \in \mathbb{N}$, see Fig. 7(b). As shown in Fig. 7, we update the variables in the following order: first, we update ($\mathscr{I}_{\text{IMEX}}$) and ($\mathscr{E}_{\text{IMEX}}$), by performing N_{sub} sub-steps; then, we update ($\mathscr{A}_{\text{IMEX}}$); successively, we update ($\mathscr{M}_{\text{I}}$) together with the constraint ($\mathscr{V}$) (more details are provided below); finally, we update ($\mathscr{C}_{\text{E}}$).

This ordering of the core models is defined to reflect the main direction of the interactions among the core models. The interactions that occur in the opposite direction, the so-called feedbacks, are instead evaluated using the solution available from the previous time-step (see, e.g., feedback from mechanics to electrophysiology). To evaluate the feedbacks between ($\mathscr{I}_{\text{IMEX}}$)–($\mathscr{E}_{\text{IMEX}}$) and ($\mathscr{A}_{\text{IMEX}}$)–($\mathscr{M}_{\text{I}}$), we employ the intergrid transfer operator described in Section 4.1. We refer to [31,32,133] for further details.

4.4. Stabilizing the coupling of the core models

The use of segregated schemes can lead to numerical instabilities, especially when feedbacks play a non-negligible role. In the case of cardiac electromechanics, numerical instabilities can arise, on the one hand, due to feedbacks between mechanics and activation [60,128,134–137] and, on the other hand, due to feedbacks between circulation and active–passive mechanics [61,108]. These instabilities, which yield non-physical oscillations, do not affect monolithic methods, which however require higher computational costs than segregated schemes. Furthermore, they force the use of a single time step size for all the core models. With the aim of preserving the advantages of segregated schemes, we use stabilization terms aimed at curing the numerical oscillations. Specifically, we extend the stabilization schemes proposed in [60,61] to the whole heart. Since both schemes act on the ($\mathscr{M}_{\text{I}}$)–($\mathscr{V}$) substep, in what follows we provide more detail on this block.

We update the mechanical displacement variable under the constraint of assigned chamber volumes. The chamber pressures ($p_{\text{RA}}(t)$, $p_{\text{LA}}(t)$, $p_{\text{RV}}(t)$ and $p_{\text{LV}}(t)$) are determined simultaneously with the displacement and play in this context the role of Lagrange multipliers enforcing the volume conservation constraints ($\mathscr{V}$). Introducing the discrete times $t^n = n\Delta t$ (with $n \geq 0$) and denoting by $\boldsymbol{a}_h^n \simeq \boldsymbol{a}_h(t^n)$ the fully discretized FE approximation of the generic (scalar a, vectorial $\boldsymbol{a}$ or tensorial $\mathbf{A}$) variable $\boldsymbol{a}(t)$, we consider the following fully discretized version of the coupled ($\mathscr{M}$)–($\mathscr{V}$) models of Eqs. (6) and (8).

For each time step t^{n+1}, given $T_{\text{a}_h}^{n+1}$ and $\boldsymbol{c}^n$, find $\mathbf{d}_h^{n+1}$, p_{LA}^{n+1}, p_{RA}^{n+1}, p_{LV}^{n+1} and p_{RV}^{n+1} by solving:

$$
\begin{cases}
\displaystyle\int_{\Omega_0} \rho_s \frac{\mathbf{d}_h^{n+1} - 2\mathbf{d}_h^n + \mathbf{d}_h^{n-1}}{\Delta t^2} \cdot \boldsymbol{\varphi}_h \, d\Omega_0 + \int_{\Omega_0} \mathbf{P}(\mathbf{d}_h^{n+1}, T_{\text{a}_h}^{n+1}) : \nabla \boldsymbol{\varphi}_h \, d\Omega_0 + \\
\quad + \displaystyle\int_{\Gamma_0^{\text{epi}}} C_{\perp}^{\text{epi}} \frac{\mathbf{d}_h^{n+1} - \mathbf{d}_h^n}{\Delta t} (\mathbf{N}_h \otimes \mathbf{N}_h) \cdot \boldsymbol{\varphi}_h \, d\Gamma_0 + \int_{\Gamma_0^{\text{epi}}} K_{\perp}^{\text{epi}} (\mathbf{N}_h \otimes \mathbf{N}_h) \mathbf{d}_h^{n+1} \cdot \boldsymbol{\varphi}_h \, d\Gamma_0 + \\
\quad + \displaystyle\sum_{k \in \{\text{RA,LA,RV,LV}\}} p_k^{n+1} \int_{\Gamma_0^{\text{endo},k}} J_h^{n+1} (\mathbf{F}_h^{n+1})^{-T} \mathbf{N}_h \cdot \boldsymbol{\varphi}_h \, d\Gamma_0 + \sum_{k \in \{\text{AO,PT}\}} p_k^n \int_{\Gamma_0^{\text{endo},k}} J_h^{n+1} (\mathbf{F}_h^{n+1})^{-T} \mathbf{N}_h \cdot \boldsymbol{\varphi}_h \, d\Gamma_0 = 0 \\
\qquad\qquad\qquad\qquad\qquad\qquad\qquad\qquad\qquad\qquad\qquad\qquad\qquad\qquad\qquad\qquad \forall \boldsymbol{\varphi}_h \in [\mathcal{X}_{\text{h}}^s]^3, \\
V_{\text{LA}}^{\text{3D}}(\mathbf{d}_h^{n+1}) = V_{\text{LA}}^{\text{0D}}(\boldsymbol{c}^n) \\
V_{\text{LV}}^{\text{3D}}(\mathbf{d}_h^{n+1}) = V_{\text{LV}}^{\text{0D}}(\boldsymbol{c}^n) \\
V_{\text{RA}}^{\text{3D}}(\mathbf{d}_h^{n+1}) = V_{\text{RA}}^{\text{0D}}(\boldsymbol{c}^n) \\
V_{\text{RV}}^{\text{3D}}(\mathbf{d}_h^{n+1}) = V_{\text{RV}}^{\text{0D}}(\boldsymbol{c}^n)
\end{cases}
\tag{21}
$$

with $\mathbf{F}_{\mathrm{h}}^{n+1} = \mathbf{I} + \nabla \mathbf{d}_h^{n+1}$, $J_h^{n+1} = \det(\mathbf{F}_h^{n+1})$ and $\boldsymbol{\varphi}_h$ being a generic test function for the finite dimensional space $[\mathcal{X}_{\mathrm{h}}^s]^3$ with $\mathcal{X}_{\mathrm{h}}^s = \{v \in C^0(\overline{\Omega}_0) : v|_{\mathrm{K}} \in \mathbb{P}_{\mathrm{s}}(K),\ s \geq 1,\ \forall K \in \mathcal{T}_h,\ v = 0 \text{ on } \Gamma_0^{\mathrm{rings}}\}$, where $\mathbb{P}_{\mathrm{s}}(K)$ stands for the set of polynomials with degree smaller than or equal to s over a mesh element K. We also remark that, unlike chamber pressures, arterial pressures (p_{PT}^n and p_{AO}^n) are evaluated at the time step t^n since they are equal to the pulmonary and systemic arterial pressures ($p_{\mathrm{AR}}^{\mathrm{PUL},n}$ and $p_{\mathrm{AR}}^{\mathrm{SYS},n}$, respectively) of the circulation state vector $\boldsymbol{c}^n$.

As mentioned above, the formulation of Eq. (21) typically exhibits numerical oscillations when coupled with an active force model on the one hand, and a circulation model on the other hand.

One source of instability is represented by the fibers-stretch-rate feedback, i.e. the influence that the rate at which fibers shorten has on the amount of force generated at each point in the domain. As shown in [60], these numerical oscillations originate from an inconsistent description of strain, which is represented in Eulerian coordinates at the microscale, i.e. in activation models, in Lagrangian coordinates instead at the macroscale, i.e. in the tissue mechanics model. This can be corrected by introducing an additional term in the formulation, which constitutes a numerically consistent stabilization term. This numerical scheme is obtained by replacing the Piola tensor expression in Eq. (21) with the following expression:

$$\mathbf{P}\left(\mathbf{d}_h^{n+1}, T_{\mathrm{a}h}^{n+1} + K_{\mathrm{a}h}^{n+1}\left(\sqrt{\mathbf{F}_h^{n+1}\mathbf{f}_0 \cdot \mathbf{F}_h^{n+1}\mathbf{f}_0} - \sqrt{\mathbf{F}_h^n\mathbf{f}_0 \cdot \mathbf{F}_h^n\mathbf{f}_0}\right)\right) \tag{22}$$

where K_{a} represents the total stiffness of the attached crossbridges, and is obtained from the activation model (see [60] for more details).

A second source of instability is related to the interaction between active–passive mechanics and circulation. As discussed in [61], the staggered scheme of Eq. (21) is not unconditionally stable, but can exhibit non-physical oscillations for given values of the parameters and Δt. This occurs, for example, for sufficiently large values of inertia, viscous dissipation and stiffness, or again as a consequence of fibers-stretch-rate feedback, which leads to an increase in apparent stiffness. In order to cure these oscillations without resorting to a monolithic scheme, we take inspiration from [61] and we correct the volume constraint in Eq. (21), namely $V_k^{\mathrm{3D}}(\mathbf{d}_h^{n+1}) = V_k^{\mathrm{0D}}(\boldsymbol{c}^n)$ for $k \in \{\mathrm{RA}, \mathrm{LA}, \mathrm{RV}, \mathrm{LV}\}$. In particular, the volumes derived from the circulation model at time t_n are replaced by their extrapolation at time t_{n+1}, which takes into account the effect that the variation of the pressures in the four chambers will have on the fluxes through the valves. More precisely, the volume constraints of the stabilized scheme read:

$$\begin{cases} V_{\mathrm{LA}}^{\mathrm{3D}}(\mathbf{d}_h^{n+1}) = V_{\mathrm{LA}}^{\mathrm{0D}}(\boldsymbol{c}^n) + \Delta t\left[Q_{\mathrm{VEN}}^{\mathrm{PUL,n}} - Q_{\mathrm{MV}}(p_{\mathrm{LA}}^{n+1}, p_{\mathrm{LV}}^{n+1})\right] \\ V_{\mathrm{LV}}^{\mathrm{3D}}(\mathbf{d}_h^{n+1}) = V_{\mathrm{LV}}^{\mathrm{0D}}(\boldsymbol{c}^n) + \Delta t\left[Q_{\mathrm{MV}}(p_{\mathrm{LA}}^{n+1}, p_{\mathrm{LV}}^{n+1}) - Q_{\mathrm{AV}}(p_{\mathrm{LV}}^{n+1}, p_{\mathrm{AR}}^{\mathrm{SYS,n}})\right] \\ V_{\mathrm{RA}}^{\mathrm{3D}}(\mathbf{d}_h^{n+1}) = V_{\mathrm{RA}}^{\mathrm{0D}}(\boldsymbol{c}^n) + \Delta t\left[Q_{\mathrm{VEN}}^{\mathrm{SYS,n}} - Q_{\mathrm{TV}}(p_{\mathrm{RA}}^{n+1}, p_{\mathrm{RV}}^{n+1})\right] \\ V_{\mathrm{RV}}^{\mathrm{3D}}(\mathbf{d}_h^{n+1}) = V_{\mathrm{RV}}^{\mathrm{0D}}(\boldsymbol{c}^n) + \Delta t\left[Q_{\mathrm{TV}}(p_{\mathrm{RA}}^{n+1}, p_{\mathrm{RV}}^{n+1}) - Q_{\mathrm{PV}}(p_{\mathrm{RV}}^{n+1}, p_{\mathrm{AR}}^{\mathrm{PUL,n}})\right] \end{cases} \tag{23}$$

We remark that in Eq. (23), while the pressures in the four chambers are evaluated at time t_{n+1}, the state variables of the circulation model are evaluated at time t_n. In other words, Eq. (23) does not invalidate the staggered nature of the scheme. Nevertheless, the additional terms allow for the removal of numerical oscillations. Indeed, it is shown in [61] that this scheme is absolutely stable for any choice of parameters and Δt. We remark that, while in the test cases presented in [61] stabilization terms were present on the diagonal on the Jacobian matrix only, in this work extra-diagonal terms are present as well. This is due to the presence of communicating chambers, since changes in pressure in a given chamber might affect the dynamics of other chambers. For example, the flux correction of the LV involves the pressure of the LA, thus leading to an extra-diagonal stabilization term. Our numerical tests have shown that, by neglecting extra-diagonal terms, stabilization is not effective, and nonphysical oscillations are likely to appear. The introduction of these terms is thus crucial for an effective application of the technique of [61] in a four-chamber setting.

The introduced stabilization terms are straightforward to implement and have negligible impact on the computational cost. Indeed, the fully discretized version of the stabilized version of system (21) can be compactly

written as:

$$\begin{cases} \mathbf{r_d}(\mathbf{d}_h^{n+1}, p_{\mathrm{LA}}^{n+1}, p_{\mathrm{LV}}^{n+1}, p_{\mathrm{RA}}^{n+1}, p_{\mathrm{RV}}^{n+1}) & = \mathbf{0}, \\ r_{p_{\mathrm{LA}}}(\mathbf{d}_h^{n+1}, p_{\mathrm{LA}}^{n+1}, p_{\mathrm{LV}}^{n+1}) & = 0, \\ r_{p_{\mathrm{LV}}}(\mathbf{d}_h^{n+1}, p_{\mathrm{LA}}^{n+1}, p_{\mathrm{LV}}^{n+1}) & = 0, \\ r_{p_{\mathrm{RA}}}(\mathbf{d}_h^{n+1}, p_{\mathrm{RA}}^{n+1}, p_{\mathrm{RV}}^{n+1}) & = 0, \\ r_{p_{\mathrm{RV}}}(\mathbf{d}_h^{n+1}, p_{\mathrm{RA}}^{n+1}, p_{\mathrm{RV}}^{n+1}) & = 0, \end{cases} \tag{24}$$

where we moved all the terms to the left hand side and $r_{p_{\mathrm{RA}}}$, $r_{p_{\mathrm{LA}}}$, $r_{p_{\mathrm{RV}}}$, $r_{p_{\mathrm{LV}}}$ and $\mathbf{r_d}$ are suitable functions. Eq. is a nonlinear saddle-point problem, that we solve by means of the Newton algorithm using the Schur complement reduction [31,32,138]. As shown in [61], this can be done at the cost of 5 solutions of the linear system (that is, the number or chambers plus one) associated with the Jacobian matrix of the standalone mechanical subproblem for each Newton iteration.

5. Numerical simulations and discussion

In this section we display and discuss the results obtained using our whole-heart electromechanical model. More specifically, in Section 5.1 we summarize the common settings for all the numerical simulations. In Section 5.2 we show the results of a baseline simulation. Eventually, in Sections 5.3 and 5.4, we show the impact of some features of our computational model, as the atrial contraction, the fibers-stretch-rate feedback and the numerical stabilization terms.

5.1. Simulation setup

We generate the computational mesh starting from the Zygote Solid 3D Heart Model [56], an anatomically accurate CAD model of the entire human heart reconstructed from high-resolution CT scans and representing a healthy male subject from the 50th percentile of the United States population. The original model – made of disjoint parts of the various cardiac compartments – has been processed to fit the domain features described in Section 3.1. With this purpose, we rely on the algorithms recently proposed by Fedele and Quarteroni [139] to facilitate the surface processing and mesh generation of cardiac geometries, implemented in the open source software `vmtk`[2] [140]. In particular, we extensively use the `surface-connection`, `boolean-connection`, `surface-tagger`, and `mesh-connector` algorithms [139]. The final tetrahedral computational mesh is shown in Fig. 9, (a). This mesh is characterized by a mesh size of about 1.5 mm in the myocardium – i.e. in the conductive regions where also the electrophysiology and the active force generation model are solved – and of about 3 mm in the non-conductive regions — where only the mechanical model is solved with a less demanding isotropic Neo-Hookean constitutive law. Starting from this mesh – that represents the domain in the imaging configuration $\widetilde{\Omega}$ – we recover the reference configuration Ω_0 by solving the problem illustrated in Section 3.4. The resulting deformed mesh is then remeshed to improve the quality of the elements that can be adversely affected by the deformation procedure, especially in the anatomically complex and thin regions of the atria.

The aforementioned mesh is used only for the baseline simulation (Section 5.2), while for the tests described in Sections 5.3 and 5.4, in order to reduce the computational burden of the numerical simulations, we take advantage of a coarser mesh characterized by a mesh-size of about 3 mm also in the conductive regions. Indeed, those tests aim at describing the qualitative effects of some changes in the models and the quantities analyzed are not significantly affected by the coarsening of the mesh. The fine and coarse meshes are made up of 1.34M and 270K elements and 229K and 51K vertexes, respectively. The corresponding number of DOFs relative to the electrical ($\mathscr{E}_{\mathrm{IMEX}}$) and mechanical ($\mathscr{M}_{\mathrm{I}}$) FE problems are 1.71M and 687K, respectively, for the fine mesh, and 337K and 154K, respectively, for the coarse mesh.

Concerning the time steps, we use $\tau = 50$ μs for the electrophysiology and $\Delta t = 1000$ μs for the mechanical, activation and circulation problems [32,83]. All the other parameters of the baseline simulation (Section 5.2) are listed in Appendix A. We simulate 9 and 6 heartbeats for the baseline simulation and the other tests, respectively, showing the results of the last two heartbeats, when the circulation variables reach their limit cycle.

[2] https://github.com/marco-fedele/vmtk

In all the presented simulations the cardiac electrical conduction system (see Fig. 1, (c)) is modeled using the same series of spherical impulses, as detailed in Fig. 9, (b). We first stimulate the atrial muscles at the SAN allowing the propagation of the signal in the RA and, through the BB and the atrial septum, toward the LA. Then, waiting for the physiological delay, we stimulate with a series of impulses the ventricular endocardium on five different points. As done by Piersanti et al. [51], this delay is a-priori calibrated considering the time that the electric signal needs to reach these points in a physiological scenario. In particular, we first stimulate the LV and soon after the RV, in order to model the physiological lag of the RBB with respect to the LBB. These series of impulses on the ventricular endocardium together with the fast endocardial layer surrogates the effect of the PFs. Finally, to achieve physiological activation times for both the ventricles and the atria, the monodomain conductivity values were estimated (using a tuning procedure described in [51]) to roughly match the following conduction velocities: for the ventricular myocardium, 0.7, 0.4 and 0.2 $\mathrm{m\,s^{-1}}$ in the fiber, sheet and sheet-normal directions, respectively [26]; for the atrial muscle, 1.2 and 0.5 $\mathrm{m\,s^{-1}}$ in the fiber and along the sheet and sheet-normal directions, respectively [141]. The whole stimulation protocol is periodically repeated every heartbeat, representing a simplified but effective model of the pacemaking activity of the SAN and of the entire electrical conduction system.

We initialize the ionic models by running a 1000-cycle long single-cell simulation for each model. Similarly, we run single-cell simulations for the force generation models with a constant calcium input ($w_{\mathrm{Ca}} = 0.1$ μmol) and a reference sarcomere length $\mathrm{SL} = 2.2$ μm [32].

The numerical framework presented in Section 4 has been implemented in `life`$^{\mathtt{x}}$ [66], an in-house high-performance `C++` FE library for cardiac applications, based on the `deal.II`[3] FE core [142]. The core of `life`$^{\mathtt{x}}$ is publicly available under an open-source license [66,67], whereas a public binary release of `life`$^{\mathtt{x}}$ including the fiber generation package is freely available online as a free binary package[4] [143]. All the numerical simulations were performed using either the `iHeart` cluster (Lenovo SR950 192-Core Intel Xeon Platinum 8160, 2100 MHz and 1.7TB RAM) at MOX, Dipartimento di Matematica, Politecnico di Milano or the `GALILEO100` supercomputer at Cineca (24 nodes endowed with 48-Core Intel CascadeLake 8260, 2.4 GHz, 384 GB RAM). A simulation of one heartbeat lasts for the fine mesh about 2.8 h with 1152 cores on the `GALILEO100` supercomputer, for the coarse mesh about 4.2 h with 48 cores of the `iHeart` cluster. The computational cost of the baseline simulation with the fine mesh is almost equally distributed between electrophysiology ($\mathscr{E}$)–($\mathscr{I}$) and mechanics ($\mathscr{M}$), with negligible computational costs for all the other core models. Indeed, both of these models are computationally demanding for several reasons, such as the high nonlinearity of the mechanical model – which affects both the assembly and solving time – and the use of quadratic FEs and a smaller timestep for the electrophysiological model. In the future – especially in a physiological scenario – we plan to reduce the cost of the electrophysiology by exploring the use of eikonal-based models, for example by extending the eikonal-diffusion model presented by Stella et al. [33] to the whole heart.

5.2. The baseline simulation

In Fig. 10 we show the temporal variation of some state variables during the last two heartbeats of the baseline simulation. The obtained curves of pressures, volumes and fluxes qualitatively correspond to those expected for a physiological heart function [72,144].

Concerning the systolic function, we obtain an excellent agreement with reference values for a healthy adult available in the literature. Indeed, the maximum fluxes obtained through the semilunar valves (Q_{PV}, Q_{AV}) during the VE phase (about $600\,\mathrm{mL\,s^{-1}}$) are in the physiological range usually measured by PC-MRI data (500–600 $\mathrm{mL\,s^{-1}}$) [145–147]. This feature is hardly achieved by computational models which tend to largely overestimate these fluxes, even when they reproduce the physiological ventricular output in terms of SV (see, e.g., [52, Fig. 10]). As we will show in Section 5.3, a key component of our model to achieve this result is the fibers-stretch-rate feedback accounted for by the RDQ20 model, that homogenizes the fibers shortening velocity and contributes to regulate the blood fluxes.

Concerning the diastolic function, instead, the *atrial kick* is clearly visible during the AC phase, for both ventricular and atrial volumes (V_{RA}, V_{RV}, V_{LA}, V_{LV}), atrial pressures (p_{RA}, p_{LA}), and fluxes through the atrioventricular

[3] https://www.dealii.org
[4] https://doi.org/10.5281/zenodo.5810269

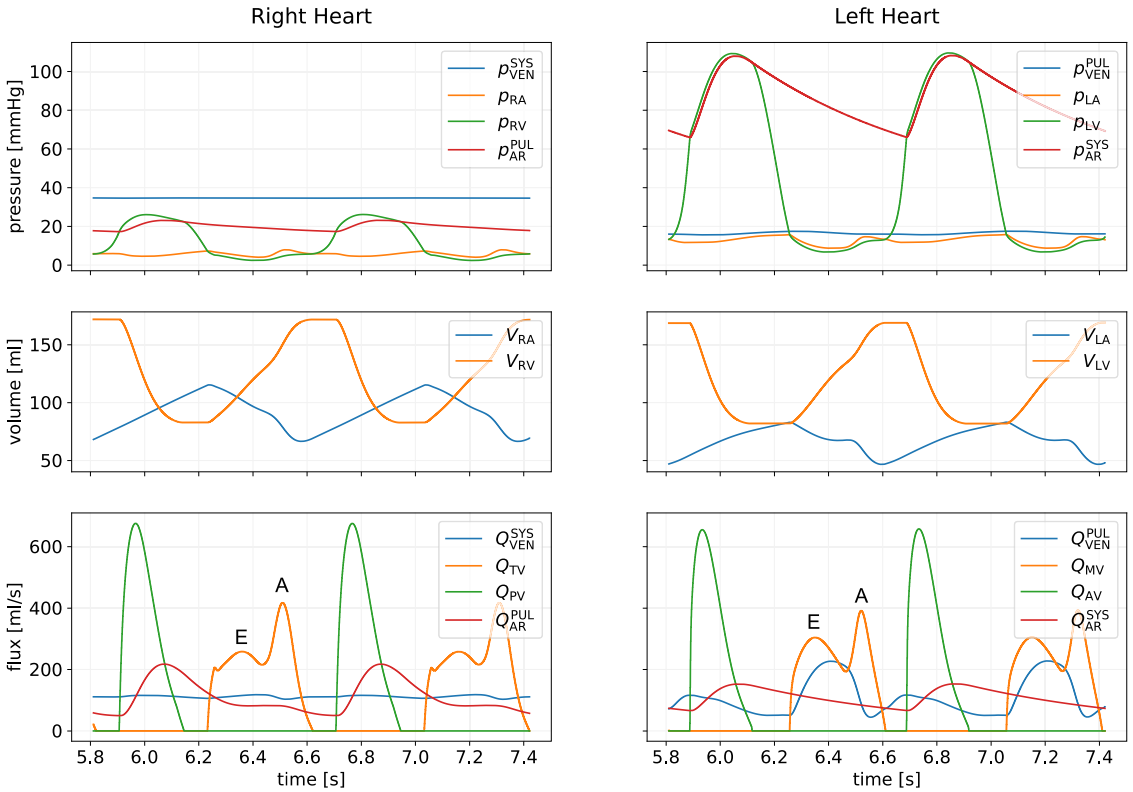

Fig. 10. Pressure, volumes, and fluxes evolution over time during the last two heartbeats of the state variables of the coupled mechanics-circulation model for the baseline simulation. For the MV and TV fluxes we also highlight the E-wave and the A-wave.

valves (Q_{TV}, Q_{MV}). However, the fluxes during a healthy diastolic function should be characterized by an E-wave – corresponding to the VPF phase – which is taller than the A-wave — corresponding to the AC phase [148,149]. In other words, the ventricular filling should be mainly determined by the ventricular relaxation than by the atrial contraction. The different behavior that we obtain (see Fig. 10, last row) can be motivated by a too slow ventricular relaxation during the VPF phase [148,149]. We expect that a better agreement with literature data can be obtained by resorting to ionic models with a more realistic decrease transient of calcium concentration [64,93].

An additional limitation regards the venous flows. Indeed, these blood flows are mainly determined by the RLC elements of the 0D blood circulation model, which is a very simplified model of the circulatory system conceived to connect the blood flows of the right and left parts of the heart, thus allowing to obtain consistent flows between the two sides of the circulation. As a consequence, the blood fluxes described by the variables $Q_{\text{VEN}}^{\text{SYS}}(t)$ and $Q_{\text{VEN}}^{\text{PUL}}(t)$ (see Fig. 10, last row) can be considered as a sort of averaged venous flows in the whole systemic and pulmonary venous circulation. Thus, these variables are not able to reproduce some physiological values measured in-vivo in specific venous districts, such as the vanishing of the pulmonary venous flow during atrial contraction at the onset of the LA (see, e.g. [150,151]).

In Fig. 11 we show the pressure–volume loops of the four cardiac chambers, while in Fig. 12 we display the same curves together with the evolution over time of the pressures and volumes. In both figures we color each curve with the five phases of the cardiac cycle described in Sections 2 and 2 and we also represent the opening and closing moments of the four cardiac valves. As depicted in Fig. 11, (a), the pressure and volume ranges vary significantly among the four cardiac chambers, as reported, e.g., by Verzicco [22, Fig. 10]. The shape of the pressure–volume loops finds a very good agreement with the medical literature [22,71,78,79,151]. While this is not the first time that an electromechanical model is able to describe the ventricular physiology [31,32,52], to the best of our knowledge the eight-shaped pressure–volume loops of the atria have never been shown so accurately by a computational model.

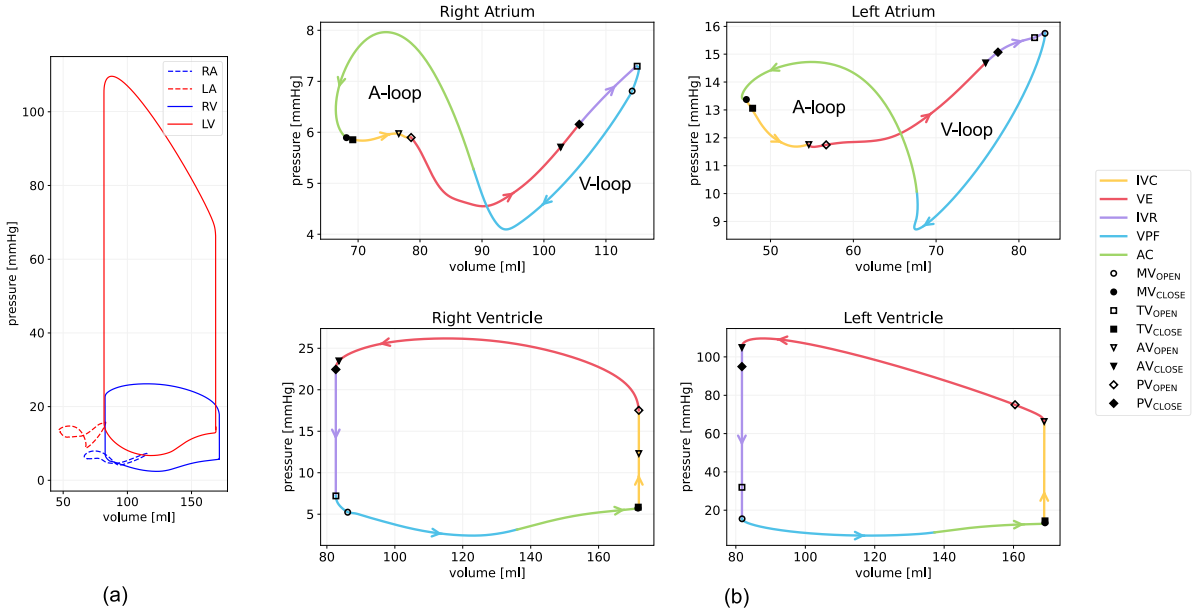

Fig. 11. The pressure–volume loops of the last heartbeat for the baseline simulation: (a) all the curves in a single figure to highlight the difference in volumes and pressures among the cardiac chambers; (b) the curves colored with the phases of the cardiac cycle and highlighting the opening and closing time of each cardiac valve. Abbreviations are defined in Table 1.

Indeed, we obtain, as expected by the literature [78,151], A- and V-loops that are similar in size. On the contrary, A-loops significantly (and abnormally) larger than V-loops are obtained by the few other whole-heart electromechanical models accounting for atrial contraction [48,52].

The atrial function of reservoir, conduit, and booster pump is also well captured: the total emptying volume ($V_{\max} - V_{\min}$, reservoir) is divided between the passive emptying volume ($V_{\max} - V_{\text{preAC}}$, conduit) and the active emptying volume ($V_{\text{preAC}} - V_{\min}$, booster pump), with these last two volumes comparable in size [78,152,153]. The contribution of the atrial booster pump function to the ventricular filling falls within the physiological upper limit. More quantitatively, the LA contraction contributes to the 33% of the LV filling, while normal healthy values are reported in the range 15%–30% [78,151,154].

The evolution over time of the atrial volume is very well captured. In particular, the LA curve (see Fig. 12, second row, last plot) matches similar curves reconstructed from medical images (see, e.g., Thomas et al. [154, Fig. 7] and Badano et al. [155, Fig. 3]): the volume smoothly increases when the MV is closed (IVC, VE and IVR phases); a sharp decrease followed by a stationary moment occurs during the VPF phase; an additional sharp decrease coincides with the AC phase, corresponding to the booster pump function.

The atrial pressure evolution over time is characterized by three waves and two pressure descents [72,151,156]: the a-wave — corresponding to the increase of pressure due to the atrial contraction; the c-wave — caused by the closure of the atrioventricular valves (TV, MV) that push the blood back toward the atria; the x-descent — determined by the initial phase of the ventricular contraction and the consequent downward movement and filling of the atria; the v-wave — caused by the continuous venous return while the atrioventricular valves are closed, during the ventricular systole; the y-descent — which begins with the opening of the atrioventricular valves and continues during the VPF phase. In Fig. 12, first two rows, central column, all these complex features are captured. Additionally, we also obtain an a-wave taller than the v-wave in the RA [156] and the opposite behavior in the LA [151,157], as described in the medical literature [72,151,156–158]. This behavior is also visible in the atrial pressure–volume loops (Fig. 11, (b), top), where the pressure assumes its maximum value during the A-loop for the RA and during the V-loop for the LA.

Another captured physiological behavior concerns the opening and closing times of the cardiac valves. Indeed, looking at the pressure and volume evolution over time (Fig. 12), we observe how the right valves (TV, PV) close

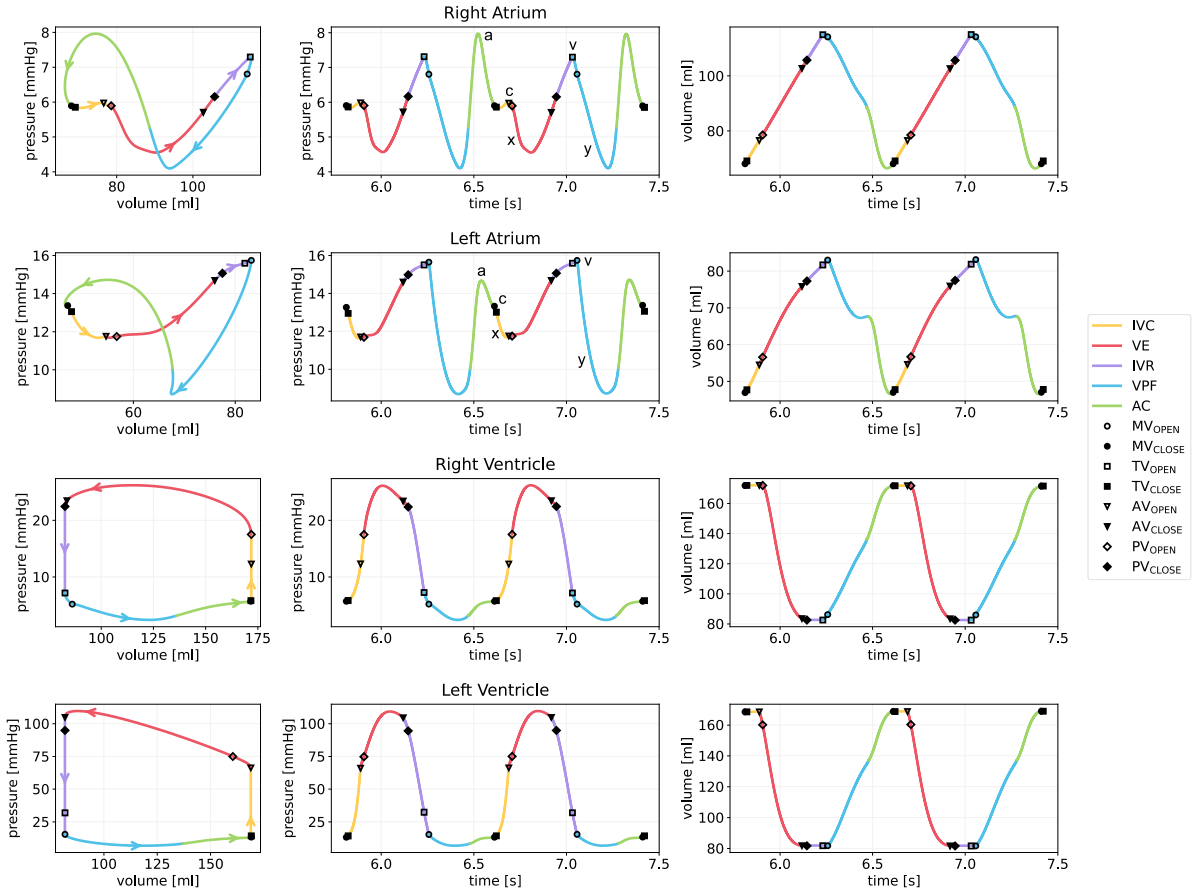

Fig. 12. The phases of the cardiac cycle for the four heart chambers both in terms of pressure–volume loop (last heartbeat) and in terms of pressure and volume evolution over time (last two heartbeats). The opening and closing time of each cardiac valve is also reported. For the atrial pressure evolution we also highlight the a–c–v waves and the x–y descents. Abbreviations are defined in Table 1.

after the left ones (MV, AV). More specifically, the closing of the atrioventricular valves (TV, MV) is almost synchronized, while a longer delay between the closing of the semilunar valves (PV, AV) occurs. This behavior corresponds to normal cardiac physiology and can be routinely verified by checking the first and second heart sounds through cardiac auscultation [159]. We obtain these results thanks to our stimulation protocol that, albeit simplified, correctly reproduces the activation delay between LV and RV. On the other hand, probably due to the oversimplified surrogated cardiac conduction system, the positions of the opening and closing times of some valves within the cardiac cycle could be further improved. For example, AV closure occurs too soon after peak systolic pressure.

In Fig. 13 we show the three-dimensional motion of the heart during a heartbeat. The cardiac muscle is colored according to the local value of the active tension T_a, to highlight which chambers are contracting and which are relaxing during the five phases of the cardiac cycle. Specifically, we show the cardiac geometry deformed by the displacement $\mathbf{d}$ at the initial and final moments of each phase. In the corresponding Video S1 (online version) we show also the evolution of the transmembrane potential u and of the intracellular calcium concentration w_{Ca}. Our simulation reproduces the expected motion of a healthy heart, as summarized below.

- The IVR starts with relaxed atria and contracted ventricle. During this short phase the ventricular active forces quickly drop down together with the pressure. Since both the atrioventricular valves (TV and MV) and the semilunar valves (PV and AV) are closed, the ventricular volumes are constant and no significant motion occurs during this phase.

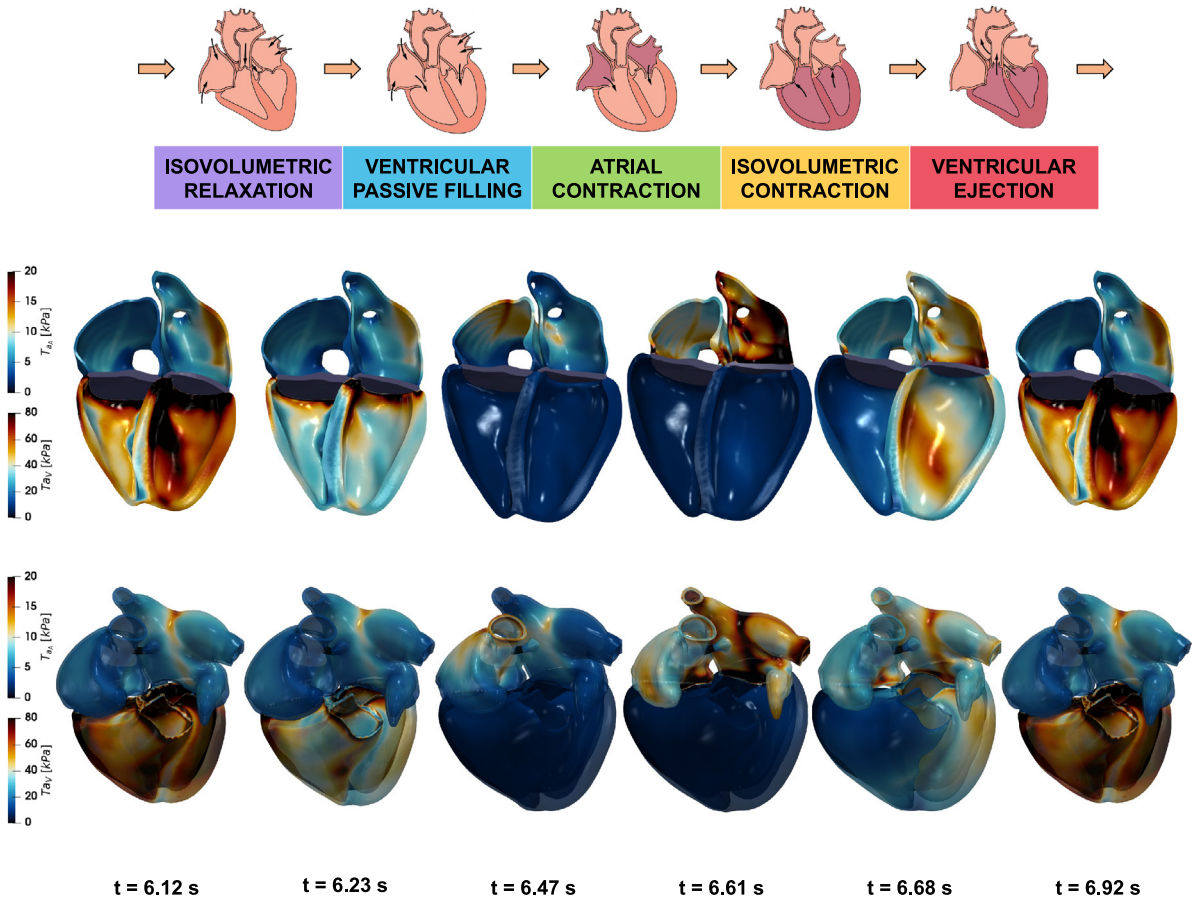

Fig. 13. Deformed configuration of the cardiac muscle over time, colored with the active tension T_a saturated to 20 kPa and 80 kPa for the atria and ventricles, respectively: the internal view (top) and the external view (bottom) at the initial and final instants of each phase of the cardiac cycle. The corresponding Video S1 (online version) shows also the evolution in time of the transmembrane potential u and of the intracellular calcium concentration w_{Ca}.

- The VPF starts when the TV and MV open and is characterized not only by the active tension that continues to fall, but also by a clear increase of the ventricular volumes and a corresponding decrease of the atrial ones. These volumetric changes are mainly caused by the upward movement of the ventricular base, which compresses the atria and dilates the ventricles. During this phase the atrial are passively deformed, acting as a conduit.
- In late diastole, the AC phase starts from the pacemaking stimulation in the RA (near the SupVC) and propagates toward the LA. The atrial booster pump function gives an additional preload to the ventricles, visible once again with a clear upward movement of the base. We recall that the active tension is influenced by the local fiber stretch. Indeed, being the atrial deformation mainly longitudinal, active tension is higher where the fibers are not oriented transmurally. Thanks to our anatomically accurate fiber model, this feature is clearly visible in the PeMs (see Video S1), where the active tension follows their characteristic orientation.
- The ventricular contraction starts during the short IVC phase, when the atrioventricular valves close again and the ventricular active tension starts to rise from the left to the right part. Since also during this phase the ventricular volumes are constant, no clear deformation are visible. Meanwhile, the atria begin to fill up, starting their reservoir function fueled by the continuous venous return.
- Finally, the VE phase is characterized by the opening of the semilunar valves (PV and AV), the strong ventricular contraction, and the consequent decrease of the ventricular volumes. Again, the key factor driving

this emptying phase is the downward movement of the atrioventricular plane [160], which also determines most of the atrial filling during its reservoir function.

The just described physiological motion of the entire heart during the whole cardiac cycle has been obtained thanks to several features of our electromechanical model. According to our experience, the key factors are the following: (i) the anatomical accuracy of the geometry; (ii) the use of comprehensive and calibrated mathematical models for the atria and the ventricles, in terms of electrophysiology, active-force generation, passive mechanics; (iv) the modeling of the most relevant feedbacks among the different core models, with particular reference to the fibers-stretch and fibers-stretch-rate feedbacks in the force generation model; (v) the mechanical boundary conditions on the epicardium taking into account both the presence of the PF and of the EAT. The latter, in particular, is of fundamental importance for the correct downward and upward movement of the ventricular base.

5.3. The impact of the atrial contraction and of the fibers-stretch-rate feedback

In this section we aim at showing the critical role that atrial contraction and fibers-stretch-rate feedback play in simulating the physiological cardiac function. We do not consider the MEF, as it mostly plays a role in pathological conditions involving arrhythmogenic behavior [12,161].

Most of the whole-heart electromechanical models, as discussed in Section 1, neglect the atrial contraction [21, 26,45,46,49,50]. To discuss the impact of this choice, in Fig. 14 we show the effect of switching off the atrial contraction in the model. This is simulated by considering the atria as purely passive tissues, by ignoring in the atrial domain $\{\Omega_0^{\mathrm{RA}} \cup \Omega_0^{\mathrm{LA}}\}$ the active stress part of the Piola–Kirchhoff stress tensor (see Eq. (15)a). The results show irrefutably the importance of atrial contraction for both atrial and ventricular function: on the one hand the A-loop disappears from the atrial pressure–volume loops; on the other hand, the ventricular cycle also changes drastically with a significant decrease in ventricular preload. This non-physiological behavior is also evident in the evolution of the state variables (Fig. 14, bottom), where the contributions of the atrial contraction in terms of pressures, volumes and fluxes disappear. In other words, neglecting atrial contraction means neglecting the booster pump function of the atria and its preloading effect on the ventricles, modeling a pathological scenario rather than a healthy one. For instance, as shown by Pagel et al. [151], similar pressure–volume loops are captured during atrial fibrillation, when the chaotic propagation of the electrical signal causes the atrium to lose its booster pump function.

In Fig. 15 we show the effects on the results of the fibers-stretch-rate feedback off in the model. In terms of pressure–volume loops (Fig. 15, top) no substantial changes are visible, with a small increase of the A-loop size in the atria and a small increase of the ventricular pressures during the VE phase. Conversely, looking at the state variables (Fig. 15, bottom), the fluxes through the semilunar valves (AV and PV) dramatically change. More specifically, without the fibers-stretch-rate feedback we obtain about $1200\,\mathrm{mL\,s^{-1}}$ in the AV and almost $1500\,\mathrm{mL\,s^{-1}}$ in the PV. This abnormal values are similar to the ones reported by the whole-heart model of Gerach et al. [52], that indeed neglects the fibers-stretch-rate feedback since, without suitable stabilization terms, it yields strong non-physical oscillations in the multi-scale model resulting in an unstable numerical scheme [52]. A large increase of the fluxes appears also in the atrioventricular valves during the AC phase.

We conclude that the fibers-stretch-rate plays a fundamental role in the regulation of the cardiac function. As a consequence of this feedback, indeed, the active force decreases for the cardiac cells located in regions where fibers are rapidly shortening, thus resulting in slowing down the contraction velocity of fibers. As this feedback acts locally (i.e. at the cell level), the resulting macroscopic effect is a homogenization of fibers shortening velocity, preventing sharp variations. From a hemodynamic perspective, this results into a smoothing of the ejected blood flux, as highlighted by our results. Hence, we postulate that the fibers-stretch-rate feedback, despite originating from the microscale force-velocity relationship of sarcomeres, plays a crucial role in the regulation of blood fluxes.

5.4. The need of the numerical stabilization

To highlight the role of the stabilization terms described in Section 4.4, we present the results of two numerical simulations obtained by switching off the stabilization terms on active stress (see Eq. (22) and [60]) and on the 3D-0D mechanics-circulation coupling (see Eq. (23) and [61]), respectively.

In Fig. 16 we show results obtained without the active stress stabilization. As soon as active tension is being developed, non-physical oscillations occur, mainly in pressure and flux traces, finally leading to failure of the

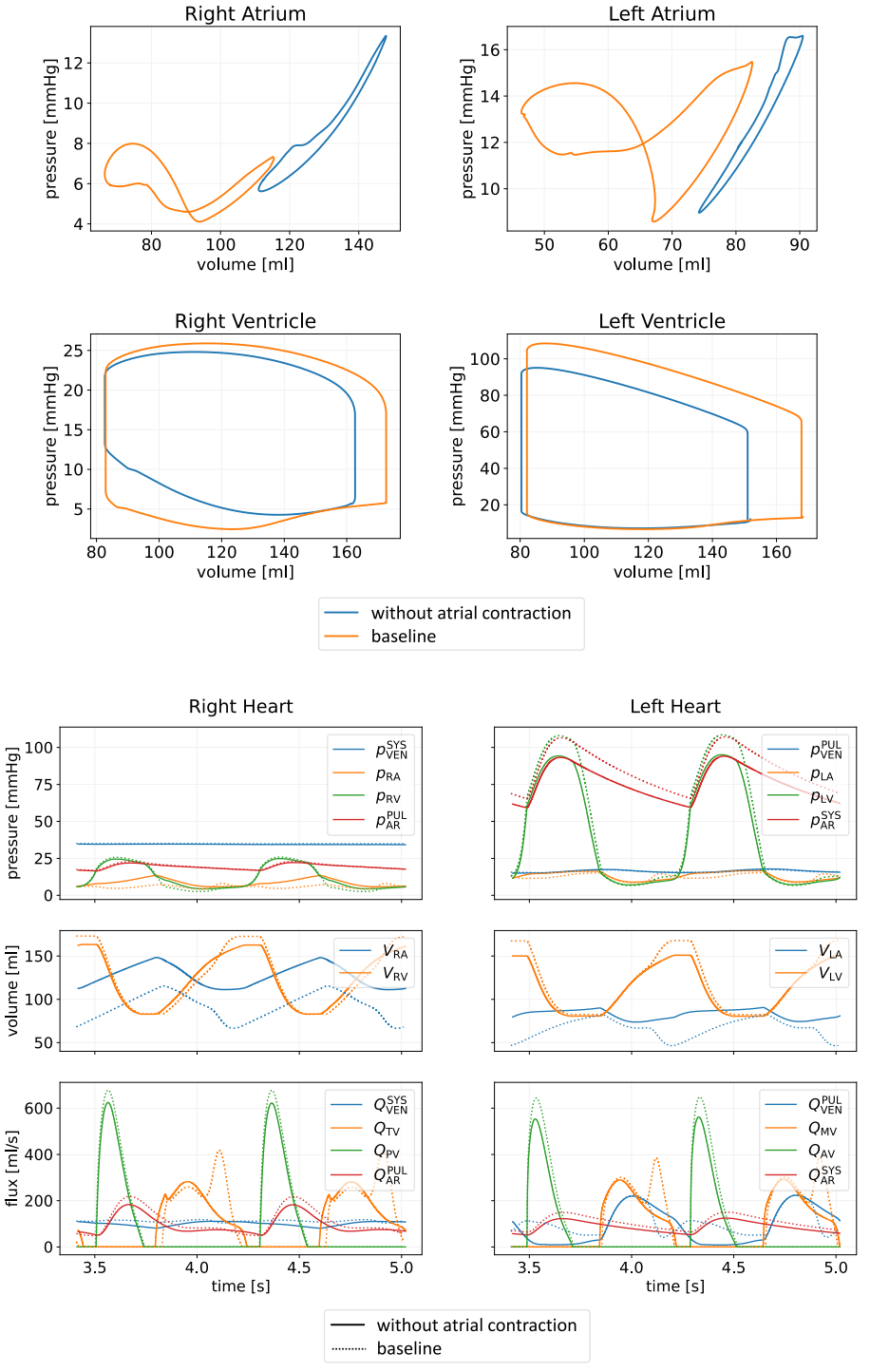

Fig. 14. Pressure–volume loops (top) and circulation state variables (bottom) with and without the atrial contraction in the model.

nonlinear mechanics solver. In the simulation shown in the figure, failure occurs after nearly 0.35 s of physical time. While the time of failure depends on the time step size and on the parameters, in our experience the numerical simulation of cardiac active mechanics with realistic parameter values always leads to this kind of numerical

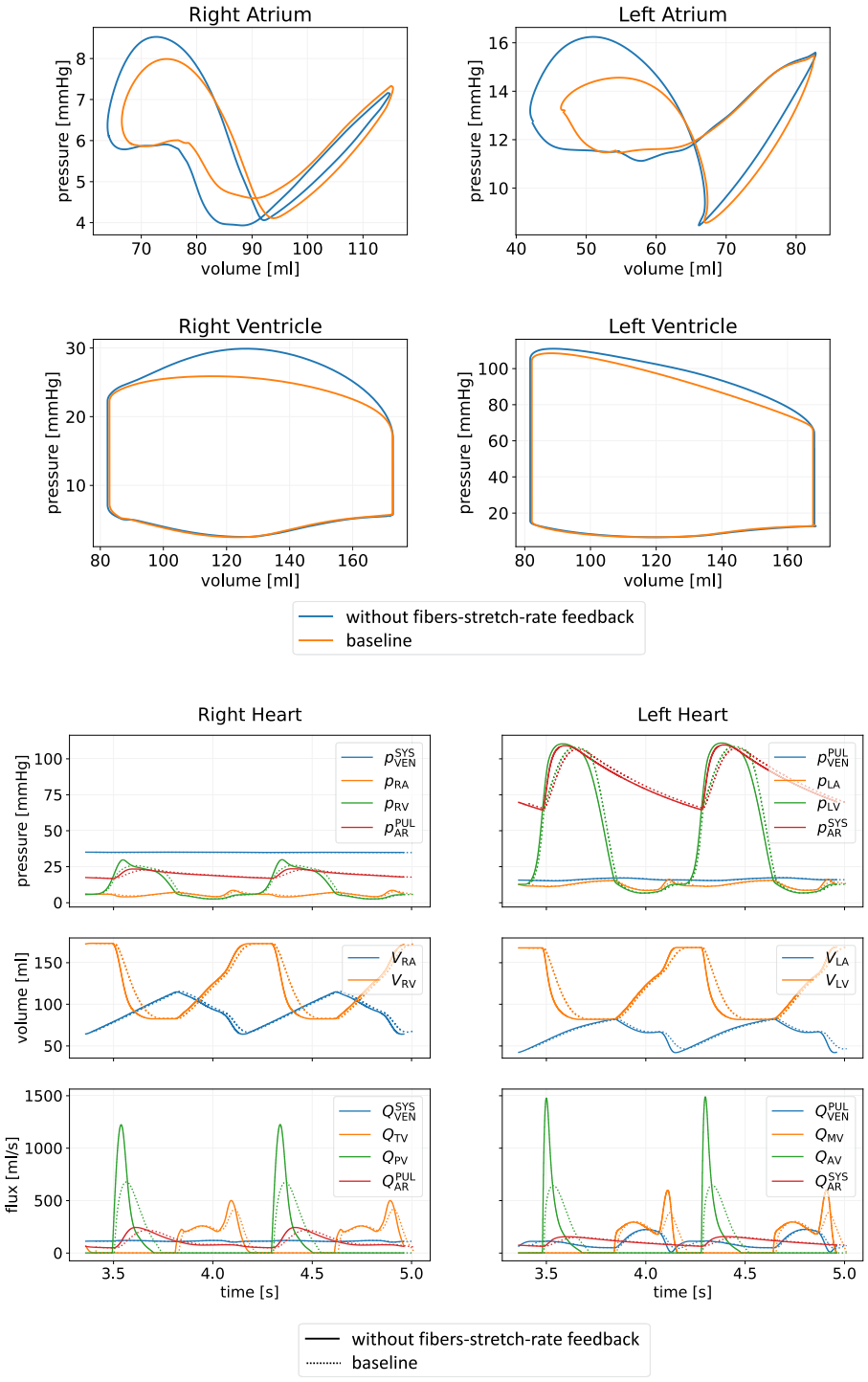

Fig. 15. Pressure–volume loops (top) and circulation state variables (bottom) with and without the fibers-stretch-rate feedback in the model.

oscillations, whenever stretch-rate-feedback is accounted for by the model. These instabilities cannot be cured by reducing the time step size: on the contrary, as analytically demonstrated [60], they are amplified by a rapid exchange of variables between the tissue mechanics and the activation model.

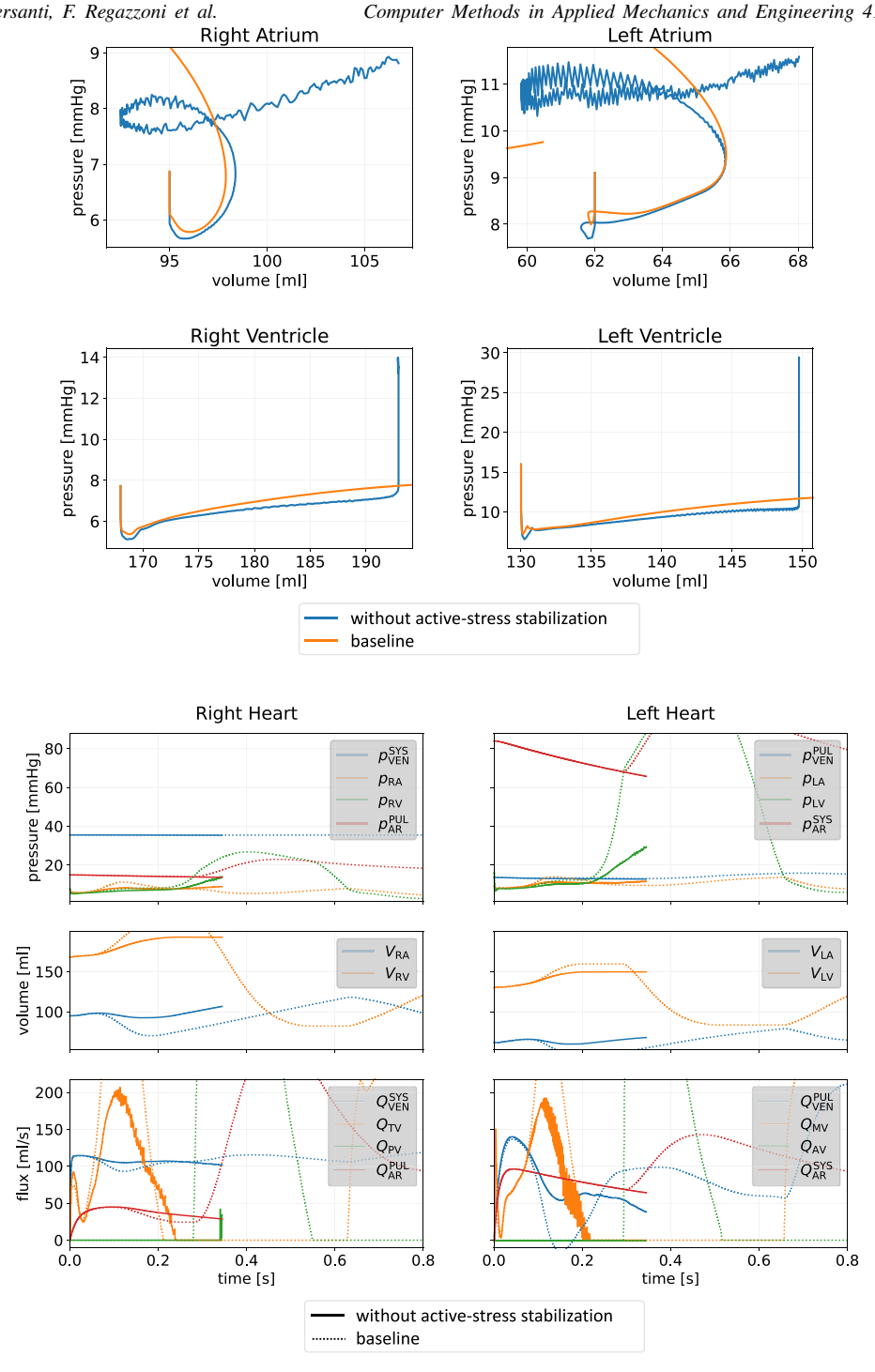

Fig. 16. Pressure–volume loops (top) and circulation state variables (bottom) with and without the stabilization terms in the active stress model.

In Fig. 17 we report the results obtained by switching off the stabilization term on the 3D-0D mechanics-circulation coupling. Unlike for the active stress stabilization term, the numerical oscillations obtained in this case do not lead to failure of the simulation. However, the results are clearly not physically meaningful. This is particularly evident from the transients of blood fluxes across valves, that exhibit very large oscillations. As demonstrated in [61],

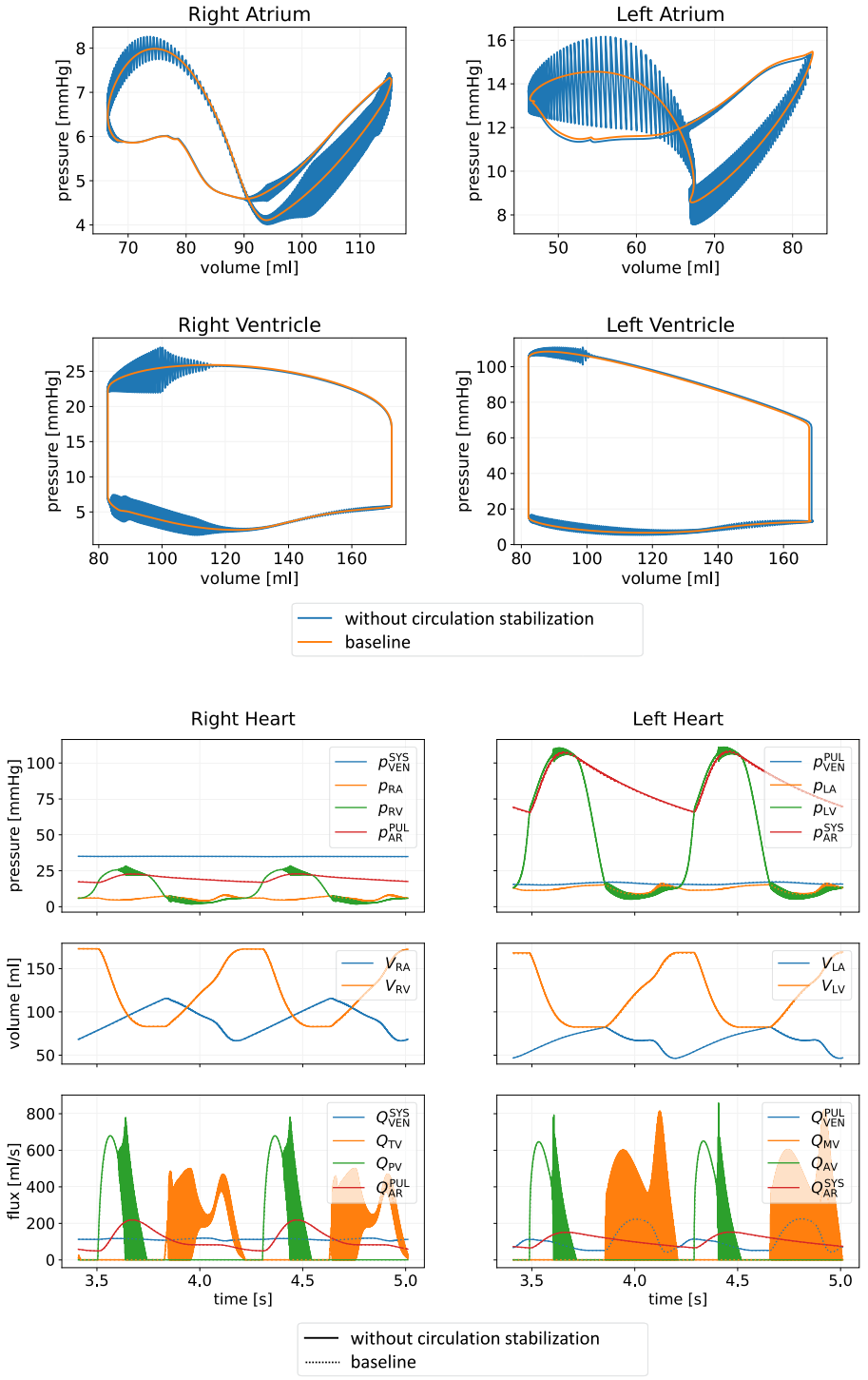

Fig. 17. Pressure–volume loops (top) and circulation state variables (bottom) with and without the stabilization terms in the circulation model.

Table 2
Volumetric indexes of the four cardiac chambers: the values computed from the baseline simulation compared to the reference ranges for cardiac magnetic resonance [153,162] (*SD* standard deviation, *LL* lower limit, *UL* upper limit). All the volumes are indexed by the body surface area. Reference ranges are taken from the recent meta-analysis by Kawel-Boehm et al. [162], with the exception of the values marked with * taken from Li et al. [153], the only paper included in the meta-analysis in which additional parameters for atrial conduit and booster pump function are analyzed.

Index	Value	Reference range		Description
		mean ± SD	[LL, UL]	
RA V_{max} [mL/m^2]	43.7	52 ± 12	[28, 76]	RA maximum volume
RA V_{preAC} [mL/m^2]	32.8	$40 \pm 10^*$	[19, 61]*	RA volume before atrial contraction
RA V_{min} [mL/m^2]	25.2	27 ± 9	[9, 45]	RA minimum volume
RA PassEF [%]	24.8	$23 \pm 9^*$	[4, 41]*	RA passive ejection fraction: $(V_{max} - V_{preAC})/V_{max}$
RA ActEF [%]	23.4	$33 \pm 10^*$	[11, 55]*	RA active ejection fraction: $(V_{preAC} - V_{min})/V_{preAC}$
RA TotEF [%]	42.4	49 ± 10	[29, 68]	RA total ejection fraction: $(V_{max} - V_{min})/V_{max}$
LA V_{max} [mL/m^2]	30.6	41 ± 8	[24, 57]	LA maximum volume
LA V_{preAC} [mL/m^2]	24.7	$30 \pm 8^*$	[15, 46]*	LA volume before atrial contraction
LA V_{min} [mL/m^2]	17.1	19 ± 5	[9, 28]	LA minimum volume
LA PassEF [%]	19.4	$26 \pm 9^*$	[8, 44]*	LA passive ejection fraction: $(V_{max} - V_{preAC})/V_{max}$
LA ActEF [%]	30.6	$37 \pm 10^*$	[17, 58]*	LA active ejection fraction: $(V_{preAC} - V_{min})/V_{preAC}$
LA TotEF [%]	44.1	54 ± 8	[37, 70]	LA total ejection fraction: $(V_{max} - V_{min})/V_{max}$
RV EDV [mL/m^2]	86.8	88 ± 17	[53, 123]	RV End Diastolic Volume
RV ESV [mL/m^2]	41.7	38 ± 11	[17, 59]	RV End Systolic Volume
RV SV [mL/m^2]	45.1	52 ± 12	[28, 75]	RV Stroke Volume (EDV – ESV)
RV EF [%]	51.9	57 ± 8	[42, 72]	RV ejection fraction (SV/EDV)
LV EDV [mL/m^2]	85.3	77 ± 15	[47, 107]	LV End Diastolic Volume
LV ESV [mL/m^2]	41.3	29 ± 9	[11, 47]	LV End Systolic Volume
LV SV [mL/m^2]	44.0	48 ± 9	[30, 66]	LV Stroke Volume (EDV – ESV)
LV EF [%]	51.6	63 ± 6	[51, 76]	LV ejection fraction (SV/EDV)

also in this case reducing the time step size does not solve this issue, but on the contrary it typically contributes to the onset of oscillations.

Thanks to the stabilization terms of Eq. (22) and Eq. (23) we are able to remove the non-physical oscillations, for any choice of parameters and of time step size. These numerical tests demonstrate that the interplay between accurate mathematical models and efficient and stable numerical methods is of fundamental importance to model the cardiac function and to obtain physiological results.

5.4.1. A quantitative analysis of volumetric indexes

Quantitative volume-based indexes of the four cardiac chambers are routinely used in clinics to assess the physiology of the heart. Reference values for these indexes are available in the medical literature, but their values significantly vary depending on the kind of medical images used or the methods employed to compute the volume. Echocardiography and cardiac magnetic resonance are the most used techniques, but the former usually underestimates the chambers' volume because of the low spatial resolution. Indeed, reference values for cardiac magnetic resonance [153,162] are consistently larger than the ones for echocardiography [78,81,152]. In both these techniques the volumes can be computed either using surrogate formulas (based on the chambers' area on specific image slices) or employing the more accurate Simpson's method (consisting in the segmentation of stack of contiguous slices that cover the whole cardiac chamber). Based on these considerations, in Table 2 we compare the volume-based indexes computed from the baseline simulation with the current reference ranges for cardiac magnetic resonance for adult men, computed using the Simpson's method. To this purpose we use values reported in the recent meta-analysis by Kawel-Boehm et al. [162] and some additional values focused on the atrial conduit and booster pump function from the study of Li et al. [153], being this paper the unique one of the meta-analysis reporting this kind of indexes – often computed in echocardiography [78,152] – for cardiac magnetic resonance. Concerning the atria, we compute all the indexes by not considering the appendages and the veins (which contribute about 25% of the total volume), as usually done in the image-based indexes such as the ones taken as reference ranges.

All the indexes calculated, both for the atria and for the ventricles, fall within the reference ranges. In conclusion, the results presented in this section demonstrate the ability of our whole-heart electromechanical model to capture most of the fundamental aspects of the healthy physiology of the heart. To the best of our knowledge, the cardiac function has never been modeled so comprehensively by a computational model of the heart.

6. Conclusions

In this paper, we proposed a biophysically detailed, numerically stable and accurate computational model of the electromechanics of the whole human heart, by considering an active contraction model for both atria and ventricles.

In developing whole-heart computation models, several aspects are crucial to comprehensively model the cardiac function and to accurately capture the highly coordinated events underlying the cardiac cycle. In this context, our model embeds different determinant features. We use an anatomically accurate computational domain including the main cardiac components such as atrial appendages, major arteries, and simplified cardiac valves (Fig. 3). In order to characterize the varying biophysical properties of the cardiac tissue, we split the whole domain into several regions, representing cardiac chambers, arteries, and insulating fibrous tissue of the cardiac valves. To capture the anisotropy of the muscular tissue, we model the myocardial fiber architecture by using the anatomically-accurate whole-heart LDRBM recently proposed in [51,62] in an extended version which includes crucial atrial anatomical features (Fig. 4). Our full electromechanical model comprises of several biophysically detailed core models. We employ chamber-specific and accurate ionic models for atria and ventricles [63,64], coupled with the monodomain equation to describe the transmembrane potential propagation at the macroscale. We use for the first time in a whole heart and for the atrial electromechanics the RDQ20 model [65] for the active force generation, a biophysically detailed microscale model that captures the crucial influence of the fibers-stretch and fibers-stretch-rate on the generation of the active forces. We extend the two-way coupling between ventricular electromechanics and closed-loop circulation [31] to the case of the four cardiac chambers. We use specific constitutive laws and model parameters for each cardiac region. The core models are mutually coupled by considering the most important feedbacks that represent the interactions among electric signal propagation, microscopic and macroscopic cardiac tissue contraction and deformation, and blood circulatory system (see Fig. 5). Among them, in this paper we pay special attention to the fibers-stretch-rate feedback (between passive mechanics and active force generation model). Concerning the numerical discretization, we extend to the whole heart the efficient segregated-intergrid-staggered scheme proposed in [31,32] for the ventricular case. In particular, we propose a computationally efficient strategy to handle the non-conductive regions in a distributed parallel computing setting and we introduce novel stabilization terms by extending recently developed stabilization techniques – related to the circulation [61] and the fibers-stretch-rate feedback [60] – to the whole heart, demonstrating their crucial role in a four-chamber scenario (see Fig. 7). To cope with the high computational complexity associated with whole-heart electromechanical simulations, we have developed our solver in `life`$^{\mathtt{x}}$, an efficient in-house FE library focused on large-scale cardiac applications in an HPC framework.

We simulate in a stable manner all the phases of the cardiac cycle for multiple heartbeats, showing numerical results that are able to reproduce the atrial and ventricular physiology, the threefold atrial function of reservoir, conduit and booster pump, and the atrioventricular interaction. To the best of our knowledge, some of the physiological features that we catch have never been shown all together by a computational model of the heart. Specifically, we mention the fluxes through the semilunar valves (Fig. 10), the eight-shaped atrial pressure–volume loops characterized by the correct proportion between A- and V-loops (Fig. 11), the evolution over time of the atrial volumes (Fig. 12), the a-, c-, v-waves of the atrial pressure (Fig. 12), and the three-dimensional deformation driven by the upward and downward movement of the atrioventricular plane (Fig. 13 and Video S1). More quantitatively, we compute volumetric indexes for all the cardiac chambers, finding values that always fall within the reference ranges for cardiovascular magnetic resonance [153,162] (Table 2).

We also analyze the impact of atrial contraction, fibers-stretch-rate feedback and stabilization terms, by comparing the results obtained with and without these features in the model. Due to the complex anatomy and physiology of the atria, atrial contraction is often neglected in electromechanical models of the whole heart [21,26,46,49,50]. However, we show that neglecting atrial contraction (and the associated atrial booster pump function acting as preload for the ventricles) means modeling a pathological rather than healthy scenario (Fig. 14). Concerning the fibers-stretch-rate feedback, we show that without this feedback the fluxes across the semilunar valves largely exceed the physiological

Table A.3
Parameters of the electrophysiological model ($\mathscr{E}$).

Variable	Value	Unit	Description
T_{hb}	0.8	s	Heartbeat duration
ϵ	0.05	–	Threshold of the fast conduction layer
$\left(\sigma_{\text{f}}^{\text{V,endo}}, \sigma_{\text{s}}^{\text{V,endo}}, \sigma_{\text{n}}^{\text{V,endo}}\right)/(\chi_{\text{m}} C_{\text{m}})$	$(8.00,\ 4.40,\ 2.20)\ \times 10^{-4}$	m^2/s	Ventricular fast layer conductivities
$\left(\sigma_{\text{f}}^{\text{V,myo}}, \sigma_{\text{s}}^{\text{V,myo}}, \sigma_{\text{n}}^{\text{V,myo}}\right)/(\chi_{\text{m}} C_{\text{m}})$	$(2.00,\ 1.10,\ 0.55)\ \times 10^{-4}$	m^2/s	Ventricular myocardial conductivities
$\left(\sigma_{\text{f}}^{\text{A}}, \sigma_{\text{s}}^{\text{A}}, \sigma_{\text{n}}^{\text{A}}\right)/(\chi_{\text{m}} C_{\text{m}})$	$(7.00,\ 1.41,\ 1.41)\ \times 10^{-4}$	m^2/s	Atrial conductivities
$\mathcal{I}_{\text{app}}/C_{\text{m}}$	25.71	V s^{-1}	Applied current value
δt	3.0	ms	Applied current duration
t_{RA}	0.0	ms	Applied current RA initial time
t_{LV}	(160, 160, 160)	ms	Applied current LV initial times
t_{RV}	(165, 172)	ms	Applied current RV initial times
r	3×10^{-3}	m	Applied current radius

range (Fig. 15). This feedback originates from the microscale force-velocity relationship of sarcomeres, decreasing the active force in regions where fibers are rapidly shortening. The macroscopic effect is a homogenization of fibers shortening velocity that, from a hemodynamic perspective, results into a smoothing of the ejected blood flux, as highlighted by our results. Hence, we postulate that the fibers-stretch-rate feedback, despite originating at the microscale, plays a crucial role in the macroscopic regulation of blood fluxes. Moreover, if not properly managed at the numerical level, this feedback produces non-physical oscillations that may lead the numerical simulation to fail [52,60]. Thus, the interplay between accurate mathematical models and efficient and stable numerical methods is of utmost importance to reproduce the heart physiology. We show that, thanks to the introduction of the stabilization terms relative to the circulation model and to the fibers-stretch-rate feedback, we are able to remove the non-physical oscillations (Figs. 16 and 17).

In conclusion, the electromechanical model presented in this study demonstrates exceptional ability in replicating essential aspects of healthy cardiac function in both the atria and ventricles. In this work, we do not merely tune models' parameters, but we actually propose novel methodologies which highlight the critical interplay between physiologically accurate mathematical models and numerical methods, including coupling strategies and stabilization techniques. Therefore, our model represents a significant step forward in the development of physics-based digital twins of the human heart, thus providing a valuable tool for advancing research in this field.

6.1. Limitations and future developments

The results shown in this paper are mainly focused on macroscopic mechanical biomarkers (such as pressure–volume loops, valvular flows, volume-based indexes). To the best of our knowledge, these were never reproduced with this accuracy by a computational model of the whole heart. In this context, the electrophysiology model has been setup by balancing accuracy and computational cost, being this model the most demanding in terms of space and time resolution. In particular, we focus on the reproduction of physiological conduction velocities (see Section 5.1) and activation times (Fig. 9), in order to properly trigger the mechanical contraction. However, this model presents some limitations if compared to computational models specifically focused on electrophysiology [9]. Specifically, we do not consider transmural heterogeneity of ionic models, we do not explicitly model the electrical conduction system and we use a mesh-size which is not fine enough to consider pathological scenarios. These limitations could also affect the accuracy of some local mechanical indicators, such as mechanical stresses. In the future, we aim to accurately assess pathologies involving anomalies of the electrical signal propagation (such as atrial fibrillation and ventricular tachycardia), overcoming the current limitations.

Concerning the mechanics, we plan to consider other passive constitutive laws than the Usyk one, such as the Holzapfel–Ogden model [106], which has been shown to offer some advantages, including better parameter identifiability [163]. Among other analyses, we will carry out an assessment of local stresses and local mechanical work, which were not the subject of the present work.

The cardiac function represents the result of a very critical balance among a large number of physical processes. In this context, we have compared the results of our simulations with reference ranges of some key biomarkers

Table A.4
Parameters of the active force generation model ($\mathscr{A}$) used in the ventricular (Ω_0^{V}) and atrial ($\Omega_0^{\mathrm{LA}} \cup \Omega_0^{\mathrm{RA}}$) domains, if modified from the calibration proposed in Regazzoni et al. [119].

Variable	Value	Unit	Description
Ventricles (Ω_0^{V})			
SL_0	1.9	μm	Reference sarcomere length
$(n_{\mathbf{f}}, n_{\mathbf{n}})$	(1, 0.4)	–	Share of active tension along the fiber and sheet-normal directions
$a_{\mathrm{XB}}^{\mathrm{LV}}$	15.0×10^8	Pa	LV upscaling constant of crossbridge stiffness
$a_{\mathrm{XB}}^{\mathrm{RV}}$	10.5×10^8	Pa	RV upscaling constant of crossbridge stiffness
$\bar{k}_{\mathrm{d}}$	0.36	μmol	Calcium-troponin dissociation constant
$\alpha_{k_{\mathrm{d}}}$	−0.2083	$\mu\mathrm{mol}\,\mu\mathrm{m}^{-1}$	Sensitivity to sarcomere length of calcium-troponin dissociation constant
γ	30	–	End-to-end tropomyosin cooperativity parameter
k_{off}	8	s^{-1}	Reaction rate associated with troponin kinetics
k_{basic}	4	s^{-1}	Reaction rate associated with tropomyosin kinetics
$\mu_{f_P}^0$	32.225	s^{-1}	Zero order moment of XB attachment rate
$\mu_{f_P}^1$	0.768	s^{-1}	First order moment of XB attachment rate
Atria ($\Omega_0^{\mathrm{LA}} \cup \Omega_0^{\mathrm{RA}}$)			
SL_0	1.9	μm	Reference sarcomere length
$(n_{\mathbf{f}}, n_{\mathbf{n}})$	(1, 0.4)	–	Share of active tension along the fiber and sheet-normal directions
$a_{\mathrm{XB}}^{\mathrm{LA}}$	30.0×10^7	Pa	LA upscaling constant of crossbridge stiffness
$a_{\mathrm{XB}}^{\mathrm{RA}}$	30.0×10^7	Pa	RA upscaling constant of crossbridge stiffness
$\bar{k}_{\mathrm{d}}$	0.865	μmol	Calcium-troponin dissociation constant
$\alpha_{k_{\mathrm{d}}}$	−1.25	$\mu\mathrm{mol}\,\mu\mathrm{m}^{-1}$	Sensitivity to sarcomere length of calcium-troponin dissociation constant
γ	20	–	End-to-end tropomyosin cooperativity parameter
k_{off}	180	s^{-1}	Reaction rate associated with troponin kinetics
k_{basic}	20	s^{-1}	Reaction rate associated with tropomyosin kinetics
$\mu_{f_P}^0$	32.225	s^{-1}	Zero order moment of XB attachment rate
$\mu_{f_P}^1$	0.768	s^{-1}	First order moment of XB attachment rate

Table A.5
Parameters of the mechanical model ($\mathscr{M}$).

Variable	Value	Unit	Description
B	50×10^3	Pa	Bulk modulus in the myocardium Ω_0^{myo}
b_{ff}	8	–	Fiber strain scaling in the myocardium Ω_0^{myo}
b_{ss}	6	–	Radial strain scaling in the myocardium Ω_0^{myo}
b_{nn}	3	–	Cross-fiber in-plain strain scaling in the myocardium Ω_0^{myo}
b_{fs}	12	–	Shear strain in fiber-sheet plane scaling in the myocardium Ω_0^{myo}
b_{fn}	3	–	Shear strain in fiber-normal plane scaling in the myocardium Ω_0^{myo}
b_{sn}	3	–	Shear strain in sheet-normal plane scaling in the myocardium Ω_0^{myo}
C^{V}	0.88×10^3	Pa	Material stiffness in the ventricular domain Ω_0^{V}
C^{RA}	1.47×10^3	Pa	Material stiffness in the right atrial domain Ω_0^{RA}
C^{LA}	1.76×10^3	Pa	Material stiffness in the left atrial domain Ω_0^{LA}
$\mu^{\mathrm{valve,caps}}$	10×10^5	Pa	Shear modulus in the domains $\{\Omega_0^{\mathrm{valve}} \cup \Omega_0^{\mathrm{caps}}\}$
$\kappa^{\mathrm{valve,caps}}$	50×10^5	Pa	Bulk modulus in the domains $\{\Omega_0^{\mathrm{valve}} \cup \Omega_0^{\mathrm{caps}}\}$
$\mu^{\mathrm{AO,PT}}$	5.25×10^5	Pa	Shear modulus in the arterial domains $\{\Omega_0^{\mathrm{AO}} \cup \Omega_0^{\mathrm{PT}}\}$
$\kappa^{\mathrm{AO,PT}}$	10×10^5	Pa	Bulk modulus in the arterial domains $\{\Omega_0^{\mathrm{AO}} \cup \Omega_0^{\mathrm{PT}}\}$
ρ_{s}	10^3	$\mathrm{kg\,m}^{-3}$	Tissue density in the whole domain Ω_0
$K_{\perp}^{\mathrm{epi,PF}}$	2×10^5	$\mathrm{Pa\,m}^{-1}$	Normal stiffness on $\Gamma^{\mathrm{epi,PF}}$
$C_{\perp}^{\mathrm{epi,PF}}$	2×10^3	$\mathrm{Pa\,s\,m}^{-1}$	Normal viscosity on $\Gamma^{\mathrm{epi,PF}}$
$K_{\perp}^{\mathrm{epi,EAT}}$	2×10^2	$\mathrm{Pa\,m}^{-1}$	Normal stiffness on $\Gamma^{\mathrm{epi,EAT}}$
$C_{\perp}^{\mathrm{epi,EAT}}$	2	$\mathrm{Pa\,s\,m}^{-1}$	Normal viscosity on $\Gamma^{\mathrm{epi,EAT}}$

for the healthy cardiac physiology. Thus, our model has not been validated against patient-specific measurements, which are outside the scope of the present work. Additionally, although we found an excellent match to healthy cardiac physiology in terms of various biomarkers, our results still have limitations in accurately capturing some

Table A.6
Parameters for the reference configuration recovery and the initial displacement computation ($\mathscr{M}^{\text{static}}$).

Variable	Value	Unit	Description
$\overline{p}_{\text{RA}}$	900	Pa	Residual RA pressure
$\overline{p}_{\text{LA}}$	1200	Pa	Residual LA pressure
$\overline{p}_{\text{RV}}$	650	Pa	Residual RV pressure
$\overline{p}_{\text{LV}}$	1150	Pa	Residual LV pressure
$\overline{p}_{\text{AO}}$	9500	Pa	Residual AO pressure
$\overline{p}_{\text{PT}}$	1700	Pa	Residual PT pressure
$\overline{T}_{\text{a,RA}}$	25.0×10^7	Pa	Residual RA active tension
$\overline{T}_{\text{a,LA}}$	25.0×10^7	Pa	Residual LA active tension
$\overline{T}_{\text{a,RV}}$	8.4×10^8	Pa	Residual RV active tension
$\overline{T}_{\text{a,LV}}$	12.0×10^8	Pa	Residual LV active tension

Table A.7
Parameters of the circulation model ($\mathscr{C}$).

Variable	Value	Unit	Variable	Value	Unit
$R_{\text{AR}}^{\text{SYS}}$	0.48	mmHg s mL^{-1}	$L_{\text{AR}}^{\text{SYS}}$	5×10^{-3}	mmHg s^2 mL^{-1}
$R_{\text{AR}}^{\text{PUL}}$	0.032116	mmHg s mL^{-1}	$L_{\text{AR}}^{\text{PUL}}$	5×10^{-4}	mmHg s^2 mL^{-1}
$R_{\text{VEN}}^{\text{SYS}}$	0.26	mmHg s mL^{-1}	$L_{\text{VEN}}^{\text{SYS}}$	5×10^{-4}	mmHg s^2 mL^{-1}
$R_{\text{VEN}}^{\text{PUL}}$	0.035684	mmHg s mL^{-1}	$L_{\text{VEN}}^{\text{PUL}}$	5×10^{-4}	mmHg s^2 mL^{-1}
$C_{\text{AR}}^{\text{SYS}}$	1.50	mL mmHg^{-1}	R_{min}	0.0075	mmHg s mL^{-1}
$C_{\text{AR}}^{\text{PUL}}$	10.0	mL mmHg^{-1}	R_{max}	75000	mmHg s mL^{-1}
$C_{\text{VEN}}^{\text{SYS}}$	60.0	mL mmHg^{-1}			
$C_{\text{VEN}}^{\text{PUL}}$	16.0	mL mmHg^{-1}			

physiological aspects. Among them, we mention the mischaracterization of diastolic flows, with an A-wave taller than the E-wave, the presence of pulmonary venous flow during atrial contraction, and the premature closure of the AV too soon after peak systolic pressure.

CRediT author statement

M. Fedele: Conceptualization, Formal analysis, Methodology, Software, Writing – original draft. **R. Piersanti**: Conceptualization, Formal analysis, Methodology, Software, Writing – original draft. **F. Regazzoni**: Conceptualization, Formal analysis, Methodology, Software, Writing – original draft. **M. Salvador**: Methodology, Software, Writing – review & editing. **P.C. Africa**: Methodology, Software, Writing – review & editing. **M. Bucelli**: Software, Writing – review & editing. **A. Zingaro**: Software, Writing – review & editing. **L. Dede'**: Conceptualization, Formal analysis, Project administration, Writing – review & editing. **A. Quarteroni**: Conceptualization, Funding acquisition, Project administration, Writing – review & editing.

Data availability

The authors do not have permission to share data.

Acknowledgments

This project has received funding from the European Research Council (ERC) under the European Union's Horizon 2020 research and innovation program (grant agreement No 740132, iHEART — An Integrated Heart Model for the simulation of the cardiac function, P.I. Prof. A. Quarteroni). We acknowledge the CINECA award under the class ISCRA B project (CoreMaS - code: HP10BD303V) for the availability of high performance computing resources. MS and AZ have received funding by the Italian Ministry of University and Research (MIUR) within the PRIN (Research projects of relevant national interest 2017 "Modeling the heart across the scales: from cardiac cells to the whole organ" Grant Registration number 2017AXL54F).

Table A.8
Tolerances of the linear solver for the different physics.

Physics/Fields	Linear solver	Preconditioner	Abs. tol.
Monodomain model	CG	AMG	10^{-10}
Activation	GMRES	AMG	10^{-10}
Mechanics	GMRES	AMG	10^{-8}

Table A.9
Tolerances of the nonlinear solver for the mechanical problem.

Physics/Fields	Nonlinear solver	Rel. tol.	Abs. tol.
Mechanics	Newton	10^{-8}	10^{-6}
Reference configuration	Newton	10^{-8}	10^{-6}

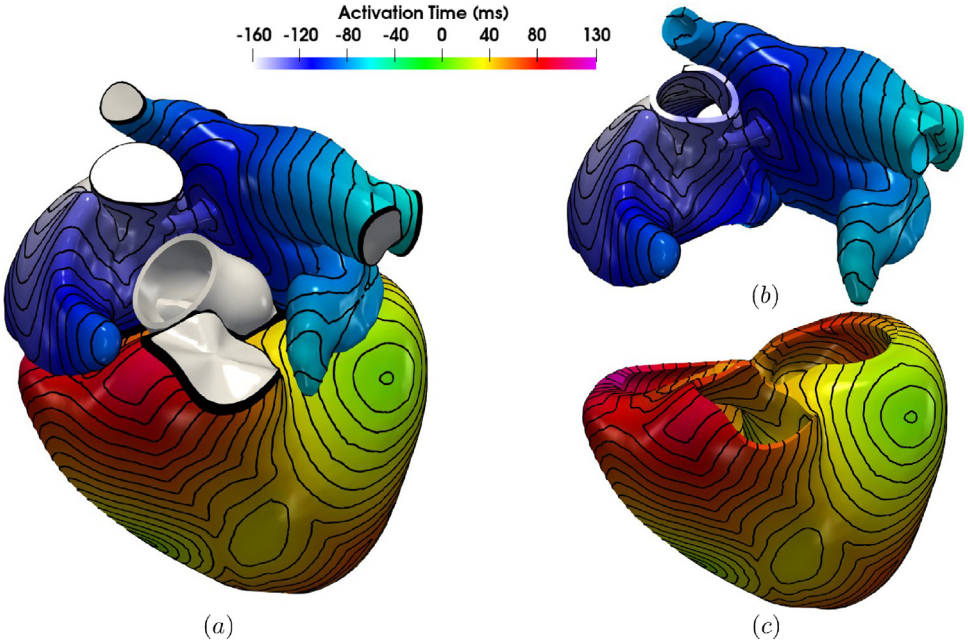

Fig. B.18. Numerical test for the treatment of the non-conductive regions in the electrophysiological model. Results in terms of activation times: (a) simulation in a unique whole-heart domain where atria and ventricles are connected by non-conductive regions; (b,c) two separated electrophysiological simulations in disjoint meshes for the atria (b) and ventricles (c).

European Research Council
Established by the European Commission

Appendix A. Model and numerical parameters

We provide more details about the parameters used for the baseline simulation (Section 5.2). Concerning the fiber generation procedure (Section 3.2), we use the parameters reported in Piersanti [83, Chapter 4]. In Table A.3 we report the parameters of the monodomain model ($\mathscr{E}$) of Eq. (3). Concerning the ionic models (4), we use the parameters reported in Courtemanche et al. [63] and ten Tusscher and Panfilov [64] (endocardium cells) for the atria (Eq. (4)a) and ventricles (Eq. (4)b), respectively. Additionally, for the TTP06 ionic model, we rescale the

calcium peak by a factor of 0.48 to bring the calcium transient into a more physiological range. In Table A.4 we report the calibration for the RDQ20 active generation model ($\mathscr{A}$) both for ventricles and atria. We only report parameters modified with respect to the original paper of Regazzoni et al. [119]. In particular, the atrial calibration is based on Mazhar et al. [120]. We also report the values of the microscale crossbridge stiffness a^i_{XB}, for $i \in \{\mathrm{RA}, \mathrm{LA}, \mathrm{RV}, \mathrm{LV}\}$, used to define the tissue level active tension of each cardiac chamber (see Eq. (13)). In Table A.5 we report the parameters of the passive mechanical model ($\mathscr{M}$) of Eq. (6). Additionally, in Table A.6 we report the specific parameters for the quasi-static approximation ($\mathscr{M}^{\mathrm{static}}$) of Eq. (20) used for the reference configuration recovery and the initial displacement computation (see Section 3.4). The parameters of the circulation model ($\mathscr{C}$) of Eqs. (7) and (17) are reported in Table A.7. Finally, concerning the numerical parameters, we report the setting used for the linear and nonlinear solvers in Tables A.8 and A.9, respectively.

Appendix B. A numerical verification test about the treatment of non-conductive regions

We perform a numerical test for the electrophysiological model ($\mathscr{E}$)–($\mathscr{I}$). First, we consider only the conductive domain Ω_0^{myo} by running two different simulations in two disjoints meshes for the atria (Ω_0^{A}) and ventricles (Ω_0^{V}). Then, we perform a simulation in the whole heart domain Ω_0 by treating the non-conductive regions as discussed in Section 4.2. In Fig. B.18 we show how the results in terms of activation time of these two scenarios match perfectly. Thus, our model is able to reproduce the physiological insulation between atria and ventricles, and the treatment of the non-conductive regions described in Section 4.2 effectively imposes insulating homogeneous Neumann conditions on the internal interfaces between conductive and non-conductive regions.

Appendix C. Supplementary data

Supplementary material related to this article can be found online at https://doi.org/10.1016/j.cma.2023.115983.

References

[1] N.A. Trayanova, Computational cardiology: the heart of the matter, Int. Sch. Res. Notices 2012 (2012) http://dx.doi.org/10.5402/2012/269680.
[2] R.A. Gray, P. Pathmanathan, Patient-specific cardiovascular computational modeling: diversity of personalization and challenges, J. Cardiovasc. Transl. Res. 11 (2) (2018) 80–88.
[3] S.A. Niederer, J. Lumens, N.A. Trayanova, Computational models in cardiology, Nat. Rev. Cardiol. 16 (2) (2019) 100–111, http://dx.doi.org/10.1038/s41569-018-0104-y.
[4] N.A. Trayanova, Whole-heart modeling applications to cardiac electrophysiology and electromechanics, Circ. Res. 108 (2011) 113–128.
[5] K. Gillette, M. Gsell, A. Prassl, E. Karabelas, U. Reiter, G. Reiter, T. Grandits, C. Payer, D. Stern, M. Urschler, J. Bayer, C. Augustin, A. Neic, T. Pock, E. Vigmond, G. Plank, A framework for the generation of digital twins of cardiac electrophysiology from clinical 12-leads ECGs, Med. Image Anal. 71 (2021) 102080.
[6] H.J. Arevalo, F. Vadakkumpadan, E. Guallar, A. Jebb, P. Malamas, K.C. Wu, N.A. Trayanova, Arrhythmia risk stratification of patients after myocardial infarction using personalized heart models, Nature Commun. 7 (1) (2016) 1–8.
[7] A. Prakosa, H. Arevalo, D. Deng, P. Boyle, P. Nikolov, H. Ashikaga, J.J.E. Blauer, E. Ghafoori, C.J. Park, R. Blake, F. Han, R. MacLeod, H. Halperin, D. Callans, R. Ranjan, J. Chrispin, S. Nazarian, N. Trayanova, Personalized virtual-heart technology for guiding the ablation of infarct-related ventricular tachycardia, Nat. Biomed. Eng. 2 (2018) 732–740.
[8] A. Frontera, S. Pagani, L.R. Limite, A. Peirone, F. Fioravanti, B. Enache, J. Cuellar Silva, K. Vlachos, C. Meyer, G. Montesano, et al., Slow conduction corridors and pivot sites characterize the electrical remodeling in atrial fibrillation, JACC Clin. Electrophysiol. 8 (5) (2022) 561–577, http://dx.doi.org/10.1016/j.jacep.2022.01.019.
[9] K. Gillette, M.A. Gsell, M. Strocchi, T. Grandits, A. Neic, M. Manninger, D. Scherr, C.H. Roney, A.J. Prassl, C.M. Augustin, et al., A personalized real-time virtual model of whole heart electrophysiology, Front. Phys. (2022) 1860.
[10] L. Marx, M.A.F. Gsell, A. Rund, et al., Personalization of electro-mechanical models of the pressure-overloaded left ventricle: fitting of windkessel-type afterload models, Phil. Trans. R. Soc. A 378 (2173) (2020) 20190342.
[11] A. Jung, M. Gsell, C. Augustin, G. Plank, An integrated workflow for building digital twins of cardiac electromechanics-a multi-fidelity approach for personalising active mechanics, Mathematics 10 (5) (2022).
[12] M. Salvador, M. Fedele, P.C. Africa, E. Sung, L. Dede', A. Prakosa, J. Chrispin, N. Trayanova, A. Quarteroni, Electromechanical modeling of human ventricles with ischemic cardiomyopathy: numerical simulations in sinus rhythm and under arrhythmia, Comput. Biol. Med. 136 (2021) 104674, http://dx.doi.org/10.1016/j.compbiomed.2021.104674.
[13] M. Peirlinck, F.S. Costabal, J. Yao, J.M. Guccione, S. Tripathy, Y. Wang, D. Ozturk, P. Segars, T.M. Morrison, S. Levine, E. Kuhl, Precision medicine in human heart modeling, Biomech. Model. Mechanobiol. 20 (3) (2021) 803–831, http://dx.doi.org/10.1007/s10237-021-01421-z.
[14] M. Peirlinck, J. Yao, F. Sahli Costabal, E. Kuhl, How drugs modulate the performance of the human heart, Comput. Mech. (2022) http://dx.doi.org/10.1007/s10237-021-01421-z.

[15] E. Karabelas, S. Longobardi, J. Fuchsberger, O. Razeghi, C. Rodero, M. Strocchi, R. Rajani, G. Haase, G. Plank, S. Niederer, Global sensitivity analysis of four chamber heart hemodynamics using surrogate models, IEEE Trans. Biomed. Eng. (2022) 1.
[16] R. Mittal, J.H. Seo, V. Vedula, Y.J. Choi, H. Liu, H.H. Huang, S. Jain, L. Younes, T. Abraham, R.T. George, Computational modeling of cardiac hemodynamics: Current status and future outlook, J. Comput. Phys. 305 (2016) 1065–1082, http://dx.doi.org/10.1016/j.jcp.2015.11.022.
[17] A. Zingaro, M. Bucelli, R. Piersanti, F. Regazzoni, L. Dede', A. Quarteroni, An electromechanics-driven fluid dynamics model for the simulation of the whole human heart, 2023, http://dx.doi.org/10.48550/arXiv.2301.02148, ArXiv Preprint.
[18] L. Feng, H. Gao, B.E. Griffith, S. Niederer, X. Luo, Analysis of a coupled fluid-structure interaction model of the left atrium and mitral valve, Int. J. Numer. Methods Biomed. Eng. 35 (11) (2019) e3254.
[19] B.E. Griffith, N.A. Patankar, Immersed methods for fluid-structure interaction, Annu. Rev. Fluid Mech. 52 (2020) 421–448, http://dx.doi.org/10.1146/annurev-fluid-010719-060228.
[20] C.S. Peskin, Numerical analysis of blood flow in the heart, J. Comput. Phys. 25 (3) (1977) 220–252.
[21] A. Santiago, J. Aguado-Sierra, M. Zavala-Aké, R. Doste-Beltran, S. Gómez, R. Arís, J.C. Cajas, E. Casoni, M. Vázquez, Fully coupled fluid-electro-mechanical model of the human heart for supercomputers, Int. J. Numer. Methods Biomed. Eng. 34 (12) (2018) e3140, http://dx.doi.org/10.1002/cnm.3140.
[22] R. Verzicco, Electro-fluid-mechanics of the heart, J. Fluid Mech. 941 (2022).
[23] E.J. Vigmond, C. Clements, D.M. McQueen, C.S. Peskin, Effect of bundle branch block on cardiac output: a whole heart simulation study, Prog. Biophys. Mol. Biol. 97 (2–3) (2008) 520–542.
[24] F. Viola, G. Del Corso, R. De Paulis, R. Verzicco, GPU accelerated digital twins of the human heart open new routes for cardiovascular research, 2022, Research Square Preprint.
[25] M. Bucelli, A. Zingaro, P.C. Africa, I. Fumagalli, L. Dede', A. Quarteroni, A mathematical model that integrates cardiac electrophysiology, mechanics, and fluid dynamics: Application to the human left heart, Int. J. Numer. Methods Biomed. Eng. (2023) e3678, http://dx.doi.org/10.1002/cnm.3678.
[26] C.M. Augustin, A. Neic, M. Liebmann, A.J. Prassl, S.A. Niederer, G. Haase, G. Plank, Anatomically accurate high resolution modeling of human whole heart electromechanics: A strongly scalable algebraic multigrid solver method for nonlinear deformation, J. Comput. Phys. 305 (2016) 622–646, http://dx.doi.org/10.1016/j.jcp.2015.10.045.
[27] A. Quarteroni, T. Lassila, S. Rossi, R. Ruiz-Baier, Integrated heart - coupling multiscale and multiphysics models for the simulation of the cardiac function, Comput. Methods Appl. Mech. Engrg. 314 (2017) 345–407.
[28] A. Gerbi, L. Dede', A. Quarteroni, A monolithic algorithm for the simulation of cardiac electromechanics in the human left ventricle, Math. Eng. 1 (1) (2019) 1–37, http://dx.doi.org/10.3934/Mine.2018.1.1.
[29] F. Viola, V. Meschini, R. Verzicco, Fluid–structure-electrophysiology interaction (FSEI) in the left-heart: a multi-way coupled computational model, Eur. J. Mech. B Fluids 79 (2020) 212–232, http://dx.doi.org/10.1016/j.euromechflu.2019.09.006.
[30] M. Strocchi, C.M. Augustin, M.A.F. Gsell, E. Karabelas, A. Neic, K. Gillette, O. Razeghi, A.J. Prassl, E.J. Vigmond, J.M. Behar, J. Gould, B. Sidhu, C.A. Rinaldi, M.J. Bishop, G. Plank, S.A. Niederer, A publicly available virtual cohort of four-chamber heart meshes for cardiac electro-mechanics simulations, PLoS One 15 (6) (2020) e0235145, http://dx.doi.org/10.1371/journal.pone.0235145.
[31] F. Regazzoni, M. Salvador, P. Africa, M. Fedele, L. Dedè, A. Quarteroni, A cardiac electromechanical model coupled with a lumped-parameter model for closed-loop blood circulation, J. Comput. Phys. 457 (2022) 111083, http://dx.doi.org/10.1016/j.jcp.2022.111083.
[32] R. Piersanti, F. Regazzoni, M. Salvador, A.F. Corno, L. Dede', C. Vergara, A. Quarteroni, 3D–0D closed-loop model for the simulation of cardiac biventricular electromechanics, Comput. Methods Appl. Mech. Engrg. 391 (2022) 114607, http://dx.doi.org/10.1016/j.cma.2022.114607.
[33] S. Stella, F. Regazzoni, C. Vergara, L. Dede', A. Quarteroni, A fast cardiac electromechanics model coupling the Eikonal and the nonlinear mechanics equations, Math. Models Methods Appl. Sci. (2022) http://dx.doi.org/10.1142/S0218202522500439.
[34] A. Zingaro, I. Fumagalli, L. Dede, M. Fedele, P.C. Africa, A.F. Corno, A. Quarteroni, A geometric multiscale model for the numerical simulation of blood flow in the human left heart, Discrete Contin. Dyn. Syst. Ser. S (2022) http://dx.doi.org/10.3934/dcdss.2022052.
[35] L. Cicci, S. Fresca, S. Pagani, A. Manzoni, A. Quarteroni, Projection-based reduced order models for parameterized nonlinear time-dependent problems arising in cardiac mechanics, Math. Eng. 5 (2) (2023) 1–38, http://dx.doi.org/10.3934/mine.2023026.
[36] P.C. Africa, M. Salvador, P. Gervasio, L. Dede', A. Quarteroni, A matrix–free high–order solver for the numerical solution of cardiac electrophysiology, J. Comput. Phys. 478 (2023) 111984, http://dx.doi.org/10.1016/j.jcp.2023.111984.
[37] D. Sánchez-Quintana, M. Doblado-Calatrava, J.A. Cabrera, Y. Macías, F. Saremi, Anatomical basis for the cardiac interventional electrophysiologist, Biomed Res. Int. 2015 (2015).
[38] A.M. Katz, Physiology of the Heart, Lippincott Williams & Wilkins, 2010.
[39] T.P. Usyk, I.J. LeGrice, A.D. McCulloch, Computational model of three-dimensional cardiac electromechanics, Comput. Vis. Sci. 4 (4) (2002) 249–257.
[40] N.P. Smith, D.P. Nickerson, E.J. Crampin, et al., Multiscale computational modelling of the heart, Acta Numer. 13 (2004) 371–431.
[41] S. Göktepe, E. Kuhl, Electromechanics of the heart: a unified approach to the strongly coupled excitation-contraction problem, Comput. Mech. 45 (2010) 227–243.
[42] D.A. Nordsletten, S.A. Niederer, M.P. Nash, et al., Coupling multi-physics models to cardiac mechanics, Prog. Biophys. Mol. Biol. 104 (2011) 77–88.
[43] M. Genet, L.C. Lee, R. Nguyen, H. Haraldsson, G. Acevedo-Bolton, Z. Zhang, L. Ge, K. Ordovas, S. Kozerke, J.M. Guccione, Distribution of normal human left ventricular myofiber stress at end diastole and end systole: a target for in silico design of heart failure treatments, J. Appl. Physiol. 117 (2) (2014) 142–152.

[44] A. Quarteroni, L. Dede', A. Manzoni, C. Vergara, Mathematical Modelling of the Human Cardiovascular System: Data, Numerical Approximation, Clinical Applications, Cambridge University Press, 2019.
[45] S. Sugiura, T. Washio, A. Hatano, J. Okada, H. Watanabe, T. Hisada, Multi-scale simulations of cardiac electrophysiology and mechanics using the University of Tokyo heart simulator, Prog. Biophys. Mol. Biol. 110 (2–3) (2012) 380–389, http://dx.doi.org/10.1016/j.pbiomolbio.2012.07.001.
[46] T. Fritz, C. Wieners, G. Seemann, H. Steen, O. Dössel, Simulation of the contraction of the ventricles in a human heart model including atria and pericardium, Biomech. Model. Mechanobiol. 13 (3) (2014) 627–641, http://dx.doi.org/10.1007/s10237-013-0523-y.
[47] B. Baillargeon, N. Rebelo, D.D. Fox, R.L. Taylor, E. Kuhl, The living heart project: A robust and integrative simulator for human heart function, Eur. J. Mech. A Solids 48 (1) (2014) 38–47, http://dx.doi.org/10.1016/j.euromechsol.2014.04.001.
[48] S. Land, S.A. Niederer, Influence of atrial contraction dynamics on cardiac function, Int. J. Numer. Methods Biomed. Eng. 34 (3) (2018) e2931, http://dx.doi.org/10.1002/cnm.2931.
[49] M.R. Pfaller, J.M. Hörmann, M. Weigl, A. Nagler, R. Chabiniok, C. Bertoglio, W.A. Wall, The importance of the pericardium for cardiac biomechanics: from physiology to computational modeling, Biomech. Model. Mechanobiol. 18 (2) (2019) 503–529, http://dx.doi.org/10.1007/s10237-018-1098-4.
[50] M. Strocchi, M.A. Gsell, C.M. Augustin, O. Razeghi, C.H. Roney, A.J. Prassl, E.J. Vigmond, J.M. Behar, J.S. Gould, C.A. Rinaldi, M.J. Bishop, G. Plank, S.A. Niederer, Simulating ventricular systolic motion in a four-chamber heart model with spatially varying robin boundary conditions to model the effect of the pericardium, J. Biomech. 101 (2020) 109645, http://dx.doi.org/10.1016/j.jbiomech.2020.109645.
[51] R. Piersanti, P.C. Africa, M. Fedele, C. Vergara, L. Dedè, A.F. Corno, A. Quarteroni, Modeling cardiac muscle fibers in ventricular and atrial electrophysiology simulations, Comput. Methods Appl. Mech. Engrg. 373 (2021) 113468, http://dx.doi.org/10.1016/j.cma.2020.113468.
[52] T. Gerach, S. Schuler, J. Fröhlich, L. Lindner, E. Kovacheva, R. Moss, E.M. Wülfers, G. Seemann, C. Wieners, A. Loewe, Electro-mechanical whole-heart digital twins: A fully coupled multi-physics approach, Mathematics 9 (11) (2021) 1247, http://dx.doi.org/10.3390/math9111247.
[53] G. Del Corso, R. Verzicco, F. Viola, A fast computational model for the electrophysiology of the whole human heart, J. Comput. Phys. 457 (2022) 111084, http://dx.doi.org/10.1016/j.jcp.2022.111084.
[54] K. Yoneda, J. Okada, M. Watanabe, S. Sugiura, T. Hisada, T. Washio, A multiple step active stiffness integration scheme to couple a stochastic cross-bridge model and continuum mechanics for uses in both basic research and clinical applications of heart simulation, Front. Phys. 12 (2021).
[55] S. Sugiura, J. Okada, T. Washio, T. Hisada, UT-heart: A finite element model designed for the multiscale and multiphysics integration of our knowledge on the human heart, in: Computational Systems Biology in Medicine and Biotechnology: Methods and Protocols, Springer US, New York, NY, 2022, pp. 221–245.
[56] Zygote, Zygote Solid 3D Male Anatomy Collection Generation II Developent Report, Technical Report, 2014.
[57] B. Baillargeon, I. Costa, J.R. Leach, L.C. Lee, M. Genet, A. Toutain, J.F. Wenk, M.K. Rausch, N. Rebelo, G. Acevedo-Bolton, et al., Human cardiac function simulator for the optimal design of a novel annuloplasty ring with a sub-valvular element for correction of ischemic mitral regurgitation, Cardiovasc. Eng. Technol. 6 (2) (2015) 105–116, http://dx.doi.org/10.1007/s13239-015-0216-z.
[58] M. Genet, L.C. Lee, B. Baillargeon, J.M. Guccione, E. Kuhl, Modeling pathologies of diastolic and systolic heart failure, Ann. Biomed. Eng. 44 (1) (2016) 112–127.
[59] S. Land, S.-J. Park-Holohan, N.P. Smith, C.G. Dos Remedios, J.C. Kentish, S.A. Niederer, A model of cardiac contraction based on novel measurements of tension development in human cardiomyocytes, J. Mol. Cell. Cardiol. 106 (2017) 68–83.
[60] F. Regazzoni, A. Quarteroni, An oscillation-free fully partitioned scheme for the numerical modeling of cardiac active mechanics, Comput. Methods Appl. Mech. Engrg. 373 (2021) 113506.
[61] F. Regazzoni, Stabilization of Staggered Time Discretization Schemes for 0D-3D, Fluid-Structure Interaction Problems, MOX Report 17, 2022.
[62] R. Piersanti, C. Vergara, L. Dedè, A. Quarteroni, Modeling Whole Heart Muscle Fibers in Cardiac Computational Models, ARGESIM Report 17, 2022, pp. 75–76.
[63] M. Courtemanche, R.J. Ramirez, S. Nattel, Ionic mechanisms underlying human atrial action potential properties: insights from a mathematical model, Am. J. Physiol.-Heart Circ. Physiol. 275 (1) (1998) H301–H321.
[64] K.H. ten Tusscher, A.V. Panfilov, Alternans and spiral breakup in a human ventricular tissue model, Am. J. Physiol.Heart Circ. Physiol. 291 (2006) 1088–1100.
[65] F. Regazzoni, L. Dedè, A. Quarteroni, Machine learning of multiscale active force generation models for the efficient simulation of cardiac electromechanics, Comput. Methods Appl. Mech. Engrg. 370 (2020) 113268, http://dx.doi.org/10.1016/j.cma.2020.113268.
[66] P.C. Africa, `Life`$^{\mathtt{x}}$: A flexible, high performance library for the numerical solution of complex finite element problems, SoftwareX 20 (2022) 101252, http://dx.doi.org/10.1016/j.softx.2022.101252.
[67] P.C. Africa, `life`$^{\mathtt{x}}$: A Flexible, High Performance Library for the Numerical Solution of Complex Finite Element Problems, Zenodo, 2022, http://dx.doi.org/10.5281/zenodo.6941115, URL https://lifex.gitlab.io/.
[68] L.H. Opie, Heart Physiology: From Cell To Circulation, Lippincott Williams & Wilkins, 2004.
[69] R.H. Anderson, R. Razavi, A.M. Taylor, Cardiac anatomy revisited, J. Anat. 205 (3) (2004) 159–177.
[70] P.A. Iaizzo, Handbook of Cardiac Anatomy, Physiology, and Devices, Springer Science & Business Media, 2010.
[71] R. Klabunde, Cardiovascular Physiology Concepts, Lippincott Williams & Wilkins, 2011.
[72] A.T. Askari, A.W. Messerli, Cardiovascular Hemodynamics: An Introductory Guide, Springer International Publishing, 2019, http://dx.doi.org/10.1007/978-3-030-19131-3.

[73] F. Regazzoni, L. Dedè, A. Quarteroni, Biophysically detailed mathematical models of multiscale cardiac active mechanics, PLoS Comput. Biol. 16 (10) (2020) e1008294, http://dx.doi.org/10.1371/journal.pcbi.1008294.
[74] P.S. Pagel, J.K. Freed, Cardiac physiology, in: Kaplan's Essentials of Cardiac Anesthesia, Elsevier, 2018, pp. 62–79, http://dx.doi.org/10.1016/B978-0-323-49798-5.00004-8.
[75] K. Spencer, V. Mor-Avi, J.r. Gorcsan, A. DeMaria, T. Kimball, M. Monaghan, J. Perez, L. Weinert, J. Bednarz, K. Edelman, et al., Effects of aging on left atrial reservoir, conduit, and booster pump function: a multi-institution acoustic quantification study, Heart 85 (3) (2001) 272–277.
[76] Q. Cui, H. Wang, W. Zhang, H. Wang, X. Sun, Y. Zhang, H. Yang, Enhanced left atrial reservoir, increased conduit, and weakened booster pump function in hypertensive patients with paroxysmal atrial fibrillation, Hypertension Res. 31 (3) (2008) 395–400.
[77] W.P. Abhayaratna, K. Fatema, M.E. Barnes, J.B. Seward, B.J. Gersh, K.R. Bailey, G. Casaclang-Verzosa, T.S. Tsang, Left atrial reservoir function as a potent marker for first atrial fibrillation or flutter in persons≥ 65 years of age, Am. J. Cardiol. 101 (11) (2008) 1626–1629.
[78] G.G. Blume, C.J. Mcleod, M.E. Barnes, J.B. Seward, P.A. Pellikka, P.M. Bastiansen, T.S.M. Tsang, Left atrial function: physiology, assessment, and clinical implications, Eur. J. Echocardiogr. 12 (6) (2011) 421–430, http://dx.doi.org/10.1093/ejechocard/jeq175, URL https://academic.oup.com/ehjcimaging/article-lookup/doi/10.1093/ejechocard/jeq175.
[79] M. Roşca, P. Lancellotti, B.A. Popescu, L.A. Piérard, Left atrial function: pathophysiology, echocardiographic assessment, and clinical applications, Heart 97 (23) (2011) 1982–1989.
[80] B.D. Hoit, Left atrial size and function: role in prognosis, J. Am. Coll. Cardiol. 63 (6) (2014) 493–505.
[81] R.M. Lang, L.P. Badano, V. Mor-Avi, J. Afilalo, A. Armstrong, L. Ernande, F.A. Flachskampf, E. Foster, S.A. Goldstein, T. Kuznetsova, et al., Recommendations for cardiac chamber quantification by echocardiography in adults: an update from the American society of echocardiography and the European association of cardiovascular imaging, Eur. Heart J.-Cardiovasc. Imaging 16 (3) (2015) 233–271, http://dx.doi.org/10.1093/ehjci/jev014.
[82] P.N. Marino, Left atrial conduit function: A short review, Physiol. Rep. 9 (19) (2021) e15053.
[83] R. Piersanti, Mathematical and Numerical Modeling of Cardiac Fiber Generation and Electromechanical Function : Towards a Realistic Simulation of the Whole Heart (Ph.D. thesis), Politecnico di Milano, 2021, URL http://hdl.handle.net/10589/183040.
[84] J. Bayer, R. Blake, G. Plank, N. Trayanova, A novel rule-based algorithm for assigning myocardial fiber orientation to computational heart models, Ann. Biomed. Eng. 40 (10) (2012) 2243–2254.
[85] R. Doste, D. Soto-Iglesias, G. Bernardino, A. Alcaine, R. Sebastian, S. Giffard-Roisin, M. Sermesant, A. Berruezo, D. Sanchez-Quintana, O. Camara, A rule-based method to model myocardial fiber orientation in cardiac biventricular geometries with outflow tracts, Int. J. Numer. Methods Biomed. Eng. 35 (4) (2019) e3185.
[86] D. Sánchez-Quintana, M. Doblado-Calatrava, J.A. Cabrera, Y. Macías, F. Saremi, Anatomical basis for the cardiac interventional electrophysiologist, Biomed Res. Int. 2015 (2015).
[87] A.U. Siddiqui, S.R.H. Daimi, K.R. Gandhi, A.T. Siddiqui, S. Trivedi, M.B. Sinha, M. Rathore, Crista terminalis, musculi pectinati, and taenia sagittalis: anatomical observations and applied significance, Int. Sch. Res. Notices 2013 (2013).
[88] C. Luo, Y. Rudy, A model of the ventricular cardiac action potential. Depolarization, repolarization, and their interaction, Circ. Res. 68 (1991) 1501–1526.
[89] C. Luo, Y. Rudy, A dynamic model of the cardiac ventricular action potential. I. simulations of ionic currents and concentration changes, Circ. Res. 74 (1994) 1071–1096.
[90] R.R. Aliev, A.V. Panfilov, A simple two-variable model of cardiac excitation, Chaos Solitons Fractals 7 (1996) 293–301.
[91] K.H. ten Tusscher, D. Noble, P.J. Noble, A.V. Panfilov, A model for human ventricular tissue, Am. J. Physiol.Heart Circ. Physiol. 286 (2004) 1573–1589.
[92] A. Bueno-Orovio, E.M. Cherry, F.H. Fenton, Minimal model for human ventricular action potentials in tissue, J. Theoret. Biol. 253 (2008) 544–560.
[93] J. Tomek, A. Bueno-Orovio, E. Passini, X. Zhou, A. Minchole, O. Britton, C. Bartolucci, S. Severi, A. Shrier, L. Virag, et al., Development, calibration, and validation of a novel human ventricular myocyte model in health, disease, and drug block, Elife 8 (2019) e48890.
[94] C.S. Henriquez, Simulating the electrical behavior of cardiac tissue using the bidomain model, Crit. Rev. Biomed. Eng. 21 (1) (1993) 1–77.
[95] A. Pullan, M.L. Buist, L.K. Cheng, Mathematically Modelling the Electrical Activity of the Heart: From Cell To Body Surface and Back Again, World Scientific Publishing Company, 2005.
[96] M. Potse, B. Dubé, J. Richer, et al., A comparison of monodomain and bidomain reaction-diffusion models for action potential propagation in the human heart, IEEE Trans. Biomed. Eng. 53 (2006) 2425–2435.
[97] P. Colli Franzone, L.F. Pavarino, G. Savaré, Computational electrocardiology: mathematical and numerical modeling, in: Complex Systems in Biomedicine, Springer, 2006, pp. 187–241.
[98] P. Colli Franzone, L.F. Pavarino, S. Scacchi, Mathematical Cardiac Electrophysiology, Springer, 2014.
[99] S. Rossi, R. Ruiz-Baier, L.F. Pavarino, A. Quarteroni, Orthotropic active strain models for the numerical simulation of cardiac biomechanics, Int. J. Numer. Methods Biomed. Eng. 28 (2012) 761–788.
[100] S. Rossi, T. Lassila, R. Ruiz-Baier, et al., Thermodynamically consistent orthotropic activation model capturing ventricular systolic wall thickening in cardiac electromechanics, Eur. J. Mech. A Solids 48 (2014) 129–142.
[101] R. Ruiz-Baier, A. Gizzi, S. Rossi, et al., Mathematical modelling of active contraction in isolated cardiomyocytes, Math. Med. Biol. 31 (2014) 259–283.
[102] R. Ogden, Non-Linear Elastic Deformations, Dover Publications, 1997.

[103] J.M. Guccione, A.D. McCulloch, L.K. Waldman, Passive material properties of intact ventricular myocardium determined from a cylindrical model, J. Biomech. Eng. 113 (1991) 42–55.
[104] J.M. Guccione, A.D. McCulloch, Mechanics of active contraction in cardiac muscle: Part I—Constitutive relations for fiber stress that describe deactivation, J. Biomech. Eng. 115 (1) (1993) 72–81, http://dx.doi.org/10.1115/1.2895473.
[105] J.M. Guccione, L. Waldman, A.D. McCulloch, Mechanics of active contraction in cardiac muscle: Part II—Cylindrical models of the systolic left ventricle, J. Biomech. Eng. 115 (1) (1993) 82–90.
[106] G.A. Holzapfel, R.W. Ogden, Constitutive modelling of passive myocardium: a structurally based framework for material characterization, Math. Phys. Eng. Sci. 367 (2009) 3445–3475.
[107] P.J. Blanco, R.A. Feijóo, A 3D–1D–0D computational model for the entire cardiovascular system, Comput. Mech. 24 (2010) 5887–5911.
[108] M. Hirschvogel, M. Bassilious, L. Jagschies, et al., A monolithic 3D–0D coupled closed-loop model of the heart and the vascular system: Experiment-based parameter estimation for patient-specific cardiac mechanics, Int. J. Numer. Methods Biomed. Eng. 33 (8) (2017) e2842.
[109] P. Kohl, U. Ravens, Cardiac mechano-electric feedback: past, present, and prospect, Prog. Biophys. Mol. Biol. 82 (1–3) (2003) 3–9, http://dx.doi.org/10.1016/S0079-6107(03)00022-1.
[110] A. Lee, U. Nguyen, O. Razeghi, J. Gould, B. Sidhu, B. Sieniewicz, J. Behar, M. Mafi-Rad, G. Plank, F. Prinzen, et al., A rule-based method for predicting the electrical activation of the heart with cardiac resynchronization therapy from non-invasive clinical data, Med. Image. Anal. 57 (2019) 197–213.
[111] C. Vergara, S. Palamara, D. Catanzariti, F. Nobile, E. Faggiano, C. Pangrazzi, M. Centonze, M. Maines, A. Quarteroni, G. Vergara, Patient-specific generation of the purkinje network driven by clinical measurements of a normal propagation, Med. Biol. Eng. Com. 52 (2014) 813–826.
[112] C. Vergara, M. Lange, S. Palamara, T. Lassila, A. Frangi, A. Quarteroni, A coupled 3D–1D numerical monodomain solver for cardiac electrical activation in the myocardium with detailed Purkinje network, J. Comput. Phys. 308 (2016) 218–238.
[113] F. Costabal, D. Hurtado, E. Kuhl, Generating Purkinje networks in the human heart, J. Biomech. 49 (2016) 2455–2465.
[114] M. Landajuela, C. Vergara, A. Gerbi, L. Dede', L. Formaggia, A. Quarteroni, Numerical approximation of the electromechanical coupling in the left ventricle with inclusion of the Purkinje network, Int. J. Numer. Methods Biomed. Eng. 34 (2018) e2984, http://dx.doi.org/10.1002/cnm.2984.
[115] A. Ferrer, R. Sebastián, D. Sánchez-Quintana, J. Rodríguez, E. Godoy, L. Martínez, J. Saiz, Detailed anatomical and electrophysiological models of human atria and torso for the simulation of atrial activation, PLoS One 10 (11) (2015) e0141573.
[116] O. Dössel, M. Krueger, F. Weber, M. Wilhelms, G. Seemann, Computational modeling of the human atrial anatomy and electrophysiology, Med. Biol. Eng. Comput. 50 (2012) 773–799.
[117] R. Lemery, D. Birnie, A. Tang, M. Green, M. Gollob, M. Hendry, E. Lau, Normal atrial activation and voltage during sinus rhythm in the human heart: an endocardial and epicardial mapping study in patients with a history of atrial fibrillation, J. Cardiovascul. Electrophysiol. 18 (4) (2007) 402–408.
[118] F. Regazzoni, L. Dedè, A. Quarteroni, Active force generation in cardiac muscle cells: mathematical modeling and numerical simulation of the actin-myosin interaction, Vietnam J. Math. 49 (2021) 87–118.
[119] F. Regazzoni, M. Salvador, L. Dedè, A. Quarteroni, A machine learning method for real-time numerical simulations of cardiac electromechanics, Comput. Methods Appl. Mech. Engrg. 393 (2022) 114825.
[120] F. Mazhar, F. Regazzoni, C. Bartolucci, C. Corsi, L. Dede', A. Quarteroni, S. Severi, Electro-mechanical coupling in human atrial cardiomyocytes: Model development and analysis of inotropic interventions, in: 2021 Computing in Cardiology (CinC), 2021-Septe, IEEE, 2021, pp. 1–4, http://dx.doi.org/10.23919/CinC53138.2021.9662766.
[121] F. Regazzoni, L. Dedè, A. Quarteroni, Active contraction of cardiac cells: a reduced model for sarcomere dynamics with cooperative interactions, Biomech. Model. Mechanobiol. 17 (2018) 1663–1686.
[122] J.M. Guccione, A.D. McCulloch, Finite element modeling of ventricular mechanics, in: Theory of Heart, Springer, 1991, pp. 121–144.
[123] A. Cheng, F. Langer, F. Rodriguez, et al., Transmural cardiac strains in the lateral wall of the ovine left ventricle, Am. J. Physiol-Heart Circ. Physiol. 288 (2005) 1546–1556.
[124] S. Doll, K. Schweizerhof, On the development of volumetric strain energy functions, J. Appl. Math. 67 (2000) 17–21.
[125] F.C. Yin, C.C. Chan, R.M. Judd, Compressibility of perfused passive myocardium, Am. J. Physiol. Heart Circ. Physiol. 271 (1996) 1864–1870.
[126] D. Guan, J. Yao, X. Luo, H. Gao, Effect of myofibre architecture on ventricular pump function by using a neonatal porcine heart model: from DT-MRI to rule-based methods, R. Soc. Open Sci. 7 (4) (2020) 191655.
[127] D. Guan, X. Zhuan, W. Holmes, X. Luo, H. Gao, Modelling of fibre dispersion and its effects on cardiac mechanics from diastole to systole, J. Eng. Math. 128 (1) (2021) 1–24.
[128] F. Regazzoni, Mathematical Modeling and Machine Learning for the Numerical Simulation of Cardiac Electromechanics (Ph.D. thesis), Politecnico di Milano, 2020.
[129] D. Nordsletten, S. Niederer, M. Nash, P. Hunter, N. Smith, Coupling multi-physics models to cardiac mechanics, Prog. Biophys. Mol. Biol. 104 (2011) 77–88.
[130] A. Quarteroni, Numerical Models for Differential Problems, Vol. 2, Springer, 2009.
[131] S. Krishnamoorthi, M. Sarkar, W. Klug, Numerical quadrature and operator splitting in finite element methods for cardiac electrophysiology, Int. J. Numer. Methods Biomed. Eng. 29 (2013) 1243–1266.
[132] P. Colli Franzone, L.F. Pavarino, S. Scacchi, A numerical study of scalable cardiac electro-mechanical solvers on HPC architectures, Front. Phys. 9 (2018) 268.

[133] M. Salvador, L. Dedè, A. Quarteroni, An intergrid transfer operator using radial basis functions with application to cardiac electromechanics, Comput. Mech. 66 (2020) 491–511.
[134] J.P. Whiteley, M.J. Bishop, D.J. Gavaghan, Soft tissue modelling of cardiac fibres for use in coupled mechano-electric simulations, Bull. Math. Biol. 69 (7) (2007) 2199–2225.
[135] S.A. Niederer, N.P. Smith, An improved numerical method for strong coupling of excitation and contraction models in the heart, Prog. Biophys. Mol. Biol. 96 (1–3) (2008) 90–111.
[136] P. Pathmanathan, J.P. Whiteley, A numerical method for cardiac mechanoelectric simulations, Ann. Biomed. Eng. 37 (5) (2009) 860–873.
[137] P. Pathmanathan, S. Chapman, D. Gavaghan, J. Whiteley, Cardiac electromechanics: the effect of contraction model on the mathematical problem and accuracy of the numerical scheme, Quart. J. Mech. Appl. Math. 63 (3) (2010) 375–399.
[138] M. Benzi, G. Golub, J. Liesen, et al., Numerical solution of saddle point problems, Acta Numer. 14 (2005) 1–137.
[139] M. Fedele, A. Quarteroni, Polygonal surface processing and mesh generation tools for the numerical simulation of the cardiac function, Int. J. Numer. Methods Biomed. Eng. 37 (4) (2021) e3435, http://dx.doi.org/10.1002/cnm.3435.
[140] L. Antiga, M. Piccinelli, L. Botti, B. Ene-Iordache, A. Remuzzi, D.A. Steinman, An image-based modeling framework for patient-specific computational hemodynamics, Med. Biol. Eng. Comput. 46 (11) (2008) 1097–1112, http://dx.doi.org/10.1007/s11517-008-0420-1.
[141] C.M. Augustin, T.E. Fastl, A. Neic, C. Bellini, J. Whitaker, R. Rajani, M.D. O'Neill, M.J. Bishop, G. Plank, S.A. Niederer, The impact of wall thickness and curvature on wall stress in patient-specific electromechanical models of the left atrium, Biomech. Model. Mechanobiol. 19 (3) (2020) 1015–1034.
[142] D. Arndt, W. Bangerth, T. Clevenger, D. Davydov, M. Fehling, D. Garcia-Sanchez, G. Harper, T. Heister, L. Heltai, M. Kronbichler, R. Kynch, M. Maier, J.-P. Pelteret, B. Turcksin, D. Wells, The `deal.II` Library, Version 9.1, J. Numer. Math. (2019).
[143] P.C. Africa, R. Piersanti, M. Fedele, L. Dede', A. Quarteroni, An open tool based on `life`^{x} for myofibers generation in cardiac computational models, 2022, http://dx.doi.org/10.48550/arXiv.2201.03303, ArXiv Preprint.
[144] J.R. Mitchell, J.-J. Wang, Expanding application of the Wiggers diagram to teach cardiovascular physiology, Adv. Physiol. Ed. 38 (2) (2014) 170–175.
[145] D. Gallo, G. De Santis, F. Negri, D. Tresoldi, R. Ponzini, D. Massai, M. Deriu, P. Segers, B. Verhegghe, G. Rizzo, et al., On the use of in vivo measured flow rates as boundary conditions for image-based hemodynamic models of the human aorta: implications for indicators of abnormal flow, Ann. Biomed. Eng. 40 (3) (2012) 729–741.
[146] J. Alastruey, N. Xiao, H. Fok, T. Schaeffter, C.A. Figueroa, On the impact of modelling assumptions in multi-scale, subject-specific models of aortic haemodynamics, J. R. Soc. Interface 13 (119) (2016) 20160073.
[147] J. Lantz, P. Dyverfeldt, T. Ebbers, Improving blood flow simulations by incorporating measured subject-specific wall motion, Cardiovasc. Eng. Technol. 5 (3) (2014) 261–269.
[148] M. Galderisi, Diastolic dysfunction and diastolic heart failure: diagnostic, prognostic and therapeutic aspects, Cardiovasc. Ultrasound 3 (1) (2005) 1–14.
[149] S.F. Nagueh, Left ventricular diastolic function: Understanding pathophysiology, diagnosis, and prognosis with echocardiography, JACC Cardiovasc. Imaging 13 (1) (2020) 228–244, http://dx.doi.org/10.1016/j.jcmg.2018.10.038.
[150] G. Keren, J. Sherez, R. Megidish, B. Levitt, S. Laniado, Pulmonary venous flow pattern–its relationship to cardiac dynamics. A pulsed Doppler echocardiographic study, Circulation 71 (6) (1985) 1105–1112.
[151] P.S. Pagel, F. Kehl, M. Gare, D.A. Hettrick, J.R. Kersten, D.C. Warltier, Mechanical function of the left atrium: new insights based on analysis of pressure–volume relations and Doppler echocardiography, J. Am. Soc. Anesthesiol. 98 (4) (2003) 975–994, http://dx.doi.org/10.1097/00000542-200304000-00027.
[152] D. Peluso, L.P. Badano, D. Muraru, L. Dal Bianco, U. Cucchini, G. Kocabay, A. Kovàcs, S. Casablanca, S. Iliceto, Right atrial size and function assessed with three-dimensional and speckle-tracking echocardiography in 200 healthy volunteers, Eur. Heart J. Cardiovasc. Imaging 14 (11) (2013) 1106–1114, http://dx.doi.org/10.1093/ehjci/jet024.
[153] W. Li, K. Wan, Y. Han, H. Liu, W. Cheng, J. Sun, Y. Luo, D. Yang, Y.-C. Chung, Y. Chen, Reference value of left and right atrial size and phasic function by SSFP CMR at 3.0 t in healthy Chinese adults, Sci. Rep. 7 (1) (2017) 3196, http://dx.doi.org/10.1038/s41598-017-03377-6.
[154] L. Thomas, D. Muraru, B.A. Popescu, M. Sitges, M. Rosca, G. Pedrizzetti, M.Y. Henein, E. Donal, L.P. Badano, Evaluation of left atrial size and function: relevance for clinical practice, J. Am. Soc. Echocardiogr. 33 (8) (2020) 934–952, http://dx.doi.org/10.1016/j.echo.2020.03.021.
[155] L.P. Badano, M.H. Miglioranza, S. Mihăilă, D. Peluso, J. Xhaxho, M.P. Marra, U. Cucchini, N. Soriani, S. Iliceto, D. Muraru, Left atrial volumes and function by three-dimensional echocardiography: reference values, accuracy, reproducibility, and comparison with two-dimensional echocardiographic measurements, Circ.: Cardiovasc. Imaging 9 (7) (2016) e004229, http://dx.doi.org/10.1161/CIRCIMAGING.115.004229.
[156] D. Chambers, C. Huang, G. Matthews, Venous pressure waveforms, in: Basic Physiology for Anaesthetists, second ed., Cambridge University Press, 2019, pp. 166–167, http://dx.doi.org/10.1017/9781108565011.041.
[157] D.G. Gibson, D.P. Francis, Clinical assessment of left ventricular diastolic function, Heart 89 (2) (2003) 231–238.
[158] A.R. Vest, Preload, in: Cardiovascular Hemodynamics: An Introductory Guide, Springer International Publishing, Cham, 2019, pp. 3–22, http://dx.doi.org/10.1007/978-3-030-19131-3_1.
[159] M.A. Chizner, Cardiac auscultation: rediscovering the lost art, Curr. Probl. Cardiol. 33 (7) (2008) 326–408, http://dx.doi.org/10.1016/j.cpcardiol.2008.03.003.

[160] M. Carlsson, M. Ugander, H. Mosén, T. Buhre, H. Arheden, Atrioventricular plane displacement is the major contributor to left ventricular pumping in healthy adults, athletes, and patients with dilated cardiomyopathy, Am. J. Physiol.-Heart Circ. Physiol. 292 (3) (2007) H1452–H1459, http://dx.doi.org/10.1152/ajpheart.01148.2006.

[161] M. Salvador, F. Regazzoni, S. Pagani, L. Dede', N. Trayanova, A. Quarteroni, The role of mechano-electric feedbacks and hemodynamic coupling in scar-related ventricular tachycardia, Comput. Biol. Med. 142 (2022) 105203, http://dx.doi.org/10.1016/j.compbiomed.2021.105203.

[162] N. Kawel-Boehm, S.J. Hetzel, B. Ambale-Venkatesh, G. Captur, C.J. Francois, M. Jerosch-Herold, M. Salerno, S.D. Teague, E. Valsangiacomo-Buechel, R.J. Van der Geest, et al., Reference ranges ("normal values") for cardiovascular magnetic resonance (CMR) in adults and children: 2020 update, J. Cardiovasc. Magn. Reson. 22 (1) (2020) 1–63, http://dx.doi.org/10.1186/s12968-020-00683-3.

[163] M. Hadjicharalambous, R. Chabiniok, L. Asner, E. Sammut, J. Wong, G. Carr-White, J. Lee, R. Razavi, N. Smith, D. Nordsletten, Analysis of passive cardiac constitutive laws for parameter estimation using 3D tagged MRI, Biomech. Model. Mechanobiol. 14 (4) (2015) 807–828.